

Using Chemical Substitution to Engineer Photomechanical Cinnamalmalononitrile Crystals

Thomas J. Gately⁽¹⁾, Cody J. Perry⁽¹⁾, Sophie Weiss⁽²⁾, Kevin Lam⁽¹⁾, Imadul Islam⁽³⁾, Mohammed Almtiri⁽³⁾, Veronica Carta⁽¹⁾, Gregory J. O. Beran^{(1)*}, Rabih O. Al-Kaysi^{(3)*}, and Christopher J. Bardeen^{(1,2)*}

⁽¹⁾Department of Chemistry
University of California, Riverside
Riverside, CA 92521 (USA)

⁽²⁾Materials Science and Engineering
University of California, Riverside
Riverside, CA 92521 (USA)

⁽³⁾College of Science and Health Professions-3124,
King Saud bin Abdulaziz University for Health Sciences, and King Abdullah International
Medical Research Center (Nanomedicine), Ministry of National Guard Health Affairs, Riyadh
11426,
(Kingdom of Saudi Arabia)

Abstract

The cinnamalmalononitrile (CM) family of molecules can undergo a [2+2] photodimerization in the solid-state and generate photomechanical response. Derivatives exhibit two different crystal packing motifs: head-to-head (HH) in which the molecules stack with the phenyl rings on the same side of the stack, and head-to-tail (HT) in which the phenyl rings of adjacent molecules are on opposite sides. The [2+2] photodimerization is only observed for HT packing motif. Attempts to identify chemical substitution patterns that favor the reactive HT packing based on simple steric and electrostatic considerations fail to reliably predict crystal packing, and fluorination generated both motifs in more-or-less random fashion. Empirically, substitution at the 3-position favors HT packing while substitution at the 4-position favors HH packing. Computational modeling suggests that the tendency for HH or HT packing arrangements stems from complex many-body interactions with the rest of the lattice. Modeling with periodic density functional theory shows that interactions with the rest of the lattice also explain why the HT motif is photochemically active while the HH motif is inert. Chemical substitution can also affect the photomechanical work output, with a significant variation in work between HT polymorphs composed of different molecules. In order to obtain a reactive HT polymorph, the best strategy appears to entail placing a strong electron-withdrawing group at the 3-position of the phenyl, and we confirm that an HT polymorph of 3-trifluoromethyl-cinnamalmalononitrile is a highly photosalient crystal, with a predicted ideal work density of 40 MJ/m³.

1. Introduction

The field of crystal engineering takes a rigorous approach to designing molecules so their crystal packing can generate new physical properties, like solubility, elasticity, thermal conductivity, and waveguiding [10.1002/anie.202302929].^{1, 2} The ability of the crystal lattice to organize molecules also provides a way to control their reactivity. There are now many examples of how crystal packing can influence reaction outcomes, starting with the seminal work of Schmidt and coworkers that gave rise to the concept of topochemistry.³⁻⁵ Much of that foundational work concerned [2+2] photocycloaddition reactions between cinnamate derivatives, and this reaction has continued to be a workhorse of the field.⁶ Its synthetic utility has been demonstrated by the work of MacGillivray and others and has been used to create highly crystalline polymer solids as well.^{7, 8} This solid-state reaction has also been harnessed to generate photomechanical motion.⁹⁻¹⁷ Vittal and coworkers pioneered a supramolecular approach that resulted in crystals that exhibit dramatic photosalient effects¹⁸⁻²³, a general phenomenon in which the photochemical creation of the product raises the potential energy inside the crystal until it is suddenly released as kinetic energy by a combination of fracture and/or phase change.^{24, 25} Although the [2+2] photodimerization is not easily reversed, it provides a useful way to investigate how molecular-level reactions can combine to generate a macroscopic mechanical effect.

We became interested in the potential of the [2+2] photocycloaddition reaction for force generation after observing that the bimolecular reaction of crystalline (*E*)-4-Fluorocinnamaldehyde malononitrile (*E*-4FCM) could produce ~10× more work in a bending ceramic template than the diarylethene derivatives used previously.²⁶ This class of molecules utilizes a divinyl sidegroup to increase conjugation and shift the absorption to longer wavelengths and had

previously been shown to be photochemically active in crystal form.²⁷ We sought to improve the performance of this molecule by adding fluorine atoms to the phenyl ring and found that the derivatives all crystallized into one of two characteristic packing motifs.²⁸ In the head-to-head (HH) motif, the molecules stack with the phenyl rings on the same side of the stack, while in the head-to-tail (HT) motif the phenyl rings of adjacent molecules are on opposite sides. As long as the reactive double bonds are within 4.2 Å of each other, the HT packing motif supports rapid [2+2] photodimerization, while the HH motif is unreactive regardless of the double bond separation. Because of the different HH versus HT reactivities, the crystal packing controls the ability of CM derivatives to function as photomechanical materials. Computational work indicated that the HH and HT polymorph energies were often within 1-3 kJ/mol of each other. In some cases, the same molecule could be crystallized in either polymorph by changing the growth solvent.²⁸

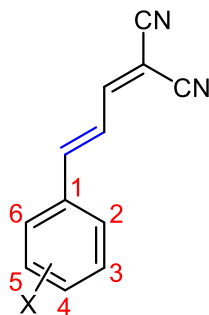


Figure x

The complex crystallization behavior of the **CM** derivatives, combined with their potential utility as photomechanical materials, motivated us to study them in greater detail. In particular, we wanted to understand what factors control HH versus HT crystal packing, since this determines whether the crystal can be photomechanically active. Our goal was to test two simple hypotheses. First, we reasoned that substituents at the 4-position will increase steric repulsion for molecules stacked in the HH geometry, raising its energy. On the other hand,

substituents at the 3-position can align on opposite sides of the stack in the HH motif and avoid this steric interference (Figure-x). These effects are illustrated in Scheme 1a. The steric interference hypothesis predicts that substitution at the 4-position will favor HT packing, while substitution at the 3-position will produce more HH crystals. The second hypothesis centers on electrostatic interactions between neighboring molecules. The addition or removal of electron density from the phenyl ring should affect its interaction with the electronegative CN groups of neighboring molecules. If the molecule is thought of as a large dipole, then a larger dipole moment should favor HT packing to maximize the Coulomb stabilization. On the other hand, substituents that decrease the net dipole should reduce the Coulomb interaction and make the HH geometry more likely to be observed. This effect is illustrated in Scheme 1b. If validated, these two hypotheses could provide a framework for the design of new materials based on the CM framework.

In this paper, we show that the reasoning described above, based on simple steric and electrostatic considerations of the monomer pair, fails to reliably predict the trends observed for the 23 molecules reported here and in our previous paper.²⁸ Experimentally, we find that most derivatives behave opposite to the expected trends, with substitution at the 3-position being the most likely to yield the reactive HT form. Computational modeling suggests that the tendency for HH or HT packing stems from a competition between the interactions within the monomer pair, which favor HT packing, and those between the pair and the rest of the lattice that favor the HH motif. By modeling the solid-state transformations with periodic density functional theory (DFT), we find that this competition between the interactions within the monomer pair and those of the pair with the rest of the lattice is also fundamentally related to the experimentally observed differences in the HH and HT solid-state reactivities. Finally, chemical substitution not only

controls crystal packing and reactivity but can also affect the photomechanical work output, with a significant variation in work between HT polymorphs composed of different molecules. The results in this paper significantly expand the available library of photoreactive phenyl-divinyl molecules and their crystal structures, providing a new testbed for theoretical crystal structure prediction models. Eventually, these models will guide the development of new design principles for improved photoresponsive molecular crystals.

2. Experimental and Computational Methods

Sample Preparation: The detailed synthesis of previously unreported CM derivatives can be found in the Supporting Information. Most crystals were grown by solvent evaporation. Typically, 4 mg of the compound was dissolved in 2 mL of solvent. For all compounds, crystallization was attempted in both a protic solvent (methanol or ethanol) and an aprotic solvent (CHCl₃ or toluene). Testing different solvents was necessary because we previously found that different solvents could generate different polymorphs.²⁸ The solutions were placed, in a loosely capped vial and stored in a dark cabinet while the solvent was allowed to evaporate over several days. Some growth solutions were placed in the refrigerator to slow the evaporation rate and enhance crystal quality. **3CNCM** and the **4CICM** crystals were grown using the solvent diffusion method. The compound was dissolved in chloroform in a 5 mL vial that was then placed open in a 20 mL jar containing isopropyl alcohol. As the alcohol diffused into the CHCl₃, the crystals grew over the course of a several days. All samples were protected from light exposure during growth.

Sample Characterization: Crystal structures were obtained using a Bruker D8 Venture Duo diffractometer. Details of the X-ray diffraction analysis for each molecule can be found in the Supporting Information. For microscopic observation of the crystals, an Olympus IX70-inverted microscope with an IX-FLA fluorescence observation attachment with 365 nm, 405 nm, 465 nm and 532 nm filter cubes was used. Images and videos were obtained using an Amscope MU1000 camera. For solution-state spectroscopic measurements, samples were prepared by dissolving approximately 1 mg of compound in 10 mL of chloroform. The solution was then placed into a quartz cuvette with a 1 cm pathlength and analyzed in a Cary 60 spectrometer from 200 to 800 nm using a scan speed of 600 nm/min.

Computational Methods

Gas-Phase Monomer Studies: For isolated molecules, dipole moments were calculated using Gaussian 16 software. The structures were optimized using the B3LYP functional and cc-pvdz basis set.

Gas-Phase Monomer Pair Studies: Initial gas-phase studies of HH and HT monomer pairs were carried out using zeroth-order symmetry adapted perturbation theory (SAPT0)^{29, 30}, which naturally decomposes intermolecular interaction energies into contributions arising from short-range exchange-repulsion, electrostatics, induction, and dispersion. The calculations employed PSI4 v1.7³¹ and the jun-cc-pVDZ basis, which performed well in an earlier benchmark study.³² After optimizing the monomer molecular structures with r²SCAN-3c³³, π -stacked monomer pairs were created with a 3.5 Å intermolecular separation. Two-dimensional interaction surfaces were

then computed by displacing one rigid monomer relative to the other along the long and short axes of the molecule (holding the 3.5 Å separation constant).

Solid-State DFT: To model the solid-state systems, the experimental crystal structures were optimized in Quantum Espresso 6.5³⁴ under periodic boundary conditions using the B86bPBE density functional^{35, 36} with the exchange hole dipole moment (XDM) dispersion correction.³⁷ A 50 Ry plane-wave cutoff was combined with the projector augmented wave (PAW) treatment of core electrons. A Monkhorst-Pack reciprocal space k-point grid spacing of at least 0.05 Å⁻¹ was used.

Generalized gradient approximate (GGA) density functionals such as B86bPBE are convenient for solid-state electronic structure calculations due to their relatively low computational cost, but they suffer from density-driven delocalization error³⁸, which can lead to artificial stabilization of species exhibiting greater electron delocalization relative to those that do not.³⁹ The [2+2]-photodimerization disrupts the π -conjugation in the CM species, resulting in a more localized electron density in the product molecule than in the reactants. As a result, delocalization error in a GGA functional will spuriously destabilize the photodimer product species relative to the reactants.⁴⁰ To address delocalization error in the GGA functional used in this work and obtain more realistic energetics, a single-point intramolecular energy correction is applied to the final optimized crystal energies using a higher level of theory⁴¹ —in this case, the double-hybrid revDSD-PBEP86 functional and D4 dispersion correction.⁴² In this approach, one computes the periodic B86bPBE-XDM energy of the crystal, subtracts out the gas-phase B86bPBE-XDM energy of each isolated molecule in the unit cell (retaining crystalline

geometry), and adds the gas-phase revDSD-PBEP86-D4 (“Higher”) energy of each isolated molecule,

$$E_{crystal}^{corrected} = E_{crystal}^{GGA} + \sum_i (E_{molec,i}^{Higher} - E_{molec,i}^{GGA}) \quad (1)$$

This approximation amounts to computing the intramolecular interactions with revDSD-PBEP86-D4, and the intermolecular interactions with the lattice with B86bPBE-XDM. The gas-phase B86bPBE-XDM energies are calculated in Quantum Espresso using the same settings, except the molecules are placed in a large periodic box with at least 20 Å spacing in all directions to minimize the interactions between the molecule in its periodic images. See reference ⁴¹ for details. The revDSD-PBEP86-D4 energies were calculated in Orca 5.0⁴³ in the def2-QZVP basis set. In practice, the intramolecular corrections only needs to be computed for each symmetrically-unique molecule in the unit cell, and the results can be multiplied by the number of equivalent molecules in the unit cell.

Modeling the Solid-State Photomechanical Responses: Techniques developed in reference ⁴⁴ were employed to study the [2+2] photochemical reactivity and resulting photomechanical responses of the crystals. In brief, this idealized model assumes the photochemical reaction occurs instantly and completely, resulting in a “proto-SSRD” crystal structure which contains the photodimer product molecules within the unit cell of the reactant crystal. Starting from the DFT-optimized monomer crystal structure, the proto-SSRD is generated by replacing pairs of topochemically reacting monomers in the crystal with the photodimer product and minimizing the orientational and translational displacement. A fixed-lattice parameter DFT optimization of this structure that produces the final proto-SSRD. Next, a variable unit cell DFT optimization is

performed to relax the proto-SSRD to the equilibrium SSRD crystal structure. This process deforms the crystal, and the associated anisotropic work density can be computed from the stress and strain associated with the proto-SSRD relative to the equilibrium SSRD. The idealized photomechanical approach provides an upper-bound estimate for the amount of work that could be performed, since experimental photomechanical crystals may not react to 100% completion, and they will likely react more slowly and generate less stress by allowing the lattice to relax as the molecules react. This topochemical modeling approach has correctly predicted the product crystal structures that result from the solid-state photochemical reactions of anthracenes and diarylethenes.^{44, 45}

3. Experimental Results

Our synthetic strategy for making the various **CM** derivatives is modular and provides a way to rapidly generate a library of different compounds. Details of the synthesis and characterization of the 12 new **CM** derivatives (structures shown in Table 1) are given in the Supporting Information. This set of molecules significantly expands the library of **CM** molecules beyond the 11 derivatives described in our first paper.²⁸ This new set of molecules has two purposes. First, we wanted to expand the library of fluorinated derivatives to fill in some gaps in our previous paper. The molecules **2,5FCM**, **3,4FCM**, and **2,3,6FCM** provide new molecules to test whether increasing the electron withdrawing power attached to the phenyl can favor the HT motif. The other 9 molecules were prepared in order to examine whether substituents (**X**) at the 3-position (denoted **3XCM**) and the 4-position (denoted **4XCM**) can favor HT versus HH packing. Including results from our previous paper, the 3 and 4-position substituents are (from smallest to largest): H, F, Cl, Br, CN, CF₃, and OCH₃. This series of

substituents was chosen because *a)* they provided a large range of sizes and electron withdrawing/donating character; and *b)* they provided crystals suitable for x-ray structure determination. We synthesized **CM** derivatives with other substituent groups, but if crystals suitable for x-ray structure determination could not be grown, they were not included in this study. For example, several CH₃ derivatives were synthesized, but they had surprisingly low solubility and we could not obtain crystals suitable for XRD structure determination.

The ability of different substituents to modify the electronic structure of the conjugated **CM** core could be inferred from changes in the electronic absorption spectra. The strong electron-withdrawing CN groups, combined with the extended conjugation of the allylidenemalononitrile tail, impart some charge-transfer (CT) character to the absorption spectrum, which helps shift the absorption peak of **CM** to ~350 nm as compared to a cinnamate whose absorption spectrum typically peaks around 300 nm. But this CT character can be partially cancelled out by placing fluorine atoms on the phenyl ring. Figure 1a shows how the addition of F atoms systematically shifts the absorption peak relative to **CM**, without any appreciable change in the absorption lineshape. When all the fluorinated compounds were analyzed together, we found that increasing the number of F atoms systematically shifted the absorption peak to higher energies, as seen from the plot in Figure 1b.

Substitution of other chemical groups at the 3- and 4-positions can also lead to substantial changes in the absorption spectrum. We find that substitution at the 4-position has a much larger effect on the absorption than at the 3-position. Since a group at the 4-position is *para* to the allylidenemalononitrile tail, it will be conjugated with this group and is expected to have a larger effect than a substituent at the *meta* position. This is consistent with the smaller absorption peak shifts seen for the **3XCMs** when compared to the **4XCMs**, as illustrated for X=Br (Figure 2a)

and X= OCH₃ (Figure 2b). In order to quantify the character of different phenyl ring substituents, we elected to use the Hammett sigma parameter, which has shown to correlate with both electronic absorption peak shifts⁴⁶⁻⁴⁸ and molecular dipole moments^{49, 50} of aromatic systems. In both the **3XCMs** and **4XCMs**, we found a good correlation between the peak absorption energy and the Hammett sigma parameter, as shown in Figures 3a and 3b. The calculated molecular dipole moment was also correlated with this parameter, as shown in Figures 3c and 3d. Together, these plots confirm that the various substituents have a systematic effect on the electron density distribution in the molecule. The next question is whether these changes influence the crystal packing in a systematic way.

When crystallized, we were surprised to find that all the new fluorinated **CMs** packed in the nonreactive HH motif. This observation showed that F substitution does not systematically favor one packing motif over the other. Symmetric fluorine substitution in the molecules **4FCM** (HH/HT), **2,5FCM** (HH), **3,4,5FCM** (HH), **2,3,5,6FCM** (HH) and **2,3,4,5,6FCM** (HH/HT) yielded the HH and HT forms with roughly equal probability. Asymmetric substitution in the molecules **2FCM** (HT), **3FCM** (HH), **2,4FCM** (HT), **3,4FCM** (HH) and **2,3,6FCM** (HH) also yielded a similar number of HH and HT forms. No obvious pattern could be extracted from the results. Previous theory suggested that the HH and HT forms were very close in energy²⁸, and indeed both polymorphs could be grown from **4FCM** and **2,3,4,5,6FCM**. It is possible that all the fluorinated derivatives possess HH and HT polymorphs that could be uncovered by an exhaustive search of the crystal growth conditions. However, from our results it is clear that although F atoms are known to be effective crystal growth directors, in the **CMs** they cannot steer the packing toward either HH or HT motifs in a systematic way.

When the phenyl ring substitution position was fixed and the chemical nature of the substituent was varied, we began to see patterns emerge. Substitution at the 3-position produced crystals that were mostly of the HT form, while substitution at the 4-position favored the HH form. Examples of this effect are shown in Figures 4a and 4b for **3CICM** versus **4CICM**, and for **3BrCM** versus **4BrCM** in Figure 4c and 4d. The complete trend for the **3XCMs** is shown in Figure 5a, where the presence of both HH and HT polymorphs is represented as an intermediate point between the HH and HT extremes. Except for **3CNFCM** and **3FCM**, all molecules with a substituent at the 3-position support an HT crystal form. Figure 5b shows the HH/HT trend for the **4XCMs**, where the majority exhibit HH packing.

The different crystal packings gave rise to the expected differences in photomechanical behavior. All the HT crystals exhibited rapid photoreaction and a photosalient response except for **4CF₃CM**, which packs in an offset HT geometry with the double bonds separated by 4.3 Å, just outside Schmidt's distance that allows photodimerization.⁵¹ In contrast, all HH crystals were highly fluorescent. After extended exposure to ultraviolet light (10 minutes or more), they sometimes exhibited fading and slight bending, but we attributed this to heating and/or reaction at induced defect sites, rather than to intrinsic reactivity. It is noteworthy that crystallization of **3CF₃CM** from a nonpolar solvent like xylene causes it to grow in a modified HH motif with the molecules twisted at ~45° with respect to each other, as shown in Figure 6a. This twisted form may be an indication that the bulky CF₃ groups interfere with the π-π interactions that would be expected to drive HH stacking. This polymorph appears to be photochemically inactive due to a misalignment of the double bonds, despite the fact that they are relatively close (3.64 Å) and fall within the Schmidt's distance. The HT form was obtained by crystallization from a polar solvent like CHCl₃, and it reacted rapidly and violently when exposed to ultraviolet light. In our

experience, the photosalient effect can be strongly attenuated when the crystals are submerged in a viscous medium, but **3CF₃CM** showed strong photosalient behavior even when submerged in highly viscous glycerol. Examples of this response are shown in videos in the Supporting Information. It had a much larger photosalient response than the other crystals studied in this work.

4. Discussion and Computational Analysis

4.1 Origins of HH versus HT packing

The results in Figure 5 provide strong evidence that our original steric hypothesis was not correct. We hypothesized that substituents at the 4-position of the phenyl ring would interfere with each other, and this should favor the HT form so the two neighboring groups could avoid interacting with each other. Meanwhile, the ability of the **3XCMs** to stack in the HH form with the substituents on alternating sides would lower the energy of this motif and make it more commonly observed. Instead, we found the opposite trend: **3XCMs** favor HT packing, while **4XCMs** favor HH packing. For the **3XCMs** that did exhibit HH packing (X=CN, F), the X groups line up on the same side in the crystal stacks, with no evidence for the alternating sidegroup stacking that we hypothesized at the beginning of this work. The data in Figure 5b show that putting bulky groups at the 4-position is not a viable strategy to enforce HT packing.

If we consider simple electrostatic effects, it is again difficult to rationalize the trends shown in Figure 5. For the **3XCMs**, the two molecules that support the HH form, **3CN₂CM** and **3FCM**, have very different dipole moments, while the molecules with intermediate dipole moments support HT packing. Only **3CN₂CM** has an anomalously low dipole moment (1.8 Debye) that would be expected to favor HH packing. Substituents at the 4-position are expected

to have a much larger effect on the molecular electron density because they are para to the divinyl tail. But here again there is no clear pattern, with HT packing observed for both large dipoles (**CM**) and much smaller dipoles (**3CF₃CM**), while intermediate dipoles exhibit HH packing. It appears that coarse measures of electron density, like the molecular dipole moment, are not sufficient to predict crystal structure trends in the **CM** class of molecules.

The failure of our crystal packing predictions based on simplistic two-body molecular interactions points to the need for a more sophisticated theoretical approach that can handle many-body interactions. In fact, when molecular pairs are considered by themselves, the HT packing is always favored. Gas-phase symmetry-adapted perturbation theory (SAPT0) calculations on π -stacked HH and HT monomer pairs of **3XCM**, and **4XCM** (X = F, Cl, or Br) and a 3.5 Å separation between the molecules indicate that the HT pair stacks arrangements bind ~10-20 kJ/mol more strongly than the HH ones (Figures 7 and 8). For hydrogen and smaller halogens, the optimal HT stacking arrangement involves one molecule being slightly displaced (typically by ~1 Å) along the long (x) axis relative to the other, though the energetic penalty for small (<1 Å) lateral displacements along the short (y) axis is modest. As the halogen grows in size, however, larger displacements along both axes become increasingly favorable. The preferred HH stacking geometry involves either a large, ~3-3.5 Å displacement along the long axis or simultaneous ~1-1.5 Å displacements along both the long (x) and short (y) axes of the molecule. The local minima observed in these monomer pair scans, particularly those with more modest displacements, are generally consistent with the arrangements observed in the experimental crystal structures. Comparing Figures 7 and 8, one also sees that the **3XCM** monomer pairs frequently bind more strongly than the **4XCM** pairs, though the differences are fairly similar across both HH and HT arrangements. The SAPT0 energy decomposition

(Supporting Information) reveals that HT stacked monomer pairs benefit from stronger electrostatic attractions and reduced short-range exchange-repulsion interactions (i.e. less steric interference) while the HH interactions exhibit moderately stronger attractive van der Waals dispersion interactions. The attractive induction (polarization) contributions are similar across both HH and HT monomer pairs.

Unfortunately, isolated pair interaction energies do not provide a clear rationale for why certain derivatives adopt HT or HH packing motifs in the solid state. Given that the HH stacks consistently exhibit weaker pair-wise interactions than HT ones, the HH crystals must compensate by forming stronger many-body interactions with the rest of the lattice such that they achieve similar total lattice energies. For example, **4FCM**, **3CICM**, and **CF₃CM** exhibit two polymorphs each with different dimer arrangements that differ by only ~1 kJ/mol in lattice energy according to periodic B86bPBE-XDM DFT calculations. The calculations suggest that the non-reactive HH polymorph of **4FCM**, the reactive colorless polymorph of **3CICM**, and the reactive HT polymorph of **3CF₃CM** are the more stable polymorphs by 1.3, 1.0, and 1.3 kJ/mol, respectively (though such small lattice energy differences could easily be reversed by errors in the DFT models and/or finite-temperature free energy contributions). Additional evidence for the energy compensation between HH and HT motifs in the solid-state comes from our earlier crystal structure prediction study which found many energetically-competitive HH and HT structures for both for **CM** and **4FCM**.²⁸

Finally, we partition the lattice energies for 10 experimental crystals into the contributions stemming from the interaction of the HH or HT monomer pair and from the interactions of that pair with the rest of the lattice. This set includes five HT crystals (**HCM**, **4FCM**, **3CICM**, **3CF₃CM**, and **2,4FCM**) and five HH ones (**3FCM**, **4FCM**, **2,5FCM**,

2,6FCM, and **4CNCM**). In the absence of the surrounding lattice, the 21 kJ/mol average HT monomer pair interaction energy component of the lattice energy is 9 kJ/mol stronger than the 12 kJ/mol average HH interaction. On the other hand, the HH crystals compensate for these weaker interactions within the non-covalent monomer pair through interactions with the rest of the lattice that are 12 kJ/mol stronger than for the HT ones on average.

In summary, it is difficult to assess whether a HH or HT crystal will form based on the monomer pair alone; rather, it is driven by a competition between the interactions within the monomer pair and the interactions of that pair with the rest of the lattice. Identifying specific, universal lattice interactions that stabilize the HH crystals is difficult, due to the wide variety of the crystal packing motifs. From the dense crystal energy landscapes found for **HCM** and **4FCM** in the earlier crystal structure prediction study²⁸ and the two additional examples of experimental polymorphs discussed here, it seems likely that polymorphism is probably thermodynamically feasible for many of these systems. Whether those polymorphs are observed experimentally may simply be a matter of the crystallization kinetics and conditions.

4.2 Reactivity differences between HH and HT crystals

To understand why the HT crystals react while the HH ones do not, we modeled the solid-state photochemical reactions for ten **CM** derivative crystals using the crystalline topochemical approach described in the Computational Methods section. Consider first **4FCM**. While the HT and HH polymorph lattice energies differ by only 1.3 kJ/mol, the predicted solid-state photodimerization energies differ considerably. The reaction energy is endothermic by 55 kJ/mol in the HT crystal, but it increases to 80 kJ/mol in the HH crystal (Figure 9). Similar trends span the other eight solid-state photodimerization reactions examined. The average solid-

state photodimerization energy for the HT crystals of **HCM**, **4FCM**, **3CICM**, **3CF₃CM**, and **2,4FCM** is 44 kJ/mol (range 40-55 kJ/mol). In contrast, the average computed solid-state reaction energy for the HH crystals of **3FCM**, **4FCM**, **2,5FCM**, **2,6FCM**, and **4CNCM** is 80% larger at 80 kJ/mol (range 69-100 kJ/mol). Similar endothermicity arguments were invoked previously to rationalize reactive and non-reactive anthracene crystals.⁵²

To understand the origin of these reaction energy differences, we decompose the solid-state energy contributions for these 10 cases. Figure 9 separates the total solid-state reaction energy into the “gas-phase” contribution (obtained from gas-phase calculations on the reactant monomer pair and the product photodimer using geometries extracted directly from the DFT-optimized crystal structures) and the “lattice contribution” which indicates how the photodimerization energy changes in the presence of the surrounding lattice. For these ten systems, the average gas-phase reaction energies for HT (40 kJ/mol) and HH (43 kJ/mol) systems are very similar. Accounting for the rest of the crystal lattice contribution increases the HT reaction energies by only 4 kJ/mol on average but substantially increases the HH reaction energies by 37 kJ/mol on average.

Overall, the calculations thus far have revealed that HH crystal packing motifs are competitive with HT ones only when the HH monomer pairs can compensate by forming stronger interactions with the rest of the lattice. Because [2+2] photodimerization significantly deforms the molecular pair, the stronger interactions with HH lattices effectively inhibit the photodimerization of the monomer pairs.

4.3 Photomechanical transformations in 3CICM and 3CF₃CM

Finally, we investigate the experimental observation that the reactive HT polymorph of **3CF₃CM** exhibits stronger photosaliency than the reactive polymorph of **3ClCM**, again using the topochemical approach to predict the photomechanical response properties. The modeling (Figure 10) indicates that both crystals exhibit small net volume changes upon photodimerization: **3ClCM** expands 1% and **3CF₃CM** contracts 0.3%. The buckling of the **3ClCM** molecules upon photodimerization elongates the *a* axis by 0.4 Å (5.7%) and increases the β angle by 2.9% (Figure 8). Photodimerization also effectively shortens the length of the molecule along its long axis, leading to a large 1.2 Å (5.9%) contraction along the *b* axis. Finally, a small 0.2 Å (2.4%) increase in the intermolecular spacing along the short **3ClCM** molecular axis occurs as well to reduce clashes between the adjacent photodimers. The photodimerization of **3CF₃CM** has a qualitatively similar behavior, though the molecular orientations relative to the unit cell axes differ. The molecular buckling from photodimerization expands the lattice 1.0 Å (10.7%) along the *b* axis. The lattice contracts 1.2 Å (6.8%) along the long molecular axis (*c* axis), and slightly expands 0.1 Å (1.5%) along the short molecular axis (*a* axis). Due to the herringbone nature of the packing, however, the lateral clashes created by CF₃ and other groups upon the photodimer buckling force the β angle to increase by a much larger 8.8%.

Given the significant anisotropy in the photomechanical structural response, it is unsurprising that the work density plots in Figure 10 are also highly anisotropic. While one might expect the expansion due to photodimer buckling to produce the most work density along the *b*-axis, the largest work density actually stems from the large *c* axis contraction in both crystals. That contraction occurs both because the photodimerized molecules become shorter along *c* due to the buckling and because the buckled photodimers exhibit more favorable C-H···Halogen interactions with nearby photodimers, especially for the larger CF₃ group. In

3CF₃CM, the work density is further enhanced relative to **3CICM** by the lateral steric clashes that induce the large β angle increase. Overall, the computed ~ 40 MJ/m³ work density of **3CF₃CM** is approximately double the ~ 20 MJ/m³ obtained for **3CICM**, which could help explain the more violent photosalient response observed for **3CF₃CM**.

5. Conclusion

In this paper, we have extended our previous results on the use of crystal engineering to create photomechanical crystals based on the **CM** motif. First, we have confirmed that the HT packing motif is required to observe the [2+2] photodimerization. The reactivity differences between HH and HT crystals can be rationalized based on the generally stronger interactions HH monomer pairs form with their surrounding lattice, which in turn inhibits the molecular deformation associated with the [2+2] photodimerization. Because the formation of stronger interactions with the lattice appears to be a prerequisite for adopting HH packing, at least among these minimally-modified **CM** species, we suspect that the reduced reactivity of HH-packed **CM** crystals is probably quite general. Second, we attempted to identify chemical substitution patterns that favor the reactive HT packing. Ideas based on simple steric and electrostatic considerations about how chemical substitution would affect HH versus HT packing were shown to be too naïve to have predictive value. Fluorination appears to generate both motifs in more-or-less random fashion. Computational results revealed that the competition between HH and HT is a complex, many-body interaction within the crystal lattice that cannot readily be explained by consideration of isolated monomer pairs. Nevertheless, we were able to identify an empirical trend in which substitution at the 3-position favors HT packing while substitution at the 4-position favors HH packing. Third, we wanted to get an idea of whether chemical

substitution could affect the photomechanical work generation by an HT crystal. Preliminary results suggest that the answer is yes, with the molecule **3CF₃CM** generating a strong photosalient response experimentally, consistent with the 2× larger computed work density. Overall, our results suggest that the recipe for more powerful photomechanical crystals involves asymmetric substitution at the *meta* (3) position in order to increase molecular size while maintaining HT packing and photoreactivity. The **CM** system provides a useful case study to illustrate how molecular structure, crystal packing, and polymorphism must all be considered when designing a functional molecular crystal.

Acknowledgements

This work was supported by the National Science Foundation, grant DMR-1810514 to C.J.B, and CHE-1955554 to G.J.O.B. Computer time to G.J.O.B from ACCESS (CHE110064) and the UC Riverside High-Performance Computing Center, which was funded by the NSF (MRI-2215705, MRI-1429826) and NIH (1S10OD016290-01A1), is also gratefully acknowledged. R.O.K acknowledges King Abdullah International Medical Research Center (KSAU-HS/KAIMRC) through Grant NRC21R25003.

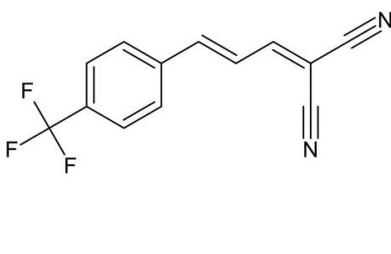
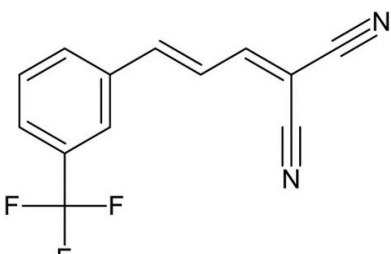
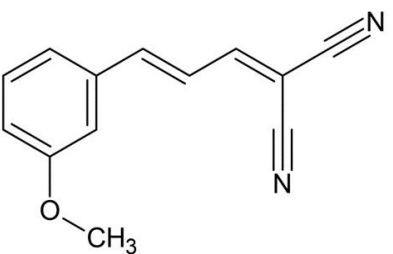
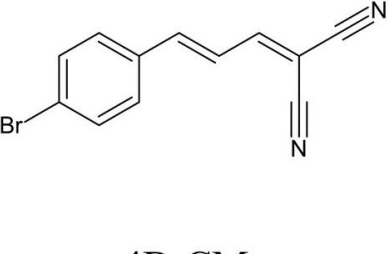
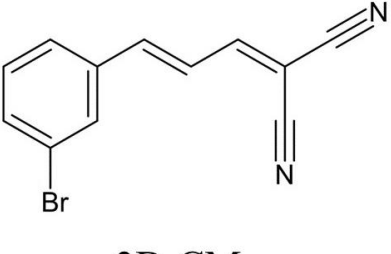
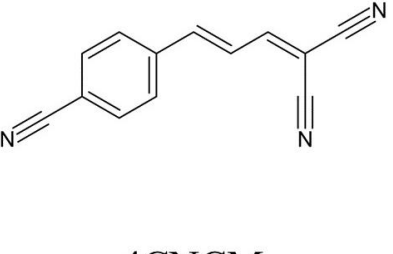
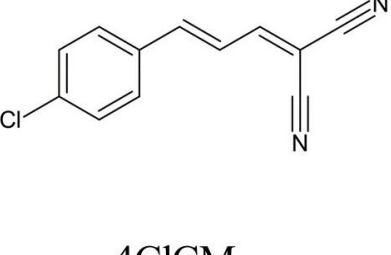
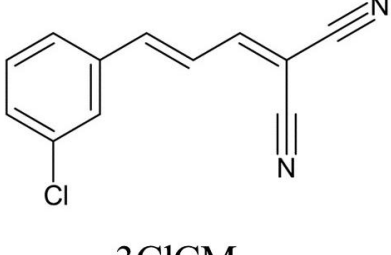
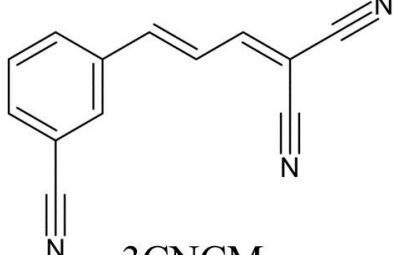
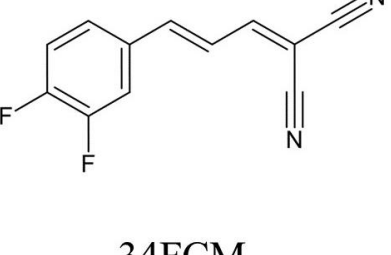
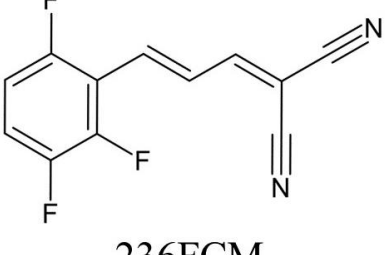
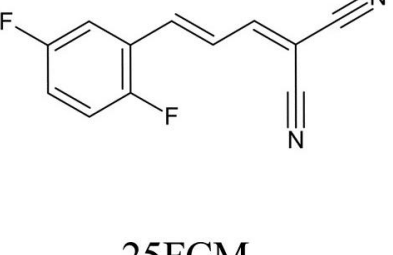
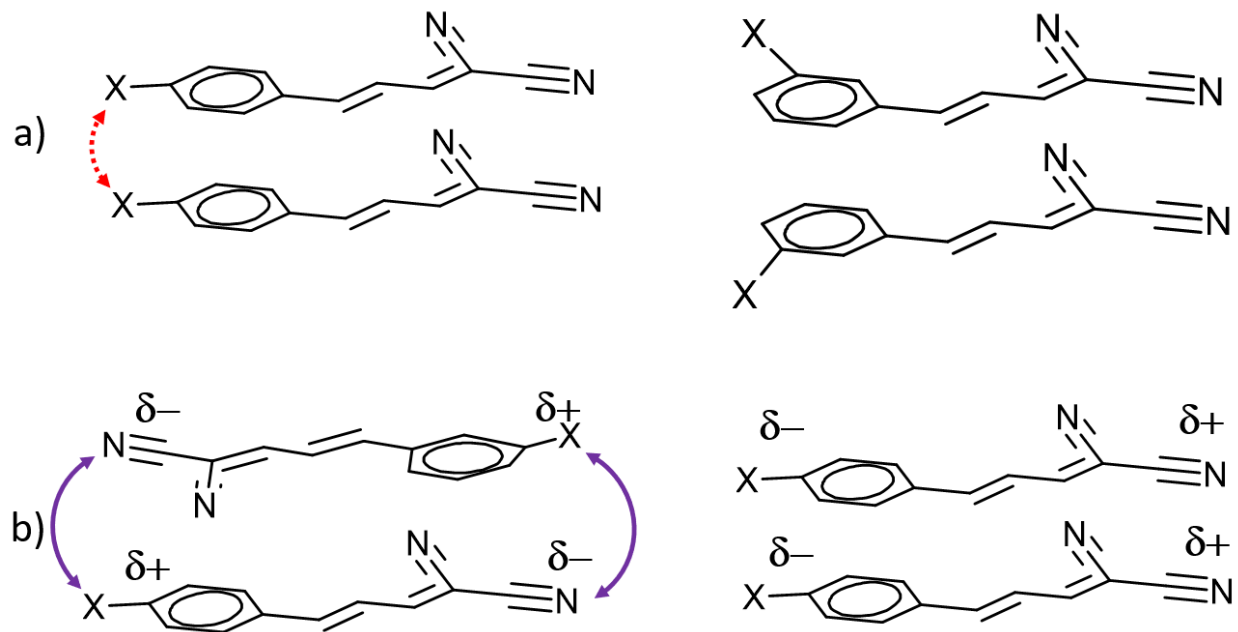
 <p>4CF3CM</p>	 <p>3CF3CM</p>	 <p>3MeCM</p>
 <p>4BrCM</p>	 <p>3BrCM</p>	 <p>4CNCM</p>
 <p>4ClCM</p>	 <p>3ClCM</p>	 <p>3CNCM</p>
 <p>34FCM</p>	 <p>236FCM</p>	 <p>25FCM</p>

Table 1: The new **CM** derivatives examined in this paper and the abbreviations used.

[Please change the label of 3-methoxyCM from 3MeCM to **3MeOCM**]



Scheme 1: a) Adding substituents at the 4-position can lead to steric interference when adopting HH packing (left) while the 3-position can largely avoid the steric interference in HH stacking (right). b) For molecules with a large dipole difference between ends of the molecule HT packing maximizes the Coulomb interaction (left) while a molecule with a small dipole has less of a difference between HH and HT packing.

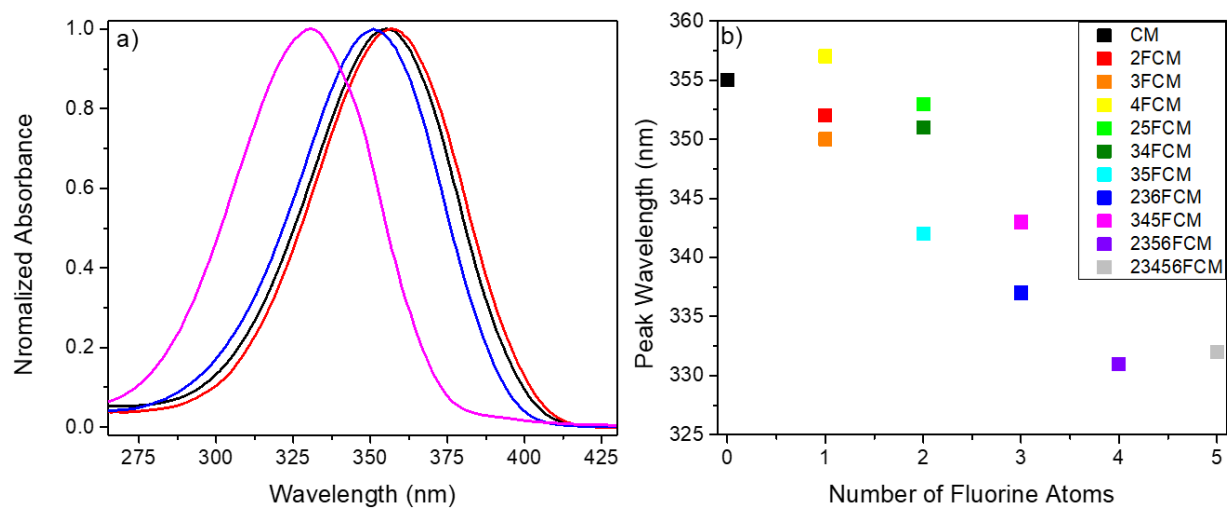


Figure 1: a) The absorption changes of a single fluorine substitution at various positions on **CM**. Black shows the spectra of unsubstituted **HCM**, red shows **4FCM**, blue shows **3,4FCM**, and purple represents **2,3,5,6FCM**. b) The shift in absorption from adding additional fluorine atoms to the **CM** structure.

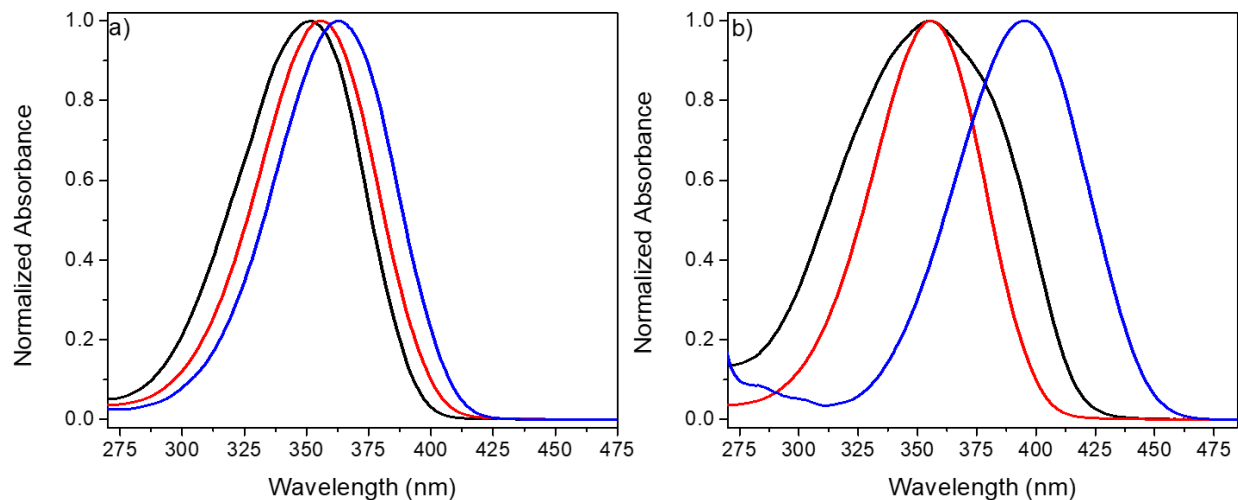


Figure 2: The shift in absorbance of the **3XCMs** and **4XCMs** with different substituents. a) shows **HCM** (red) with a λ_{\max} of 356 nm, **3BrCM** (black) with a λ_{\max} of 352 nm and **4BrCM** (blue) with a λ_{\max} of 363 nm. b) shows unsubstituted **HCM** (red) **3MeOCM** (black) with a λ_{\max} of 355 nm and **4MeOCM** (blue) with a λ_{\max} of 395 nm.

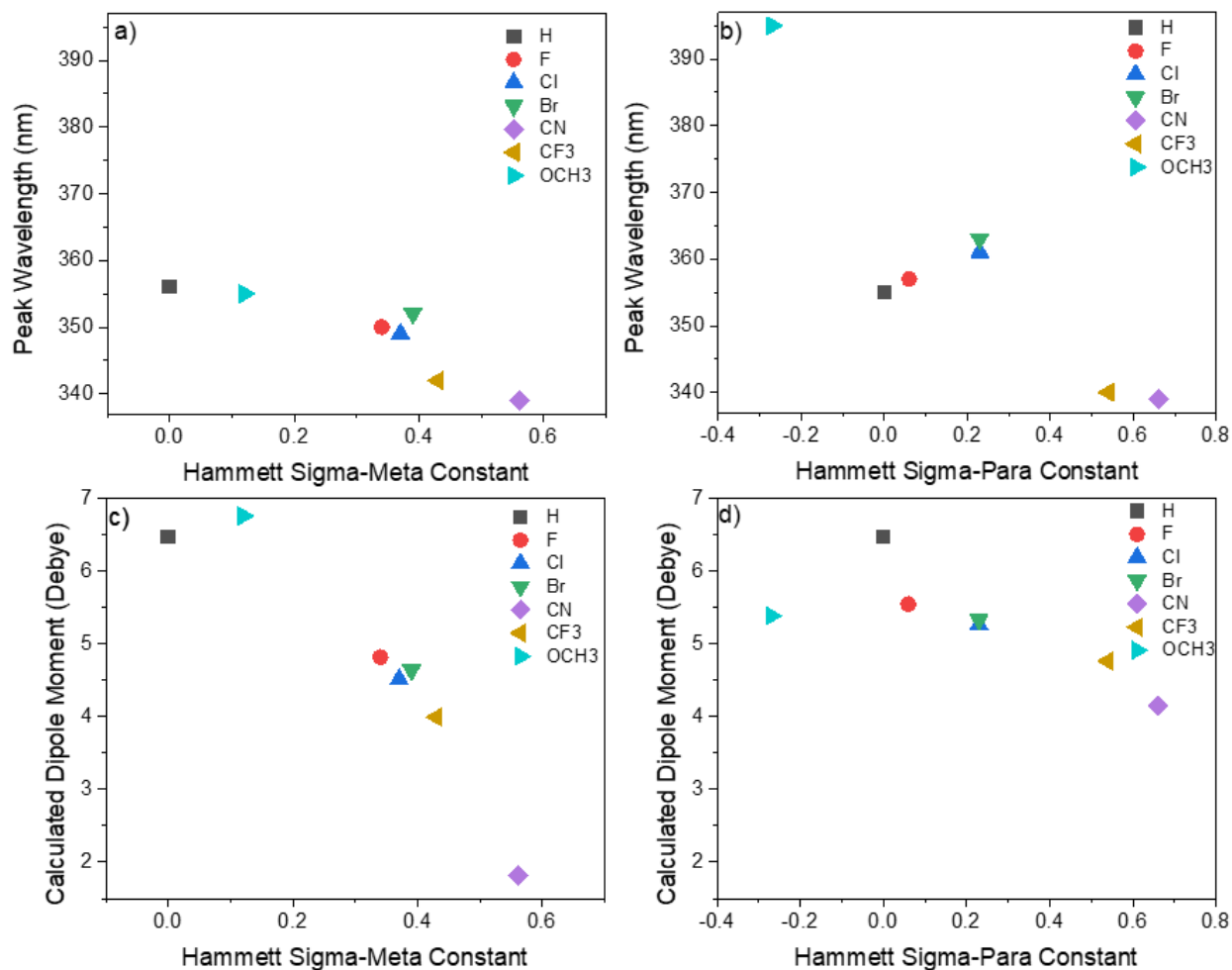


Figure 3: The peak wavelength absorption plotted against the Hammett sigma parameter for a) the meta substituted **3XCMs** and b) the para substituted **4XCMs**. The calculated molecular dipole moment plotted against the Hammett sigma parameter for c) the meta substituted **3XCMs** and b) the para substituted **4XCMs**.

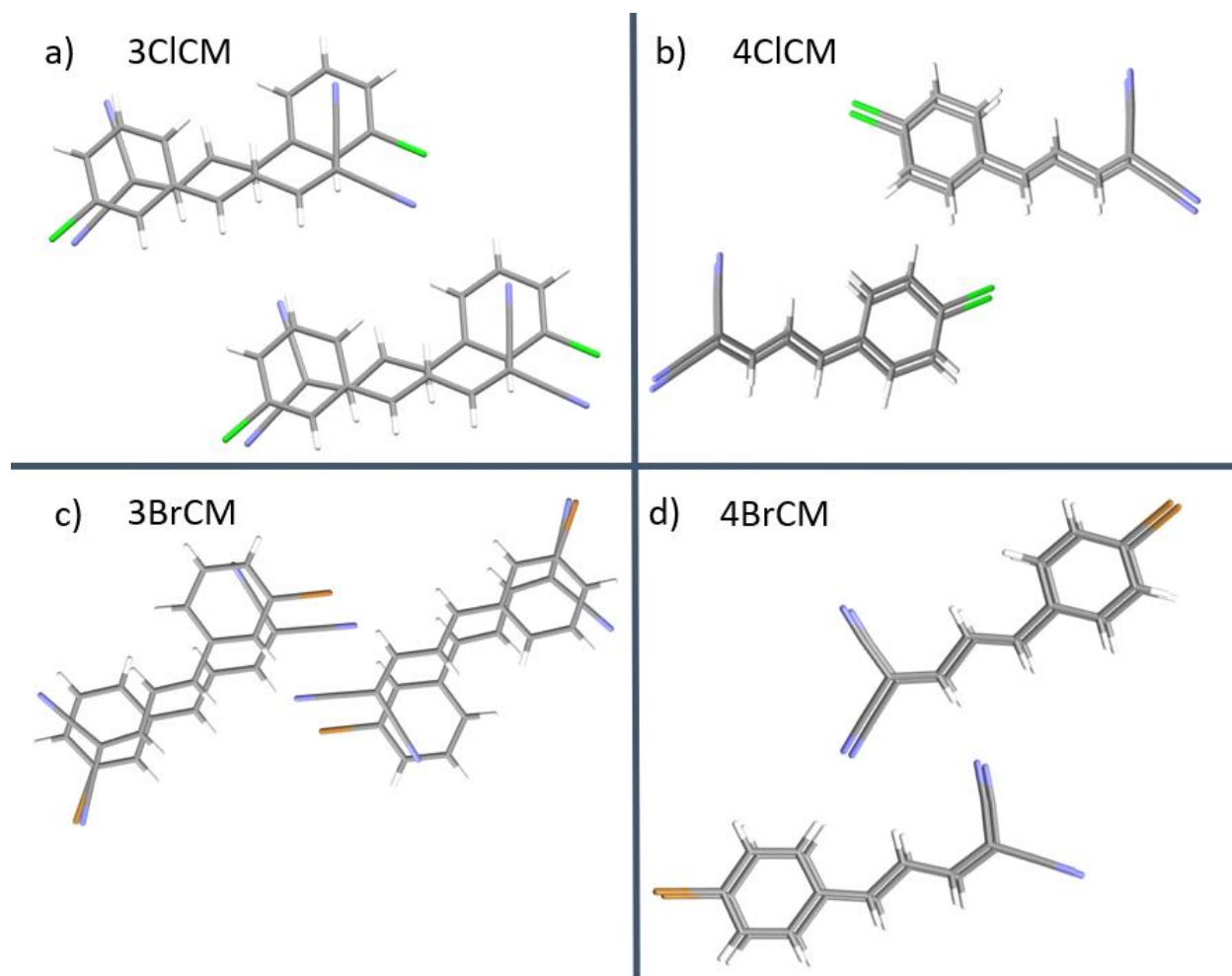


Figure 4: a) for **3ClCM** HT packing while b) **4ClCM** shows HH packing. b) The same trend is seen in c) **3BrCM** and d) **4BrCM**.

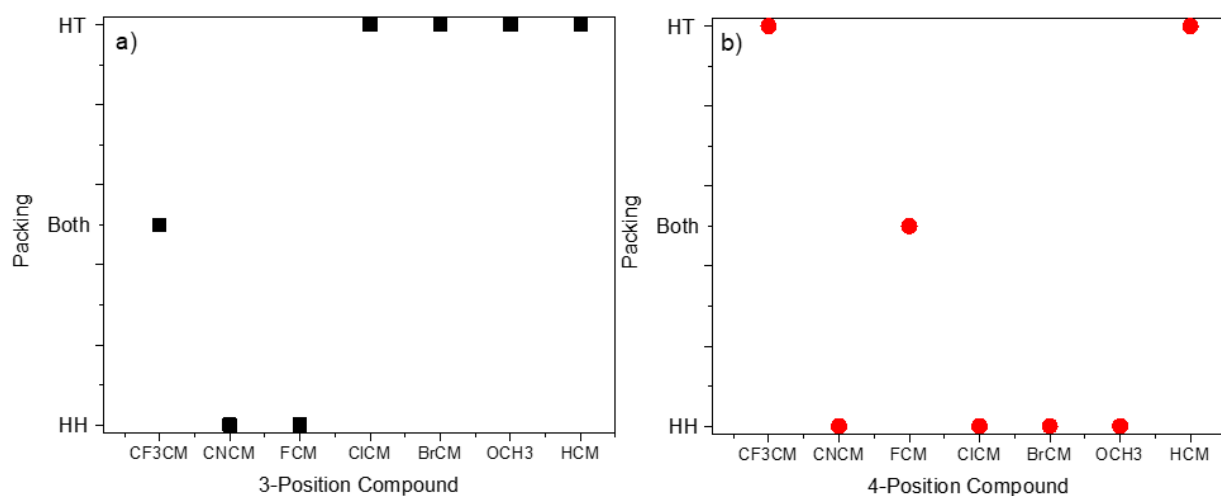


Figure 5: a) The packing trends for the **3XCMs** favoring HT packing. b) the packing trends for the **4XCMs** favoring HH packing.

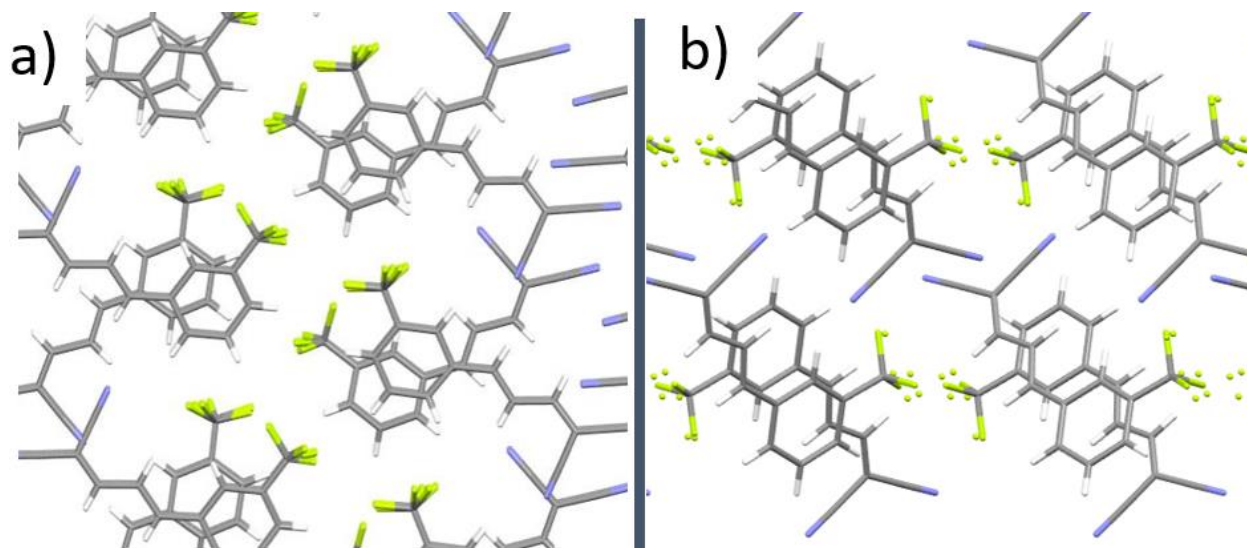


Figure 6: a) **3CF₃CM** gives rise to the expected HH packing which is offset by approximately 45 degrees. b) **3CF₃CM** showing the HT packing motif.

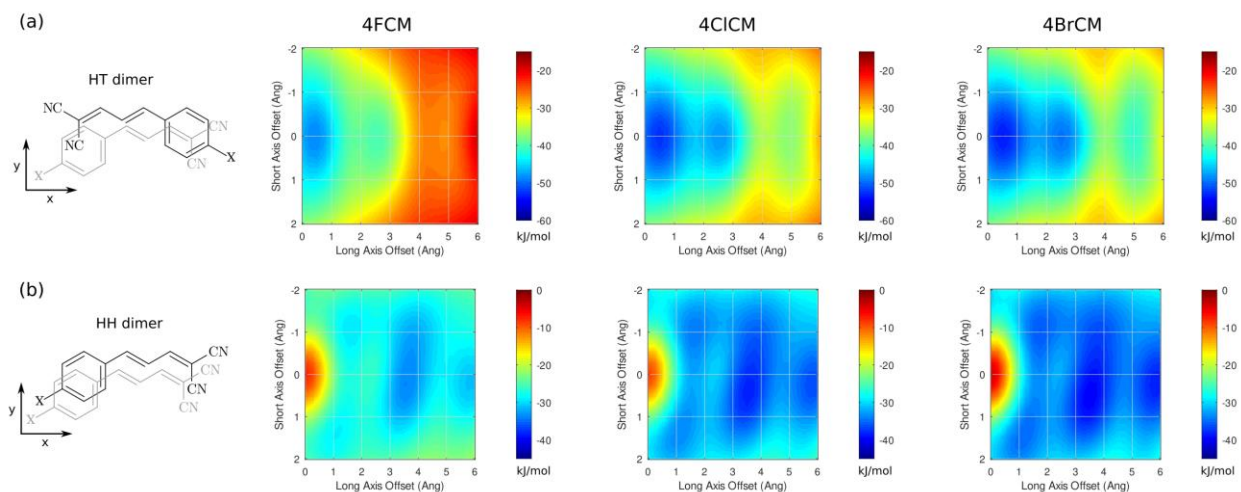


Figure 7: Rigid-molecule SAPT0/jun-cc-pVDZ potential energy scans (kJ/mol) showing how substituting increasingly large halogens in the 4-position impacts the intermolecular interactions. Note that the (a) HT and (b) HH energy scales differ to enable clear visualization of the local minima.

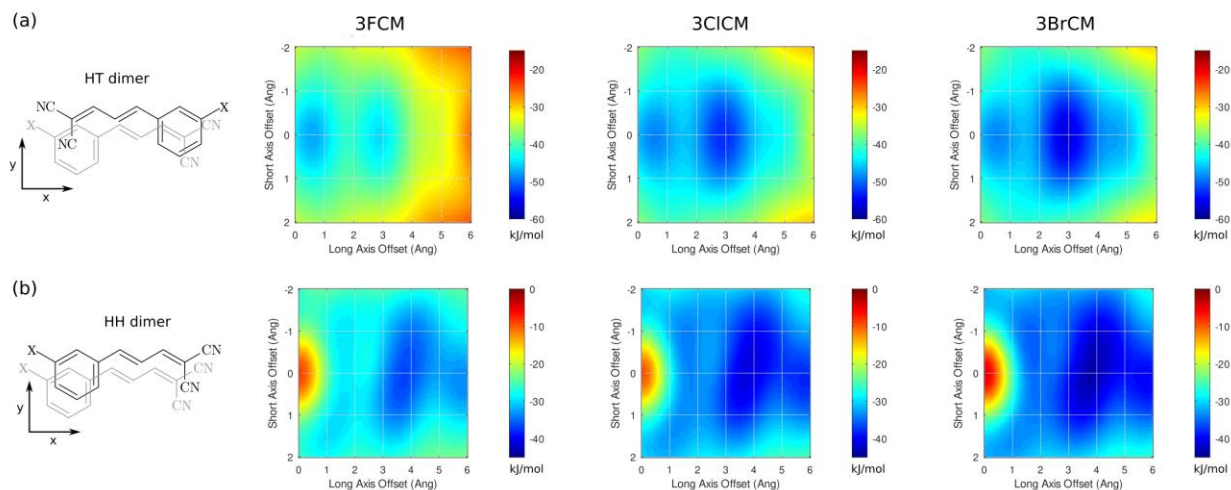


Figure 8: Rigid-molecule SAPT0/jun-cc-pVDZ potential energy scans (kJ/mol) showing how substituting increasingly large halogens in the 3-position impacts the intermolecular interactions. Note that the (a) HT and (b) HH energy scales differ to enable clear visualization of the local minima.

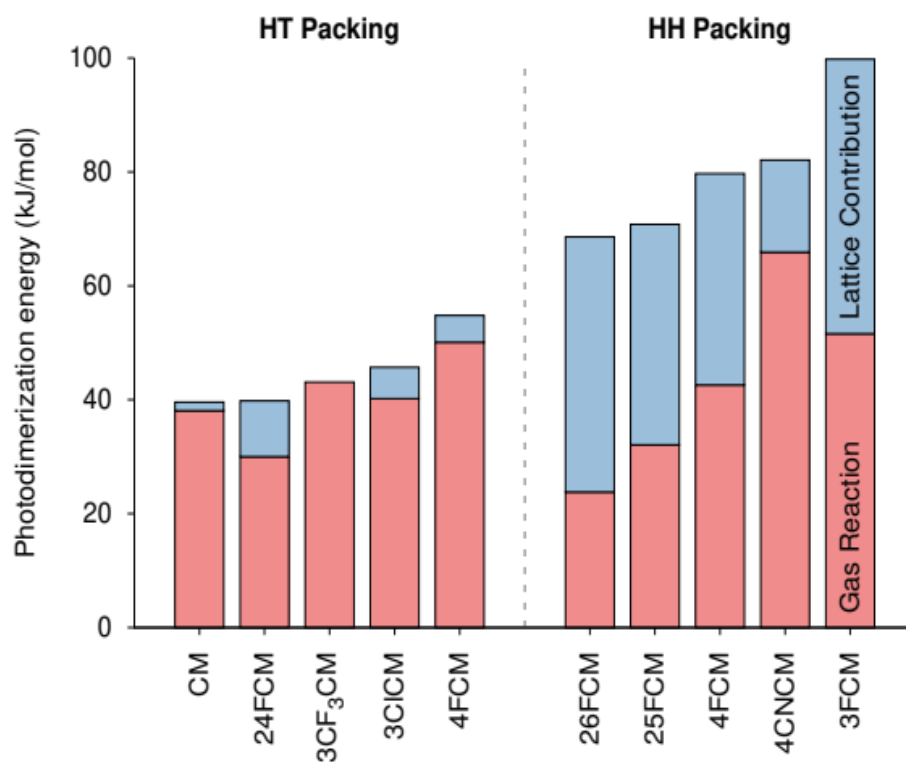
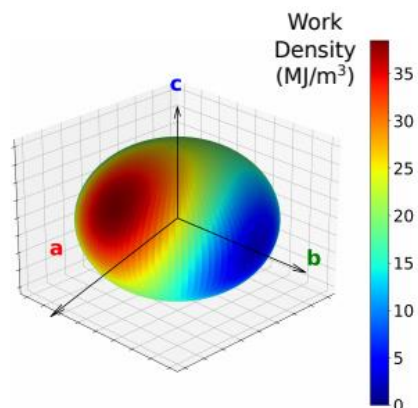
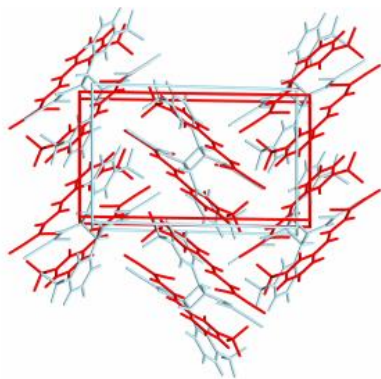


Figure 9: Predicted solid-state photodimerization energies, $E_{SSRD} - 2 E_{monomer}$, for ten **CM** derivatives. The total reaction energies are partitioned into the gas-phase dimer reaction computed in the absence of the surrounding crystal lattice (using the crystalline dimer and SSRD geometries) in red, and the contributions from the surrounding lattice in blue.

a) 3CF₃CM

b (+10.7%)
a (+1.5%)
c (-6.8%)
β (+8.8%)



b) 3CICM

b (+2.4%)
a (+5.7%)
c (-5.9%)
β (+2.9%)

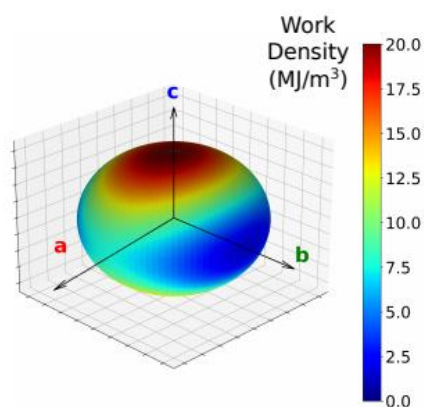
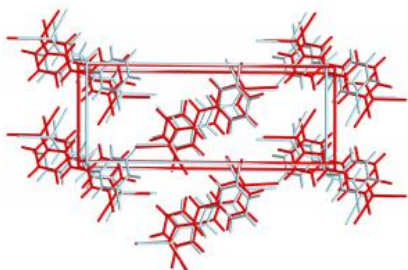


Figure 10: Predicted structural transformations resulting from the [2+2] photodimerization of the reactive polymorphs of (a) **3CICM** and (b) **3CF₃CM**. The computed anisotropic photomechanical work densities (MJ/m^3) are also plotted. The larger change in lattice parameters for **3CF₃CM** results in a maximum work density that is almost twice as large as that for **3CICM**.

- (1) Desiraju, G. R. *Crystal Engineering. The Design of Organic Solids*; Elsevier, 1989.
- (2) Nangia, A. K.; Desiraju, G. R. Crystal Engineering: An Outlook for the Future. *Angew. Chem. Int. Ed.* **2019**, *58*, 4100-4107. DOI: 10.1002/anie.201811313.
- (3) Cohen, M. D.; Schmidt, G. M. J.; Sonntag, F. I. Topochemistry. Part II. The Photochemistry of trans-Cinnamic Acids. *J. Chem. Soc.* **1964**, 2000-2013. DOI: 10.1039/JR9640002000.
- (4) Schmidt, G. M. J. Topochemistry. Part III. The Crystal Chemistry of Some trans-Cinnamic Acids. *J. Chem. Soc.* **1964**, 2014-2021. DOI: 10.1039/JR9640002014.
- (5) Schmidt, G. M. J. Photodimerization in the Solid State. *Pure Appl. Chem.* **1971**, *27* (4), 647-678. DOI: 10.1351/pac197127040647.
- (6) Friscic, T.; MacGillivray, L. R. Single-Crystal-to-Crystal [2+2] Photodimerization: from Discovery to Design. *Z. Kristallogr.* **2005**, *220*, 351-363. DOI: 10.1524/zkri.220.4.351.61621.
- (7) MacGillivray, L. R.; Papaefstathiou, G. S.; Friscic, T.; Hamilton, T. D.; Bucar, D. K.; Chu, Q.; Varshney, D. B.; Georgiev, I. G. Supramolecular control of reactivity in the solid state: from templates to ladderanes to metal-organic frameworks. *Acc. Chem. Res.* **2008**, *41*, 280-291. DOI: 10.1021/ar700145r.
- (8) Hema, K.; Ravi, A.; Raju, C.; Pathan, J. R.; Rai, R.; Sureshan, K. M. Topochemical polymerizations for the solid-state synthesis of organic polymers. *Chem. Soc. Rev.* **2021**, *50*, 4062-4099. DOI: 10.1039/d0cs00840k.
- (9) Naumov, P.; Kowalik, J.; Solntsev, K. M.; Baldrige, A.; Moon, J.-S.; Kranz, C.; Tolbert, L. M. Topochemistry and photomechanical effects in crystals of green fluorescent protein-like chromophores: effects of hydrogen bonding and crystal packing. *J. Am. Chem. Soc.* **2010**, *132*, 5845-5857. DOI: 10.1021/ja100844m.
- (10) Kim, T.; Zhu, L.; Mueller, L. J.; Bardeen, C. J. Dependence of the solid-state photomechanical response of 4-chlorocinnamic acid on crystal shape and size. *CrystEngComm* **2012**, *14*, 7792-7799. DOI: 10.1039/C2CE25811K.
- (11) Wang, H.; Chen, P.; Wu, Z.; Zhao, J.; Sun, J.; Lu, R. Bending, Curling, Rolling, and Salient Behavior of Molecular Crystals Driven by [2+2] Cycloaddition of a Styrylbenzoxazole Derivative. *Angew. Chem. Int. Ed.* **2017**, *56*, 9463-9467. DOI: 10.1002/anie.201705325.
- (12) Peng, J.; Ye, K.; Liu, C.; Sun, J.; Lu, R. The photomechanical effects of the molecular crystals based on 5-chloro-2-(naphthalenylvinyl)benzoxazoles fueled by topo-photochemical reactions. *J. Mater. Chem. C* **2019**, *7*, 5433-5441. DOI: 10.1039/c9tc01084j.
- (13) Shen, J. L. K. Y. Y.; Peng, J.; Sun, J.; Lu, R. Photoactuators based on the dynamic molecular crystals of naphthalene acrylic acids driven by stereospecific [2+2] cycloaddition reactions. *J. Mater. Chem. C* **2020**, *8*, 3165-3175. DOI: 10.1039/c9tc06689f.
- (14) Shu, Y.; Ye, K.; Yue, Y.; Sun, J.; Haoran Wang; Zhong, J.; Yang, X.; Gao, H.; Lu, R. Fluorine as a robust balancer for tuning the reactivity of topo-photoreactions of chalcones and the photomechanical effects of molecular crystals. *CrystEngComm* **2021**, 5856-5868. DOI: 10.1039/d1ce00086a.

- (15) Chen, Y.-R.; Jia, M.-Z.; Pan, J.-Q.; Tan, B.; Zhang, J. Photomechanical behavior triggered by [2 + 2] cycloaddition and photochromism of a pyridinium-functionalized coordination complex. *Dalton Trans.* **2022**, *51*, 6157-6161. DOI: 10.1039/D2DT00599A.
- (16) Xu, T.-Y.; Tong, F.; Xu, H.; Wang, M.-Q.; Tian, H.; Qu, D.-H. Engineering Photomechanical Molecular Crystals to Achieve Extraordinary Expansion Based on Solid-State [2 + 2] Photocycloaddition. *J. Am. Chem. Soc.* **2022**, *144*, 6278–6290. DOI: 10.1021/jacs.1c12485.
- (17) Wang, L.; Qiao, S.-B.; Chen, Y.-T.; Ma, X.; Wei, W.-M.; Zhang, J.; Du, L.; Zhao, Q.-H. [2 + 2] cycloaddition and its photomechanical effects on 1D coordination polymers with reversible amide bonds and coordination site regulation. *Chem. Sci.* **2024**, *15*, 3971-3979. DOI: 10.1039/D3SC06098E.
- (18) Medishetty, R.; Husain, A.; Bai, Z.; Runceviski, T.; Dinnebier, R. E.; Naumov, P.; Vittal, J. J. Single crystals popping under UV light: a photosalient effect triggered by a [2+2] cycloaddition reaction. *Angew. Chem. Int. Ed.* **2014**, *53*, 5907-5911. DOI: 10.1002/anie.201402040.
- (19) Kole, G. K.; Kojima, T.; Kawano, M.; Vittal, J. J. Reversible Single-Crystal-to-Single-Crystal Photochemical Formation and Thermal Cleavage of a Cyclobutane Ring. *Angew. Chem. Int. Ed.* **2014**, *53*, 2143–2146. DOI: 10.1002/anie.201306746.
- (20) Medishetty, R.; Sahoo, S. C.; Mulijanto, C. E.; Naumov, P.; Vittal, J. J. Photosalient Behavior of Photoreactive Crystals. *Chem. Mater.* **2015**, *27*, 1821-1829. DOI: 10.1021/acs.chemmater.5b00021.
- (21) Yadava, K.; Vittal, J. J. Photosalient Behavior of Photoreactive Zn(II) Complexes. *Cryst. Growth De.* **2019**, *19*, 2542-2547. DOI: 10.1021/acs.cgd.9b00260.
- (22) Rath, B. B.; Vittal, J. J. Single-Crystal-to-Single-Crystal [2 + 2] Photocycloaddition Reaction in a Photosalient One-Dimensional Coordination Polymer of Pb(II). *J. Am. Chem. Soc.* **2020**, *142*, 20117–20123. DOI: 10.1021/jacs.0c09577.
- (23) Rath, B. B.; Vittal, J. J. Photoreactive Crystals Exhibiting [2 + 2] Photocycloaddition Reaction and Dynamic Effects. *Acc. Chem. Res.* **2022**, *55*, 1445–1455. DOI: 10.1021/acs.accounts.2c00107.
- (24) Naumov, P.; Sahoo, S. C.; Zakharov, B. A.; Boldyreva, E. V. Dynamic Single Crystals: Kinematic Analysis of Photoinduced Crystal Jumping (The Photosalient Effect). *Angew. Chem. Int. Ed.* **2013**, *52*, 9990–9995. DOI: 10.1002/anie.201303757.
- (25) McGehee, K.; Saito, K.; Kwaria, D.; Minamikawa, H.; Norikane, Y. Releasing a bound molecular spring with light: a visible light-triggered photosalient effect tied to polymorphism. *Phys. Chem. Chem. Phys.* **2024**, *26*, 6834-6843. DOI: 10.1039/D3CP04691E.
- (26) Tong, F.; Xu, W.; Guo, T.; Lui, B. F.; Hayward, R. C.; Palffy-Muhoray, P.; Al-Kaysi, R. O.; Bardeen, C. J. Photomechanical molecular crystals and nanowire assemblies based on the [2+2] photodimerization of a phenylbutadiene derivative. *J. Mater. Chem. C* **2020**, *8*, 5036-5044. DOI: 10.1039/C9TC06946A.
- (27) Row, T. N. C.; Swamy, H. R.; Acharyaa, K. R.; Ramamurthy, V.; Venkatesan, K.; Rao, C. N. R. Reversible Photodimerization of Phenylbutadienes in the Solid State. *Tet. Lett.* **1983**, 3263-3266. DOI: 10.1016/S0040-4039(00)88152-6.
- (28) Gately, T. J.; Cook, C.; Almuzarie, R.; Islam, I.; Gardner, Z.; Iulicci, R. J.; Al-Kaysi, R. O.; Beran, G. J. O.; Bardeen, C. J. Effect of Fluorination on the Polymorphism and Photomechanical Properties of Cinnamalmalononitrile Crystals. *Cryst. Growth. Des.* **2022**, *22*, 7298–7307. DOI: 10.1021/acs.cgd.2c00930.
- (29) Szalewicz, K. Symmetry-adapted perturbation theory of intermolecular forces. *WIREs Comp. Molec. Sci.* **2012**, *2*, 254-272. DOI: 10.1002/wcms.86.
- (30) Hohenstein, E. G.; Sherrill, C. D. Density fitting of intramonomer correlation effects in symmetry-adapted perturbation theory. *J. Chem. Phys.* **2010**, *133*, 014101. DOI: 10.1063/1.3451077.
- (31) Smith, D. G. A.; Burns, L. A.; Simmonett, A. C.; Parrish, R. M.; Schieber, M. C.; Galvelis, R.; Kraus, P.; Kruse, H.; Di Remigio, R.; Alenaizan, A.; et al. Psi4 1.4: Open-source software for high-throughput quantum chemistry. *J Chem Phys* **2020**, *152* (18), 184108. DOI: 10.1063/5.0006002 From NLM PubMed-not-MEDLINE.

- (32) Papajak, E.; Truhlar, D. G. What are the most efficient basis set strategies for correlated wave function calculations of reaction energies and barrier heights? *J. Chem. Phys.* **2012**, *137*, 064110. DOI: 10.1063/1.4738980.
- (33) Parker, T. M.; Burns, L. A.; Parrish, R. M.; Ryno, A. G.; Sherrill, C. D. Levels of symmetry adapted perturbation theory (SAPT). I. Efficiency and performance for interaction energies. *J. Chem. Phys.* **2014**, *140*, 094106. DOI: 10.1063/1.4867135.
- (34) Giannozzi, P.; Andreussi, O.; Brumme, T.; Bunau, O.; Nardelli, M. B.; Calandra, M.; Car, R.; Cavazzoni, C.; Ceresoli, D.; Cococcioni, M.; et al. Advanced capabilities for materials modelling with Quantum ESPRESSO. *J. Phys.: Condens. Matter* **2017**, *29*, 465901. DOI: 10.1088/1361-648X/aa8f79.
- (35) Becke, A. D. On the large-gradient behavior of the density functional exchange energy. *J. Chem. Phys.* **1986**, *85*, 7184-7187. DOI: 10.1063/1.451353.
- (36) Perdew, J. P.; Burke, K.; Ernzerhof, M. Generalized Gradient Approximation Made Simple. *Phys. Rev. Lett.* **1996**, *77*, 3865-3868. DOI: 10.1103/PhysRevLett.77.3865.
- (37) Otero-de-la-Roza, A.; Johnson, E. R. Van der Waals interactions in solids using the exchange-hole dipole moment model. *J. Chem. Phys.* **2012**, *136*, 174109. DOI: 10.1063/1.4705760.
- (38) Bryenton, K. R.; Adeleke, A. A.; Dale, S. G.; Johnson, E. R. Delocalization error: The greatest outstanding challenge in density-functional theory. *WIREs Comp. Molec. Sci.* **2023**, *13*, e1631. DOI: 10.1002/wcms.1631.
- (39) Beran, G. J. O.; Greenwell, C.; Cook, C.; Řezáč, J. Improved Description of Intra- and Intermolecular Interactions through Dispersion-Corrected Second-Order Møller–Plesset Perturbation Theory. *Acc. Chem. Res.* **2023**, *23*, 3525–3534. DOI: 10.1021/acs.accounts.3c00578.
- (40) Beran, G. J. O. Solid state photodimerization of 9-tert-butyl anthracene ester produces an exceptionally metastable polymorph according to firstprinciples calculations. *Cryst. Eng. Comm.* **2019**, *21*, 758–764. DOI: 10.1039/c8ce01985a.
- (41) Greenwell, C.; Beran, G. J. O. Inaccurate Conformational Energies Still Hinder Crystal Structure Prediction in Flexible Organic Molecules. *Cryst. Growth Des.* **2020**, *20*, 4875–4881. DOI: 10.1021/acs.cgd.0c00676.
- (42) Santra, G.; Sylvetsky, N.; Martin, J. M. L. Minimally Empirical Double-Hybrid Functionals Trained against the GMTKN55 Database: revDSD-PBEP86-D4, revDOD-PBE-D4, and DOD-SCAN-D4. *J. Phys. Chem. A* **2019**, *123*, 5129–5143. DOI: 10.1021/acs.jpca.9b03157.
- (43) Neese, F. The ORCA program system. *WIREs Comp. Molec. Sci.* **2012**, *2*, 73-78. DOI: 10.1002/wcms.81. Citations: 8,197.
- (44) Cook, C. J.; Li, W.; Lui, B. F.; Thomas J. Gately; Al-Kaysi, R. O.; Mueller, L. J.; Bardeen, C. J.; Beran, G. J. O. A theoretical framework for the design of molecular crystal engines. *Chem. Sci.* **2023**, *14*, 937-949. DOI: 10.1039/D2SC05549J.
- (45) Cook, C. J.; Perry, C. J.; Beran, G. J. O. Organic Crystal Packing Is Key to Determining the Photomechanical Response. *J. Phys. Chem. Lett.* **2023**, *14*, 6823–6831. DOI: 10.1021/acs.jpcllett.3c01676.
- (46) Uscumlic, G. S.; Krstic, V. V.; Muskatirovic, M. D. Correlation of Ultraviolet Absorption Frequencies of Cis and Trans Substituted Cinnamic Acids with Hammett Substituent Constants. *J. Molec. Struct.* **1988**, *174*, 251-254. DOI: 10.1016/0022-2860(88)80166-2.
- (47) Barker, C. C.; Bride, M. H.; Hallas, G.; Stamp, A. Steric Effects in Di- and Tri-arylmethanes. Part III. Electronic Absorption Spectra of Derivatives of Nalachite Green containing Substituents in the Phenyl Ring. *J. Chem. Soc.* **1961**, 1285-1290. DOI: 10.1039/JR9610001285.
- (48) st, Y. D.; Yildirim, M. Synthesis, UV–Vis spectra, and Hammett correlation of some novel bis(dihydropyrrolo[3,4-c]pyrazoles). *Monatsh. Chem.* **2010**, *141*, 961–973. DOI: 10.1007/s00706-010-0351-z.
- (49) Beek, L. K. H. v. A relationship between dipole moments and the Hammett equation. *Rec. Travaux Chimie Pays-Bas* **1957**, *76*, 729-732. DOI: 10.1002/recl.19570760908.

- (50) Rao, C. N. R.; Wahl, W. H.; Williams, E. J. A Correlation of Electric Dipole Moments of Substituted Benzenes by Reactivities. *Can. J. Chem.* **1957**, *35*, 1575-1578. DOI: 10.1139/v57-20.
- (51) Ramamurthy, V.; Venkatesan, K. Photochemical reactions of organic crystals. *Chem. Rev.* **1987**, *87*, 433–481. DOI: 10.1021/cr00078a009.
- (52) Gately, T. J.; Sontising, W.; Easley, C. J.; Islam, I.; Al-Kaysi, R. O.; Beran, G. J. O.; Bardeen, C. J. Effect of halogen substitution on energies and dynamics of reversible photomechanical crystals based on 9-anthracenecarboxylic acid. *CrystEngComm* **2021**, *23*, 5931–5943. DOI: 10.1039/d1ce00846c.

Supporting Information

S1: Crystal packing

Figure S1: **3ClCM** crystal packing

Figure S2: **4ClCM** crystal packing

Figure S3: **3BrCM** crystal packing

Figure S4: **4BrCM** crystal packing

Figure S5: **3CF₃CM** crystal packing

Figure S6: **4CF₃CM** crystal packing

Figure S7: **3CN₂CM** crystal packing

Figure S8: **4CN₂CM** Crystal packing

Figure S9: **3Methoxy-CM** crystal packing

Figure S10: **34FCM** crystal packing

Figure S11: **236FCM** crystal packing

Figure S12: **25FCM** crystal packing

S2: Experimental

S2.1: Synthesis of (E)-3-Chloro-cinnamalmalononitrile (**3ClCM**)

S2.2: Synthesis of (E)-4-Chloro-cinnamalmalononitrile (**4ClCM**)

S2.3: Synthesis of (E)- 3-Cyano-cinnamalmalononitrile (**3CN₂CM**)

S2.4: Synthesis of (E)- 4-Cyano-cinnamalmalononitrile (**4CN₂CM**)

S2.5: Synthesis of (E)- 3-Bromo-cinnamalmalononitrile (**3BrCM**)

S2.6: Synthesis of (E)- 4-Bromo-cinnamalmalononitrile (**4BrCM**)

S2.7: Synthesis of (E)-3-Tri-fluoro methyl-cinnamalmalononitrile (**3CF₃CM**)

S2.8: Synthesis of (E)-4-Tri-fluoro methyl-cinnamalmalononitrile (**4CF₃CM**)

S2.9: Synthesis of (E)-3-Methoxy-cinnamalmalononitrile (**3Methoxy-CM**)

S2.10: Synthesis of (E)- 2,3,6-tri-fluoro-cinnamalmalononitrile (**236FCM**)

S2.11: Synthesis of (E)- 3,4-di-fluoro-cinnamalmalononitrile (**34FCM**)

S2.12: Synthesis of (E)-2,5-di-fluoro-cinnamalmalononitrile (**25FCM**)

S2.13: Solid-state photodimerization of **3CF₃CM**

S3: NMR Spectra of compounds

Figure S13: ^1H NMR spectra trans-3-Chlorocinnamaldehyde
Figure S14A: **3ClCM** ^1H NMR spectra
Figure S14B: **3ClCM** ^{13}C NMR spectra
Figure S15: ^1H NMR spectrum of trans-4-Chlorocinnamaldehyde
Figure S16A: **4ClCM** ^1H NMR spectra
Figure S16B: **4ClCM** ^{13}C NMR spectra
Figure S17: ^1H NMR spectra of trans-3-Cyanocinnamaldehyde
Figure S18A: **3CNCM** ^1H NMR spectra
Figure S18B: **3CNCM** ^{13}C NMR spectra
Figure S19: ^1H NMR spectra of trans-4-Cyanocinnamaldehyde
Figure S20A: **4CNCM** ^1H NMR spectra
Figure S20B: **4CNCM** ^{13}C NMR spectra
Figure S21A: **3BrCM** ^1H NMR spectra
Figure S21B: **3BrCM** ^{13}C NMR spectra
Figure S22A: **4BrCM** ^1H NMR spectra
Figure S22B: **4BrCM** ^{13}C NMR spectra
Figure S23A: **3CF₃CM** ^1H NMR spectra
Figure S23B: **3CF₃CM** ^{13}C NMR spectra
Figure S24: ^1H NMR spectra of trans-4-Trifluoromethylcinnamaldehyde
Figure S25A: **4CF₃CM** ^1H NMR spectra
Figure S25B: **4CF₃CM** ^{13}C NMR spectra
Figure S26A: **3MethoxyCM** ^1H NMR spectra
Figure S26B: **3MethoxyCM** ^{13}C NMR spectra
Figure S27: ^1H NMR spectra of trans-2,3,6-Trifluorocinnamaldehyde
Figure S28A: **3MethoxyCM** ^1H NMR spectra
Figure S28B: **3MethoxyCM** ^{13}C NMR spectra
Figure S29: ^1H NMR spectra of trans-3,4-Difluorocinnamaldehyde
Figure S30A: **34FCM** ^1H NMR spectra
Figure S30B: **34FCM** ^{13}C NMR spectra
Figure S31: ^1H NMR spectra of trans-2,5-Difluorocinnamaldehyde
Figure S32A: **25FCM** ^1H NMR spectra

Figure S32B: **25FCM** ^{13}C NMR spectra

Figure S33: ^1H NMR spectra of the **3CF3CM** dimer

S4: Crystal Structure data and collection procedures for various **CMs**

Table S1: Crystal Data and Structure Refinement for various **CMs**.

S4.1: Collection parameters for crystal structure data for **34FCM**

S4.2: Collection parameters for crystal structure data for **236FCM**

S4.3: Collection parameters for crystal structure data for **25FCM**

S4.4: Collection parameters for crystal structure data for **4CF3CM**

S4.5: Collection parameters for crystal structure data for **3CICM** (colorless)

S4.6: Collection parameters for crystal structure data for **3CICM** (yellow)

S4.7: Collection parameters for crystal structure data for **4CICM**

S4.8: Collection parameters for crystal structure data for **3MethoxyCM**

S4.9: Collection parameters for crystal structure data for **4BrCM**

S4.10: Collection parameters for crystal structure data for **3BrCM**

S4.11: Collection parameters for crystal structure data for **3CNM**

S4.12: Collection parameters for crystal structure data for **4CNM**

S4.13: Collection parameters for crystal structure data for **3FC3CM** (nonreactive)

S4.14: Collection parameters for crystal structure data for **3CF3CM** (reactive)

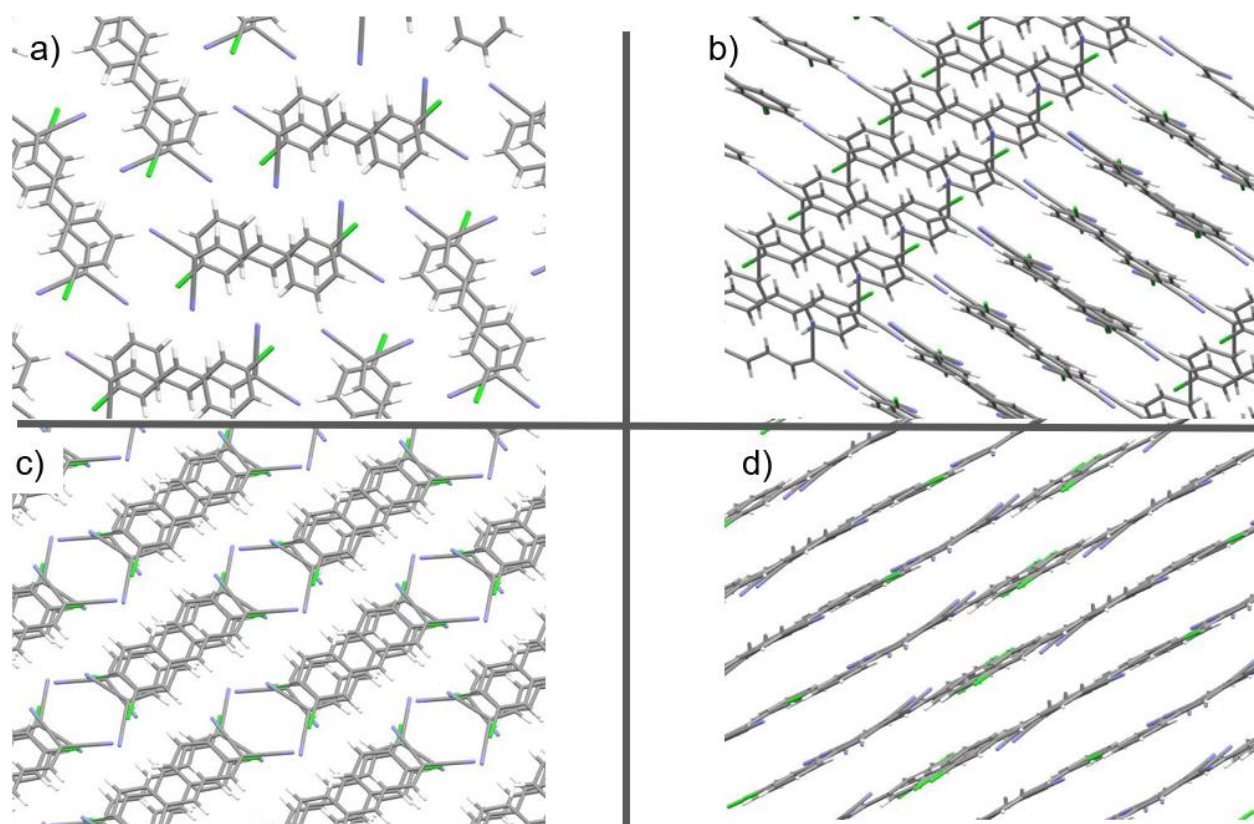


Figure S1: 3CICM crystal packing showing the in a) top and b) side and the yellow blocks in c) top and d) side views

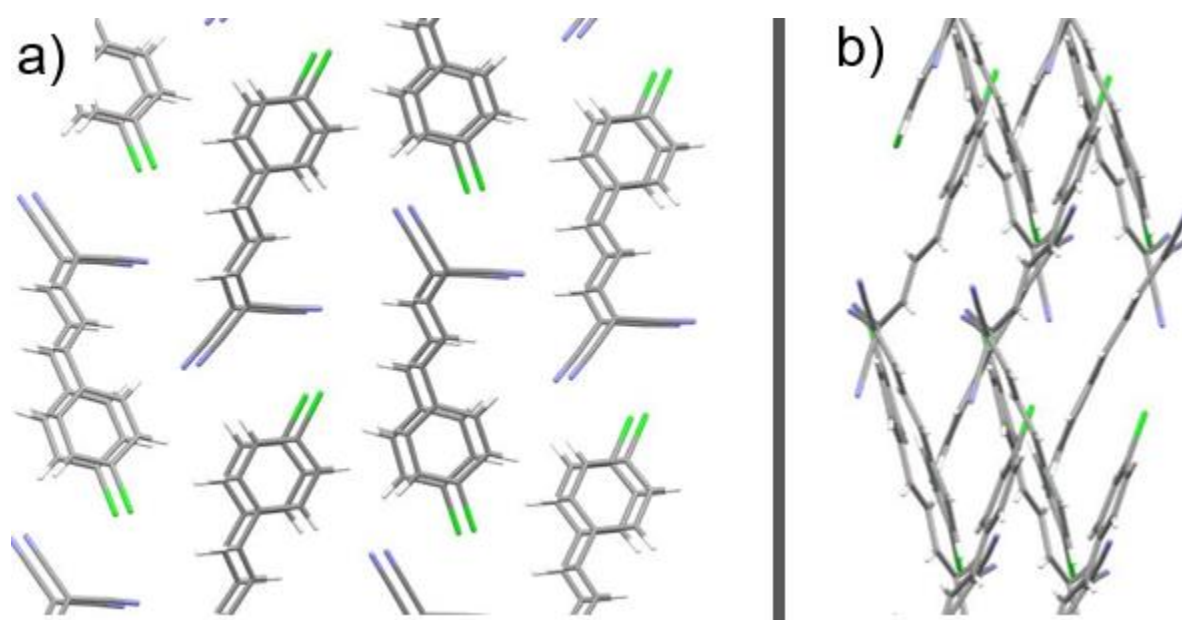


Figure S2: 4CICM crystal packing showing from a) the top b) side of the crystal

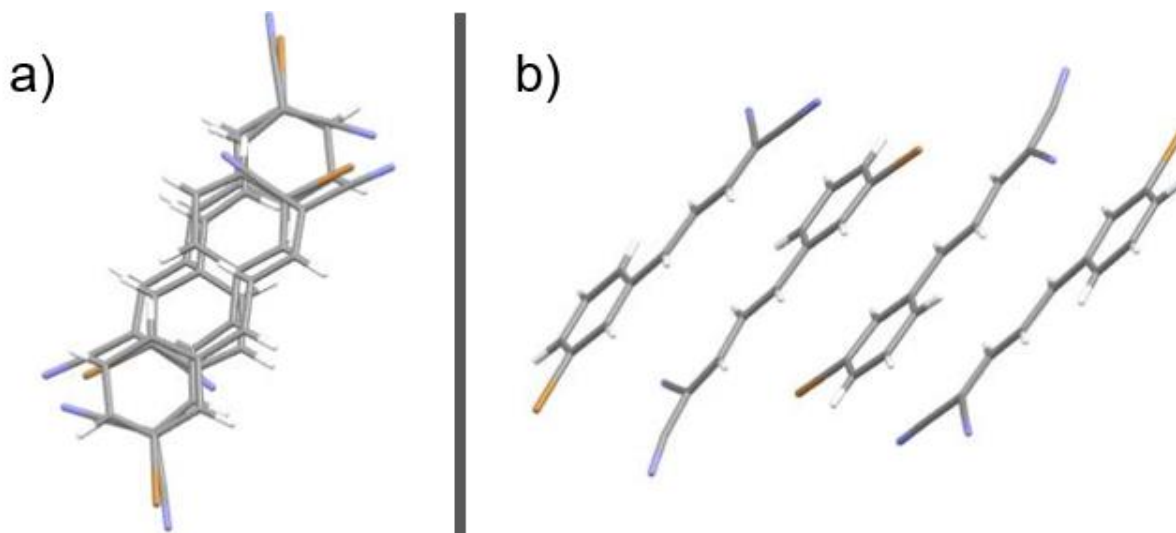


Figure S3: 3BrCM crystal packing shown from the a) top and b) side of the crystal

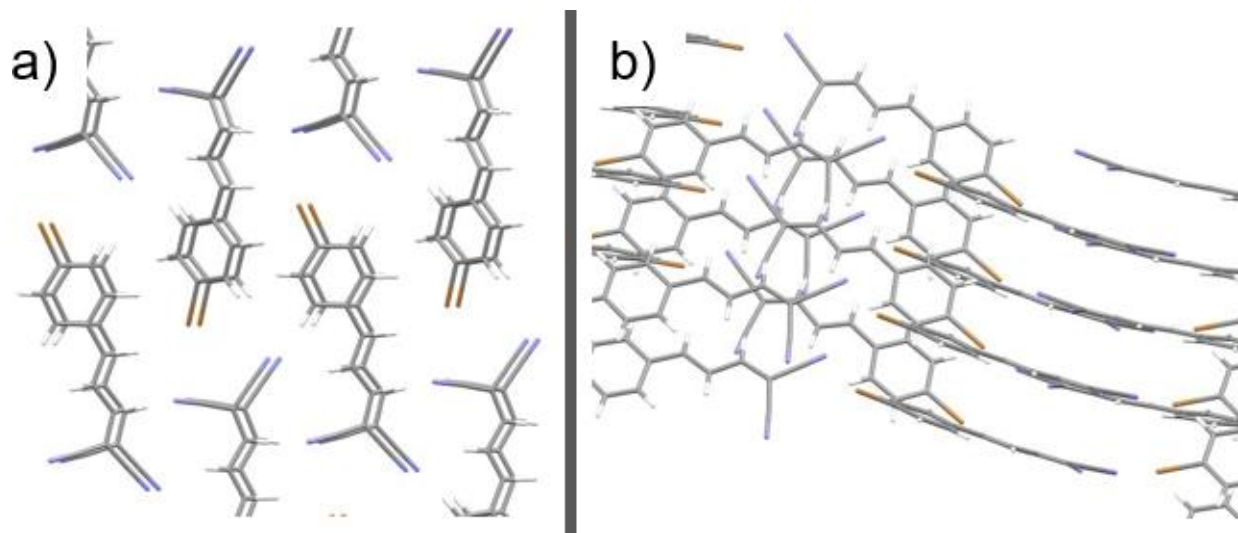


Figure S4: 4BrCM crystal packing shown from the a) top and b) side of the crystal

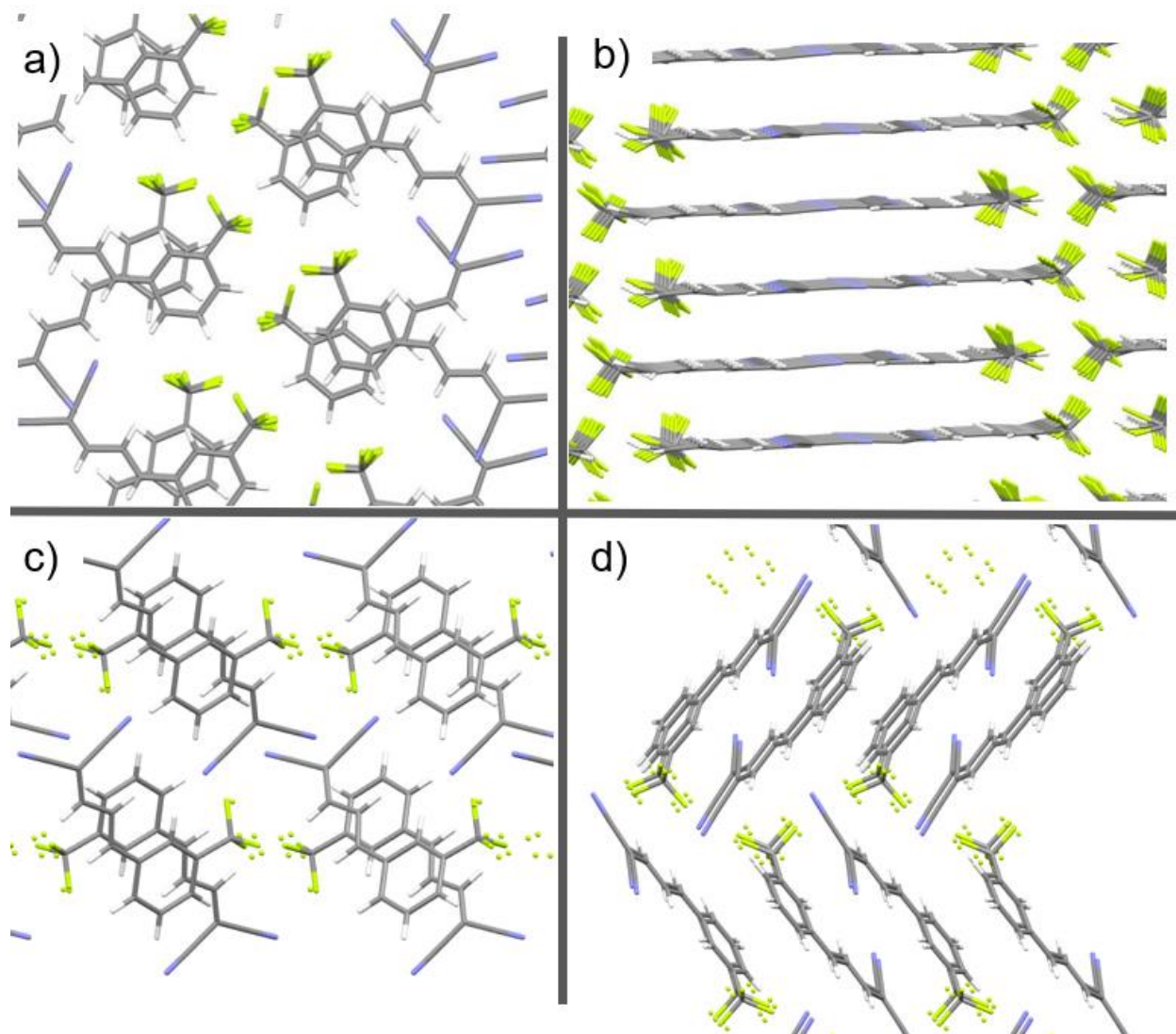


Figure S5: 3CF3CM crystal packing shown from the a) top and b) side of the crystal nonreactive crystal and the c) top and d) side of the reactive crystal

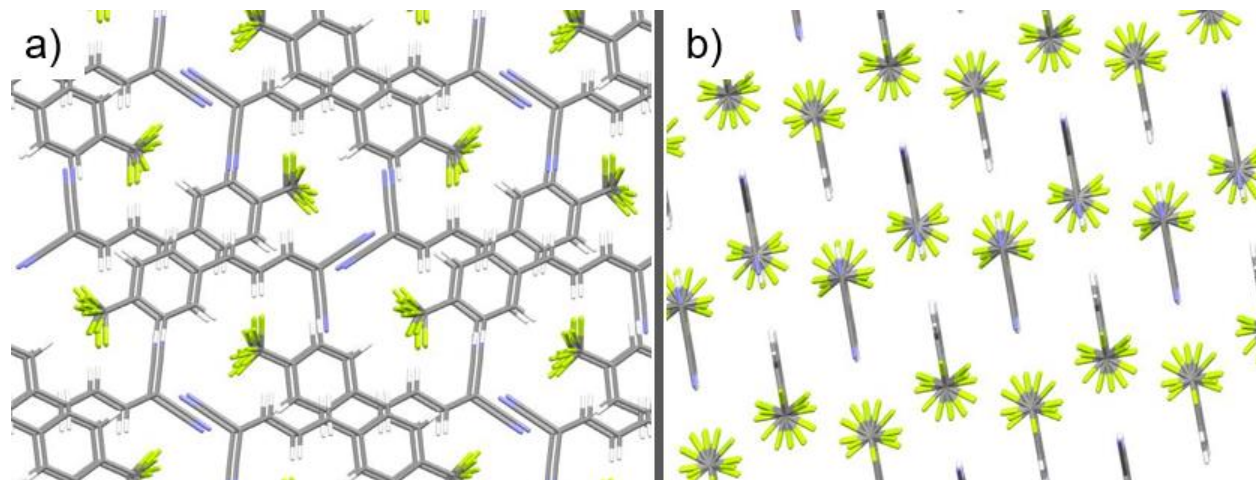


Figure S6: 4CF3CM crystal packing shown from the a) top and b) side of the crystal

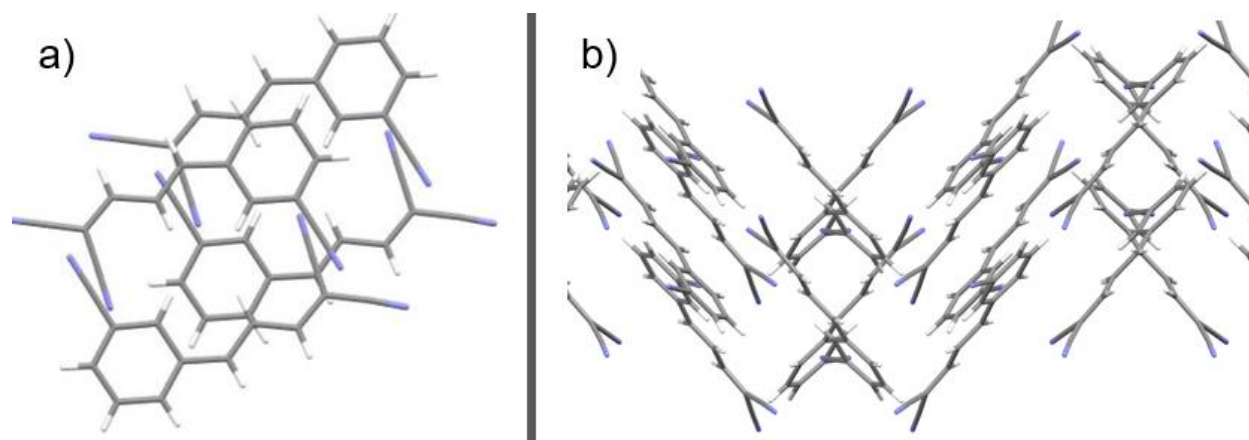


Figure S7: 3CNM crystal packing shown from the a) top and b) side of the crystal

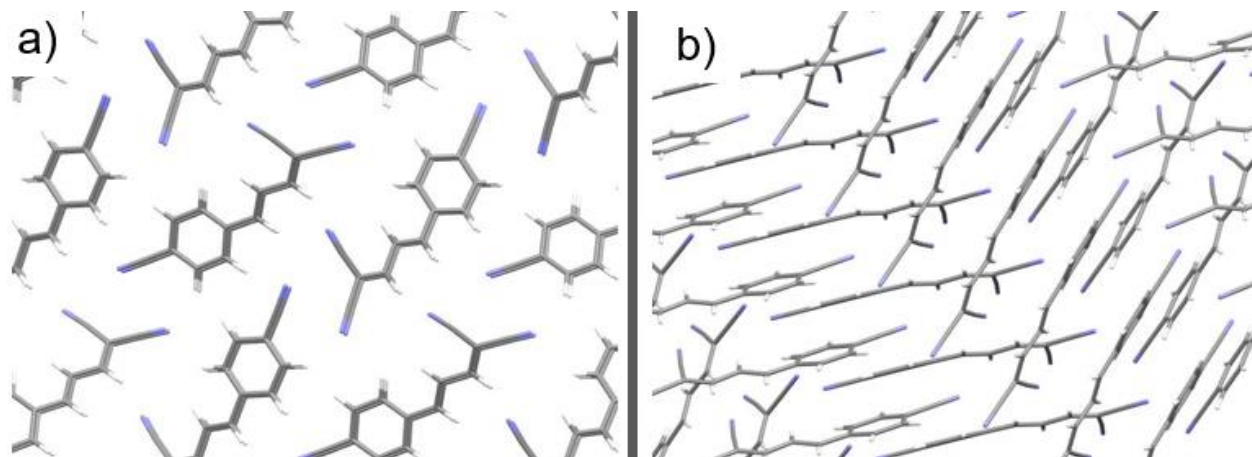


Figure S8: 4CNCM crystal packing shown from the a) top and b) side of the crystal

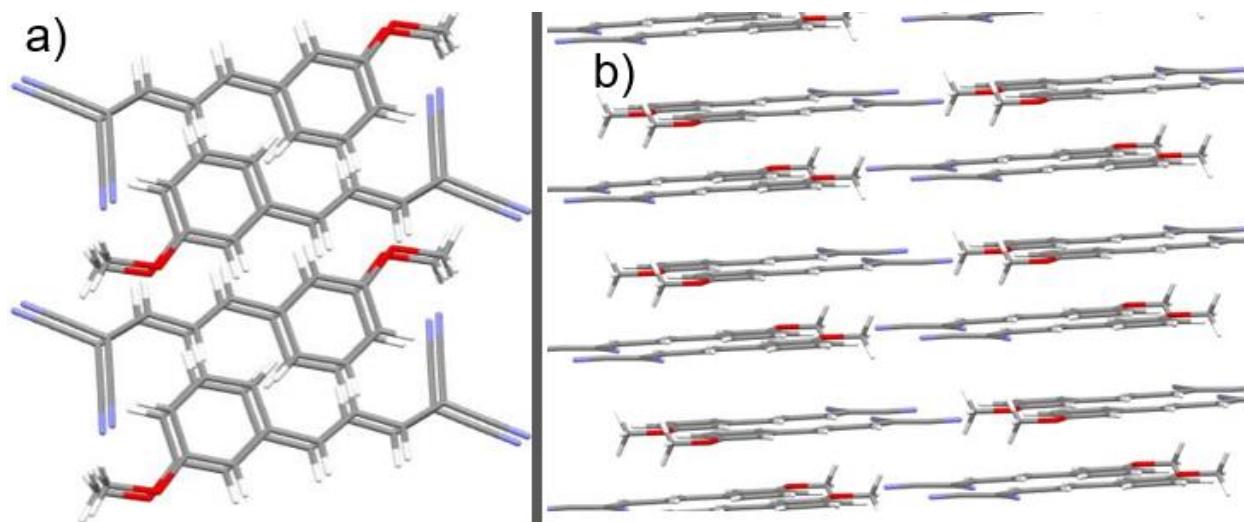


Figure S9: 3MethoxyCM crystal packing shown from the a) top and b) side of the crystal

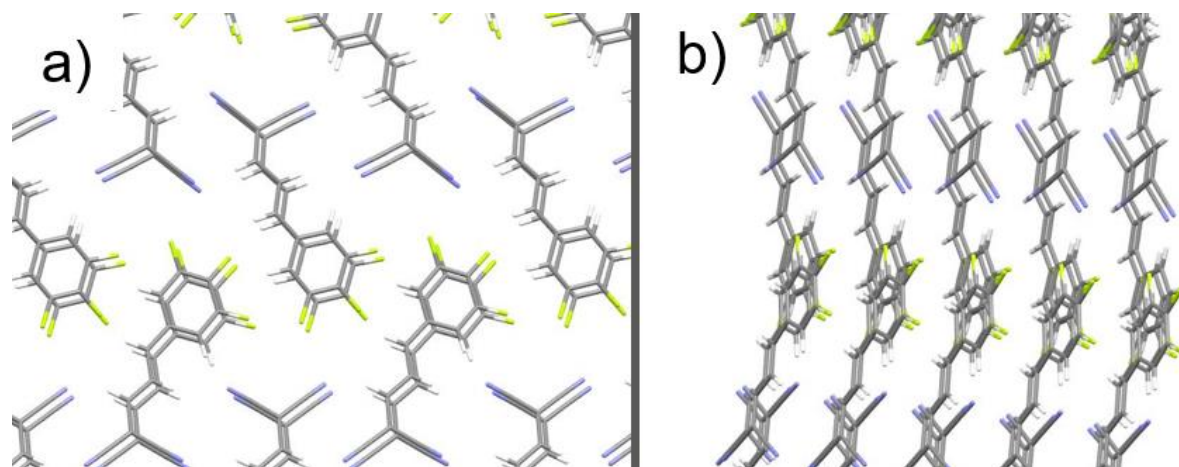


Figure S10: 34FCM crystal packing shown from the a) top and b) side of the crystal

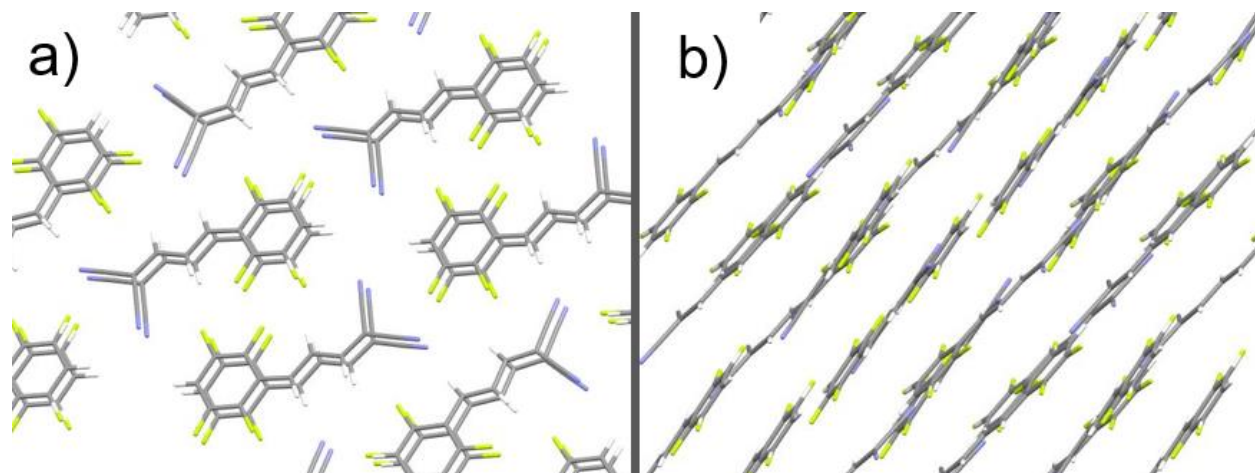


Figure S11: 236FCM crystal packing shown from the a) top and b) side of the crystal

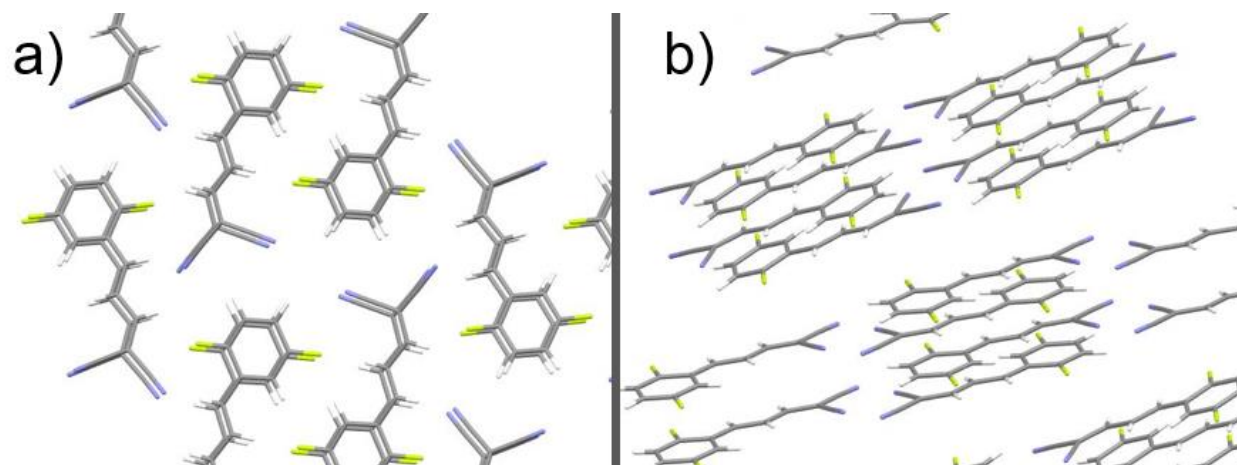


Figure S12: 25FCM crystal packing shown from the a) top and b) side of the crystal

S.2 Experimental

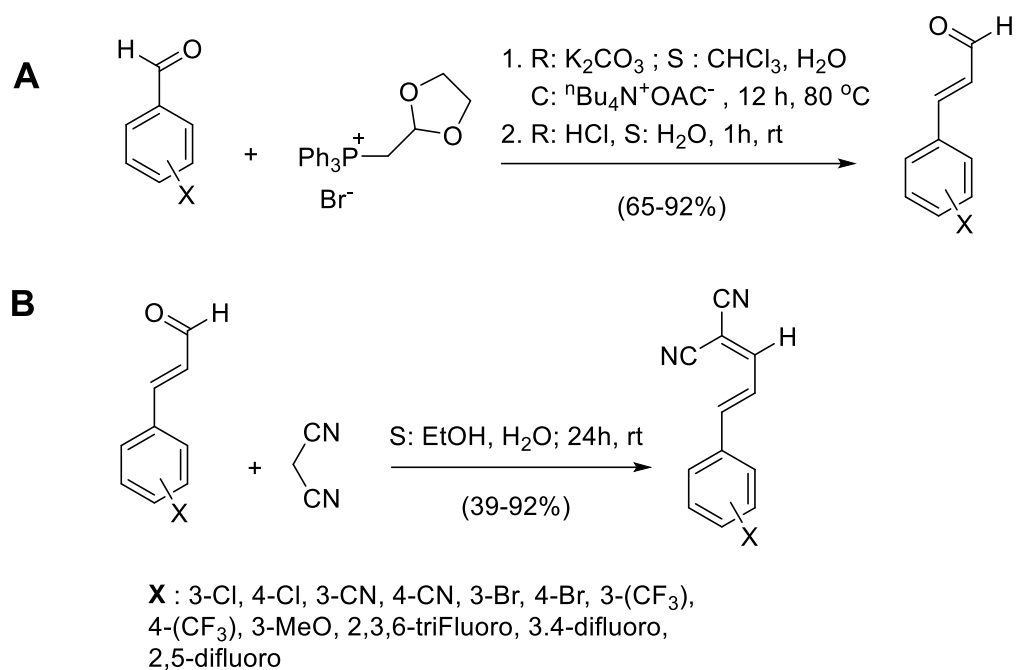
Synthesis of 3ClCM, 4ClCM, 3CNM, 4CNM, 3BrCM, 4BrCM, 3CF₃CM, 4CF₃CM, 3MeOCM, (2,3,6)FCM, (3,4)FCM, (2,5)FCM was conducted using the following reagents and procedure.

Reagents: 3-Chlorobenzaldehyde (98%), 4-Chlorobenzaldehyde (99%), 3-Formylbenzonitrile (99%), 4-Formylbenzonitrile (99%), 3-Bromobenzaldehyde (99%), trans-4-Bromocinnamaldehyde (99%), 3-(Trifluoromethyl)benzaldehyde (97%), 4-(Trifluoromethyl)benzaldehyde (98%), trans-3-Methoxycinnamaldehyde (97%), 2,3,6-Trifluorobenzaldehyde (98%), 3,4-Difluorobenzaldehyde (97%), 2,5-Difluorobenzaldehyde (98%), malononitrile (>98%), and (1,3-Dioxolan-2-ylmethyl)triphenylphosphonium bromide (98%) were purchased from Santa Cruz Biotechnology USA. Potassium carbonate anhydrous (99%) was used. All the organic solvents used were of reagent grade. Spectroscopic grade solvents were used as received. Thin layer chromatography (TLC) was performed on 5x2.5 cm pre-coated silica gel GF254 on an aluminum sheet. Spots on TLC were visualized using UV light (254 nm) or developed chemically using KMnO₄ aqueous solution. Silica gel for column chromatography (spherical 100 microns) was purchased from TCI America.

NMR spectroscopy: ¹H NMR spectra were recorded on JEOL (400 MHz) at 298 K. Abbreviations were used to describe peak splitting patterns: s = singlet, d = doublet, dd = doublet of a doublet, ddd = doublet of a doublet of a doublet, dt = doublet of triplets, tt = triplet of triplets, m = multiplet. ¹³C NMR spectra were recorded on JEOL (101 MHz) spectrometer with complete proton decoupling at 298 K. Proton chemical shifts were reported in ppm (δ) (DMSO-d₆, δ 2.50 ppm, and CDCl₃, δ 7.24 ppm) and J values are reported in hertz (Hz). Carbon chemical shifts were reported in ppm (δ) (DMSO-d₆, δ 39.52 ppm, and CDCl₃, δ 77.23 ppm). In some cases, a 10% (V/V) mixture of DMSO-d₆ in CCl₄ was used instead of pure DMSO-d₆ to increase the solubility of the compound and prevent the solution from freezing.

Melting Point: Differential scanning calorimetry was used to determine all melting points. Samples were prepared in 30 μL aluminum concave pans and measurements were performed on a Netzsch DSC 214 at a heating rate of 10 °C/min.

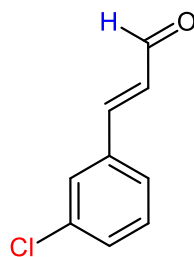
The derivatives were synthesized following the general reaction scheme-1 outlined below:



Scheme-1: The following synthesis scheme was used for the synthesis of the studied derivatives.

S2.1: 3CICM

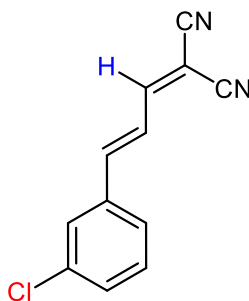
A. Synthesis of *trans*-3-Chlorocinnamaldehyde:



3-Chlorobenzaldehyde (0.56 g, 4 mmol, 1 eq.), (1,3-Dioxolan-2-ylmethyl)triphenylphosphonium bromide (2.0g, 4.8 mmol, 1.2 eq.), K_2CO_3 (5.2g, 38 mmol, 19 eq), and tetra-*n*-butylammonium acetate (50 mg) were dissolved in a mixture of $CHCl_3$ (25 mL), water (25 mL). The reaction mixture was stirred vigorously at 80 °C under an atmosphere of Argon gas for 12-24 hours. The reaction progress was monitored by TLC using Ethyl acetate/Hexane (1:3 ratio). When the aldehyde is consumed the Chloroform layer was separated and the acetal was decomposed to generate the aldehyde by adding HCl (2 mL, 12M) and stirring at room temperature for 1 hour. The reaction progress was monitored by TLC using Ethyl acetate /Hexane (1:3 ratio). The organic phase was washed with water followed by brine then dried using anhydrous $MgSO_4$. Decant then remove the organic phase under reduced pressure. Obtained a solid mixture of the *trans*-3-chlorocinnamaldehyde and triphenylphosphine oxide. The aldehyde was separated from the triphenylphosphine oxide by passing through 20 grams of activated silica gel using 30% Ethyl acetate in hexane as the mobile phase. The organic solvent was removed under reduced pressure to afford *trans*-3-chlorocinnamaldehyde as a pale-yellow oil (0.62 g, 92% yield). The 1H NMR of the product matched the 1H NMR reported in the literature. The product was taken to the next step without further purification. Traces of triphenylphosphine oxide were detected in the 1H NMR of the final product, but that had little effect on the next step. The 1H NMR of the final product was similar to the NMR reported in [10.1002/anie.201912043].

1H NMR (400 MHz, $DMSO-d_6$) δ 9.67 (d, $J = 7.5$ Hz, 1H), 7.69 – 7.58 (m, 2H), 7.58 – 7.47 (s, 1H), 7.43 – 7.33 (m, 2H), 6.75 (dd, $J = 16.0, 7.5$ Hz, 1H).

B. Synthesis of (*E*)-3-Chloro-Cinnamalmalononitrile (3CICM):



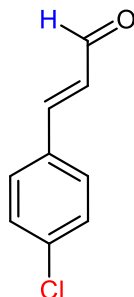
Trans-3-chlorocinnamaldehyde (0.58 g, 3.4 mmol, 1 eq) was dissolved in Ethanol (20 mL). Water was slowly added to the mixture until the solution became turbid (~40 mL). Excess Malononitrile (0.82 g, 12.4 mmol, 3.6 eq) was added to the mixture and stirred at room temperature for 24 hours under a blanket of Argon gas. The product separates as yellow amorphous powder that was suction filtered and recrystallized from ethanol/ water. Obtained yellow crystal powder (0.52 g, 70% yield). MP: 149-151 °C.

^1H NMR (400 MHz, DMSO- d_6) δ 8.20 – 8.12 (d, 1H), 7.70 (s, 1H), 7.64 – 7.57 (m, 1H), 7.48 (d, $J = 15.3$ Hz, 1H), 7.39 (dd, $J = 3.9, 1.3$ Hz, 2H), 7.27 (dd, $J = 15.3, 11.3$ Hz, 1H).

^{13}C NMR (101 MHz, DMSO- d_6) δ 160.79, 148.60, 136.27, 134.72, 130.82, 130.19, 128.72, 126.78, 123.77, 113.16, 111.20, 83.12.

S2.2: 4C1CM

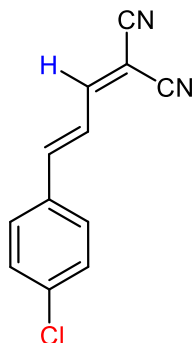
A. Synthesis of *trans*-4-Chlorocinnamaldehyde:



Synthesis of this compound was done following a procedure similar to the one reported for the synthesis of *trans*-3-Chlorocinnamaldehyde. Starting with 4-chlorobenzaldehyde (0.28g, 2 mmol, 1eq.), obtained a yellow oil (0.31 g, 92% yield) that was carried to the next step without further purification. The ¹H NMR of the product matched the ¹H NMR reported in the literature [[10.1039/c8cc03722a](https://doi.org/10.1039/c8cc03722a)].

¹H NMR (400 MHz, DMSO-D₆) δ 9.65 (d, J = 7.6 Hz, 1H), 7.66 – 7.57 (m, 2H), 7.52 (d, J = 16.0 Hz, 1H), 7.46 – 7.36 (m, 2H), 6.73 (dd, J = 16.0, 7.6 Hz, 1H).

B. Synthesis of (*E*)-4-Chloro-Cinnamalmalononitrile (**4C1CM**):



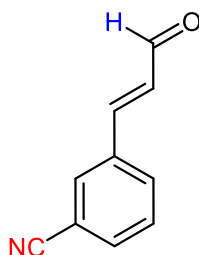
Synthesis of this compound was done following a procedure similar to the one reported for the synthesis of 3C1CM. Starting with *trans*-4-Chlorocinnamaldehyde (0.52g, 3.3 mmol, 1eq.) and excess malononitrile we obtained (0.50 g, 68% yield) of yellowish crystals.

¹H NMR (400 MHz, DMSO-D₆) δ 8.15 (d, J = 11.4 Hz, 1H), 7.68 (d, J = 8.6 Hz, 2H), 7.50 (d, J = 15.3 Hz, 1H), 7.40 (d, J = 8.5 Hz, 2H), 7.23 (dd, J = 15.2, 11.4 Hz, 1H).

¹³C NMR (101 MHz, DMSO-D₆) δ 160.88, 148.92, 137.00, 132.93, 130.22, 129.13, 122.96, 113.24, 111.34, 82.44.

S2.3: 3CNCM

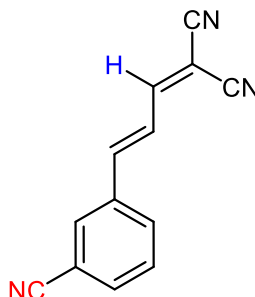
A. Synthesis of *trans*-3-Cyanocinnamaldehyde:



Synthesis of this compound was done following a procedure similar to the one reported for the synthesis of *trans*-3-Chlorocinnamaldehyde. Starting with 3-cyanobenzaldehyde (0.37g, 2.8 mmol, 1eq.), a pale yellow solid product (0.33 g, 75% yield) was carried to the next step without further purification. The ^1H NMR of the product matched the ^1H NMR reported in the literature [10.1248/cpb.55.1494]

^1H NMR (400 MHz, DMSO- D_6) δ 9.70 (d, J = 7.6 Hz, 1H), 8.15 (d, J = 1.6 Hz, 1H), 8.05 – 7.93 (m, 1H), 7.78 (dt, J = 7.7, 1.3 Hz, 1H), 7.72 – 7.55 (m, 2H), 6.91 (dd, J = 16.0, 7.6 Hz, 1H).

B. Synthesis of (*E*)-3-Cyano-Cinnamalmalononitrile (3CNCM):



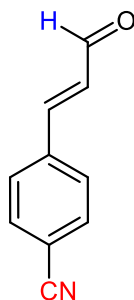
Synthesis of this compound was done following a procedure similar to the one reported for the synthesis of 3CICM. Starting with *trans*-3-Cyanocinnamaldehyde (0.3g, 1.9 mmol, 1eq.) and excess malononitrile, obtained (0.28 g, 68% yield) of a pale yellow solid. MP: 184-185 °C.

^1H NMR (400 MHz, DMSO- D_6) δ 8.29 (s, 1H), 8.23 (d, J = 11.2 Hz, 1H), 8.00 (d, J = 7.9 Hz, 1H), 7.79 (dt, J = 7.7, 1.2 Hz, 1H), 7.66 – 7.50 (m, 2H), 7.43 (dd, J = 15.3, 11.2 Hz, 1H).

^{13}C NMR (101 MHz, DMSO- D_6) δ 161.21, 148.09, 135.54, 133.87, 133.00, 132.45, 129.95, 124.73, 117.61, 113.36, 113.06, 111.38, 83.21.

S2.4: 4CNCM

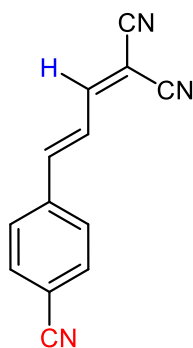
A. Synthesis of *trans*-4-Cyanocinnamaldehyde:



Synthesis of this compound was done following a procedure similar to the one reported for the synthesis of trans-3-Chlorocinnamaldehyde. Starting with 4-cyanobenzaldehyde (0.52g, 4 mmol, 1eq.), a pale yellow solid (0.4 g, 64% yield) was carried to the next step without further purification. The ^1H NMR of the product matched the ^1H NMR reported in the literature [[10.1039/b812306c](https://doi.org/10.1039/b812306c)]

^1H NMR (400 MHz, $\text{DMSO-}D_6$) δ 9.71 (d, $J = 7.5$ Hz, 1H), 7.83 (d, $J = 8.3$ Hz, 2H), 7.76 (d, $J = 8.4$ Hz, 2H), 7.62 (d, $J = 16.1$ Hz, 1H), 6.87 (dd, $J = 16.0, 7.5$ Hz, 1H).

B. Synthesis of (*E*)-4-Cyano-Cinnamalmalononitrile (**4CNCM**):



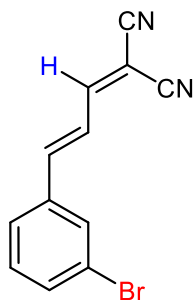
Synthesis of this compound was done following a procedure similar to the one reported for the synthesis of 3ClCM. Starting with trans-4-Cyanocinnamaldehyde (0.38g, 2.4 mmol, 1eq.) and excess malononitrile, we obtained (0.37 g, 74% yield) of pale yellow crystals. MP: 197-200 °C.

^1H NMR (400 MHz, $\text{DMSO-}D_6$) δ 8.22 (d, $J = 11.2$ Hz, 1H), 7.88 (d, $J = 8.3$ Hz, 2H), 7.76 (d, $J = 8.4$ Hz, 2H), 7.57 (d, $J = 15.3$ Hz, 1H), 7.36 (dd, $J = 15.3, 11.3$ Hz, 1H).

^{13}C NMR (151 MHz, DMSO) δ 161.82, 148.78, 138.89, 133.41, 130.12, 126.10, 118.93, 113.56, 112.37, 83.85.

S2.5: 3BrCM

B. Synthesis of (*E*)-3-Bromo-Cinnamalmalononitrile (**3BrCM**):



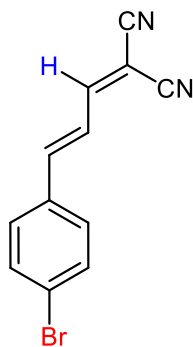
Synthesis of this compound was done following a procedure similar to the one reported for the synthesis of **3CICM**. Starting with commercially available *trans*-3-Bromocinnamaldehyde (1g, 4.7 mmol, 1eq.) and excess malononitrile, we obtained (1.1 g, 89% yield) of yellow crystals. MP: 156-160 °C.

¹H NMR (400 MHz, DMSO-D₆) δ 8.21 (dd, J = 11.3, 0.5 Hz, 1H), 7.91 (t, J = 1.7 Hz, 1H), 7.69 (d, J = 7.8 Hz, 1H), 7.58 (ddd, J = 8.0, 1.9, 0.9 Hz, 1H), 7.52 (d, J = 15.2 Hz, 1H), 7.37 (t, J = 7.9 Hz, 1H), 7.29 (dd, J = 15.2, 11.3 Hz, 1H).

¹³C NMR (101 MHz, DMSO-D₆) δ 161.31, 148.95, 136.53, 133.83, 131.45, 130.74, 127.61, 123.82, 122.67, 113.45, 111.50, 82.48.

S2.6: 4BrCM

A. Synthesis of (*E*)-4-Bromo-Cinnamalmalononitrile (**4BrCM**)



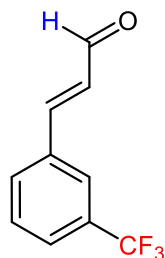
Synthesis of this compound was done following a procedure similar to the one reported for the synthesis of 3CICM. Starting with commercially available *trans*-3-Bromocinnamaldehyde (0.21g, 1 mmol, 1eq.) and excess malononitrile, we obtained (0.14 g, 54% yield) of yellow needle-like crystals. MP: 196-197 °C.

^1H NMR (400 MHz, $\text{DMSO-}D_6$) δ 8.14 (d, $J = 11.3$ Hz, 1H), 7.61 (d, $J = 8.6$ Hz, 2H), 7.55 (d, $J = 8.6$ Hz, 2H), 7.48 (d, $J = 15.2$ Hz, 1H), 7.24 (dd, $J = 15.2, 11.4$ Hz, 1H).

^{13}C NMR (101 MHz, $\text{DMSO-}D_6$) δ 160.89, 149.01, 133.32, 132.07, 130.38, 125.57, 123.04, 113.25, 111.34, 82.51.

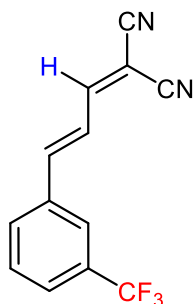
S2.7: 3CF3CM

A. Synthesis of *trans*-3-(trifluoromethyl)Cinnamaldehyde:



Synthesis of this compound was done following a procedure similar to the one reported for the synthesis of trans-3-Chlorocinnamaldehyde. Starting with 3-(trifluoromethyl)Benzaldehyde (0.7g, 4 mmol, 1eq.), a pale yellow oil (0.6 g, 75% yield) was obtained, which was used in the next step without further purification. The ^1H NMR of the product matched the ^1H NMR reported in the literature [10.1021/ol051234w]

B. Synthesis of (*E*)-3-trifluoromethyl-Cinnamalmalononitrile (**3CF3CM**)



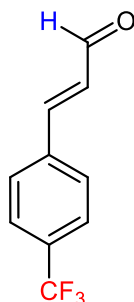
Synthesis of this compound was done following a procedure similar to the one reported for the synthesis of 3C1CM. Starting with crude trans-3-(trifluoromethyl)cinnamaldehyde (0.6g, 3 mmol, 1eq.) and excess malononitrile, we obtained yellow crystals of **3CF3CM** (0.44 g, 61% yield) after recrystallization from the appropriate solvent. MP: 114-116 °C.

^1H NMR (400 MHz, $\text{DMSO-}D_6$) δ 8.19 (d, $J = 11.3$ Hz, 1H), 7.97 (d, $J = 5.9$ Hz, 2H), 7.68 (d, $J = 7.7$ Hz, 1H), 7.59 (dd, $J = 15.5, 6.9$ Hz, 2H), 7.37 (dd, $J = 15.3, 11.3$ Hz, 1H).

^{13}C NMR (101 MHz, $\text{DMSO-}D_6$) δ 161.32, 148.84, 135.25, 132.04, 130.82, 130.50, 129.83, 127.31, 125.76, 124.99, 124.25, 122.29, 113.42, 111.48, 82.85.

S2.8: 4CF3CM

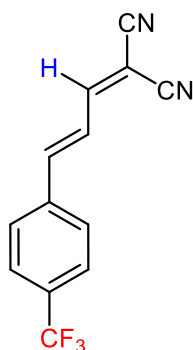
A. Synthesis of trans-4-(trifluoromethyl)Cinnamaldehyde:



Synthesis of this compound was done following a procedure similar to the one reported for the synthesis of trans-3-Chlorocinnamaldehyde. Starting with 4-(trifluoromethyl)benzaldehyde (0.35g, 2 mmol, 1eq.), a pale yellow solid (0.32 g, 80% yield) was obtained, which was used in the next step without further purification. The ^1H NMR of the product matched the ^1H NMR reported in the literature [10.1002/anie.201912043]

^1H NMR (400 MHz, $\text{DMSO-}D_6$) δ 9.71 (d, $J = 7.5$ Hz, 1H), 7.82 (d, $J = 8.2$ Hz, 2H), 7.69 (d, $J = 8.3$ Hz, 2H), 7.62 (d, $J = 16.0$ Hz, 1H), 6.86 (dd, $J = 16.0, 7.5$ Hz, 1H).

B. Synthesis of (*E*)-4-trifluoromethyl-Cinnamalmalononitrile (**4CF3CM**)



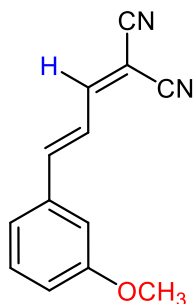
Synthesis of this compound was done following a procedure similar to the one reported for the synthesis of 3ClCM. Starting with crude trans-4-(trifluoromethyl)cinnamaldehyde (0.44g, 2.2 mmol, 1eq.) and excess malononitrile, the product **4CF3CM** was obtained (0.44 g, 81% yield) as yellow powder crystals after recrystallization from the appropriate solvent. MP: 143-147 °C.

^1H NMR (400 MHz, $\text{DMSO-}D_6$) δ 8.21 (d, $J = 11.3$ Hz, 1H), 7.87 (d, $J = 8.2$ Hz, 2H), 7.68 (d, $J = 8.3$ Hz, 2H), 7.58 (d, $J = 15.3$ Hz, 1H), 7.34 (dd, $J = 15.3, 11.3$ Hz, 1H).

^{13}C NMR (101 MHz, $\text{DMSO-}D_6$) δ 160.67, 148.25, 137.78, 132.12, 131.80, 129.17, 125.74, 125.67, 124.88, 124.70, 122.16, 113.06, 111.16, 83.82.

S2.9: 3MeOCM

A. Synthesis of (*E*)-3-methoxy-Cinnamalmalononitrile (**3MeOCM**)



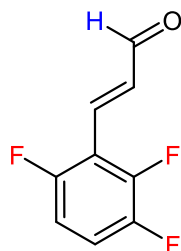
Synthesis of this compound was done following a procedure similar to the one reported for the synthesis of 3CICM. Starting with commercially available *trans*-3-methoxycinnamaldehyde (1g, 6.1 mmol, 1eq.), obtained yellow plate crystals (1.1 g, 80% yield). MP: 127-135 °C.

^1H NMR (400 MHz, $\text{DMSO-}D_6$) δ 8.19 (dd, $J = 11.4, 0.6$ Hz, 1H), 7.53 (d, $J = 15.2$ Hz, 1H), 7.33 (t, $J = 7.9$ Hz, 1H), 7.27 – 7.16 (m, 3H), 6.99 (ddd, $J = 8.2, 2.5, 0.9$ Hz, 1H), 3.83 (s, 3H).

^{13}C NMR (101 MHz, $\text{DMSO-}D_6$) δ 162.12, 160.23, 151.52, 135.97, 130.38, 123.12, 121.91, 118.09, 114.15, 114.09, 112.16, 81.79, 55.62.

S2.10: 2,3,6FCM

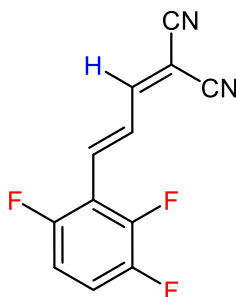
A. Synthesis of *trans*-2,3,6-trifluoro-cinnamaldehyde



Synthesis of this compound was done following a procedure similar to the one reported for the synthesis of trans-3-Chlorocinnamaldehyde. Starting with 2,3,6-trifluorobenzaldehyde (0.64g, 4 mmol, 1eq.), obtained pale yellow crystals (0.6 g, 81% yield). The ^1H NMR of the product matched the ^1H NMR reported in the literature [[10.3184/030823407x225464](https://doi.org/10.3184/030823407x225464)]

^1H NMR (400 MHz, $\text{DMSO-}D_6$) δ 9.70 (d, $J = 7.4$ Hz, 1H), 7.56 (d, $J = 16.5$ Hz, 1H), 7.37 (qd, $J = 9.3$, 5.0 Hz, 1H), 7.06 (tdd, $J = 9.5$, 3.7, 2.2 Hz, 1H), 6.88 (dd, $J = 16.5$, 7.4 Hz, 1H).

B. Synthesis of (*E*)-2,3,6-trifluoro-Cinnamalmalononitrile (**236FCM**):



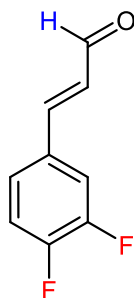
Synthesis of this compound was done following a procedure similar to the one reported for the synthesis of 3CICM. Starting with trans-2,3,6-trifluoro-cinnamaldehyde (0.60 g, 3.2 mmol, 1eq.), obtained yellow crystals (0.31 g, 41% yield). MP: 107-109 °C.

^1H NMR (400 MHz, $\text{DMSO-}D_6$) δ 8.29 (d, $J = 10.9$ Hz, 1H), 7.57 (d, $J = 15.7$ Hz, 1H), 7.47 (dd, $J = 15.7$, 10.9 Hz, 1H), 7.37 (qd, $J = 9.2$, 5.0 Hz, 1H), 7.12 – 6.99 (m, 1H).

^{13}C NMR (101 MHz, $\text{DMSO-}D_6$) δ 161.01, 134.76, 129.23, 129.14, 129.04, 119.41, 119.22, 114.16, 112.78, 111.79, 110.81, 85.13.

S2.11: 3,4FCM

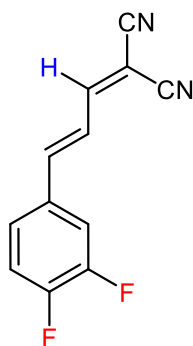
A. Synthesis of trans-3,4-difluoro-cinnamaldehyde:



Synthesis of this compound was done following a procedure similar to the one reported for the synthesis of trans-3-Chlorocinnamaldehyde. Starting with 3,4-difluorobenzaldehyde (0.57g, 4 mmol, 1eq.), obtained pale yellow crystals (0.58 g, 86% yield).

^1H NMR (400 MHz, $\text{DMSO-}D_6$) δ 9.65 (d, $J = 7.5$ Hz, 1H), 7.70 – 7.58 (m, 1H), 7.51 (d, $J = 16.0$ Hz, 1H), 7.46 (dq, $J = 6.3, 2.1$ Hz, 1H), 7.28 (dt, $J = 9.9, 8.3$ Hz, 1H), 6.72 (dd, $J = 16.0, 7.6$ Hz, 1H).

B. Synthesis of (*E*)-3,4-difluoro-Cinnamalmalononitrile (**3,4FCM**):



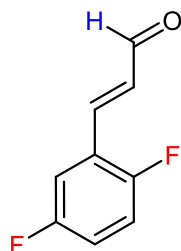
Synthesis of this compound was done following a procedure similar to the one reported for the synthesis of 3ClCM. Starting with trans-3,4-difluoro-cinnamaldehyde (0.48 g, 2.9 mmol, 1eq.), obtained yellow needles (0.25 g, 39% yield). MP: 142-144 °C.

^1H NMR (400 MHz, $\text{DMSO-}D_6$) δ 8.13 (d, $J = 11.4$ Hz, 1H), 7.78 – 7.65 (m, 1H), 7.55 – 7.41 (m, 2H), 7.35 – 7.18 (m, 2H).

^{13}C NMR (151 MHz, DMSO) δ 162.26, 149.04, 132.53, 127.79, 124.32, 118.86, 118.74, 118.03, 117.91, 114.58, 112.52, 82.39.

S2.12 2,5FCM

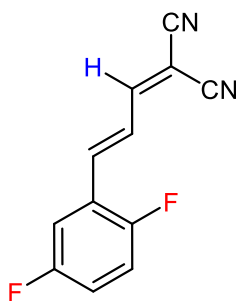
A. Synthesis of trans-2,5-difluoro-cinnamaldehyde



Synthesis of this compound was done following a procedure similar to the one reported for the synthesis of trans-3-Chlorocinnamaldehyde. Starting with 2,5-difluorobenzaldehyde (0.57g, 4 mmol, 1eq.), obtained pale yellow crystals (0.48 g, 71% yield).

^1H NMR (400 MHz, DMSO- D_6) δ 9.69 (d, J = 7.5 Hz, 1H), 7.63 (d, J = 16.2 Hz, 1H), 7.53 (td, J = 6.7, 3.2 Hz, 1H), 7.24 – 7.10 (m, 2H), 6.83 (dd, J = 16.2, 7.5 Hz, 1H).

B. Synthesis of (*E*)-2,5-difluoro-Cinnamalmalononitrile (**2,5FCM**):

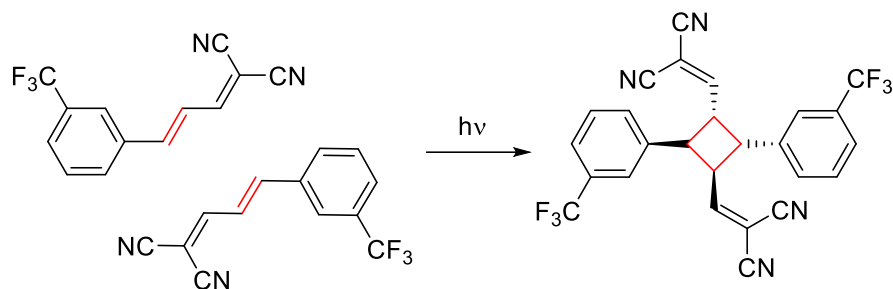


Synthesis of this compound was done following a procedure similar to the one reported for the synthesis of 3CICM. Starting with trans-3,4-difluoro-cinnamaldehyde (0.40 g, 2.3 mmol, 1eq.), obtained yellow needles (0.35 g, 76% yield). MP: 152-156 °C.

^1H NMR (400 MHz, DMSO- D_6) δ 8.20 (d, J = 11.3 Hz, 1H), 7.65 (dd, J = 8.6, 6.0 Hz, 1H), 7.58 (d, J = 15.4 Hz, 1H), 7.37 (dd, J = 15.4, 11.3 Hz, 1H), 7.23 – 7.12 (m, 2H).

^{13}C NMR (101 MHz, DMSO- D_6) δ 160.75, 159.72, 158.54, 157.29, 156.04, 140.82, 125.92, 125.86, 123.89, 123.81, 123.75, 123.67, 119.40, 119.31, 119.15, 119.06, 117.47, 117.39, 117.22, 117.14, 115.33, 115.11, 113.03, 111.05, 84.04.

S2.13: Solid-state photodimerization of **3CF3CM**



A sample of 3CF3CM was purified by recrystallization from acetonitrile/water and then dried in a vacuum oven at room temperature. Next, a portion of the crystals (0.1 g, 0.55 mmol) was placed in a Schlenk flask and suspended in 30 mL of deionized water. The mixture was sonicated in a bath sonicator (Branson) to break up the crystals, followed by purging with argon gas for 10 minutes. To further aid in breaking up the 3CF3CM crystals and dispersing them throughout the aqueous phase, 0.5 mL of methanol was added to the suspension. The Schlenk flask was sealed under argon gas and then exposed to 450 nm light from a commercial blue LED strip for photolysis. The photolysis process was considered complete when the suspended crystals changed color from yellow to white, which could take up to two days depending on the intensity of the LED used. The resulting photoproduct was then suction filtered and air-dried, yielding a quantitative amount of the photodimer. ¹H NMR of the photodimer showed chemical shifts consistent with the formation of a cyclobutene derivative.

¹H NMR (400 MHz, DMSO-*D*₆) δ 7.87 (d, *J* = 10.1 Hz, 2H), 7.79 (m, 4H), 7.70 – 7.50 (m, 4H), 4.61 (td, *J* = 10.2, 6.8 Hz, 2H), 4.50 (dd, *J* = 9.0, 6.5 Hz, 2H).

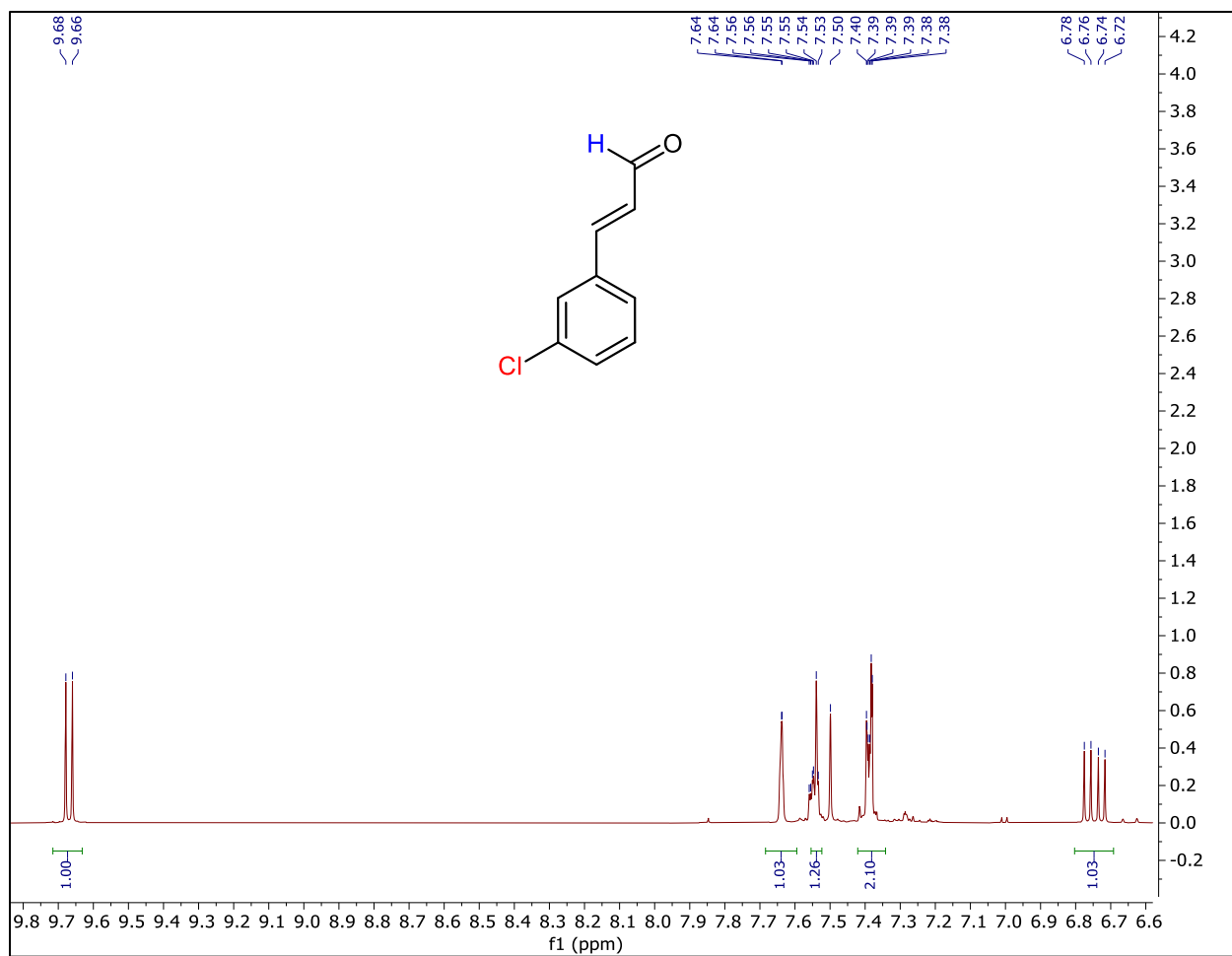


Figure S13: The ¹H NMR spectrum of trans-3-Chlorocinnamaldehyde in DMSO-D₆.

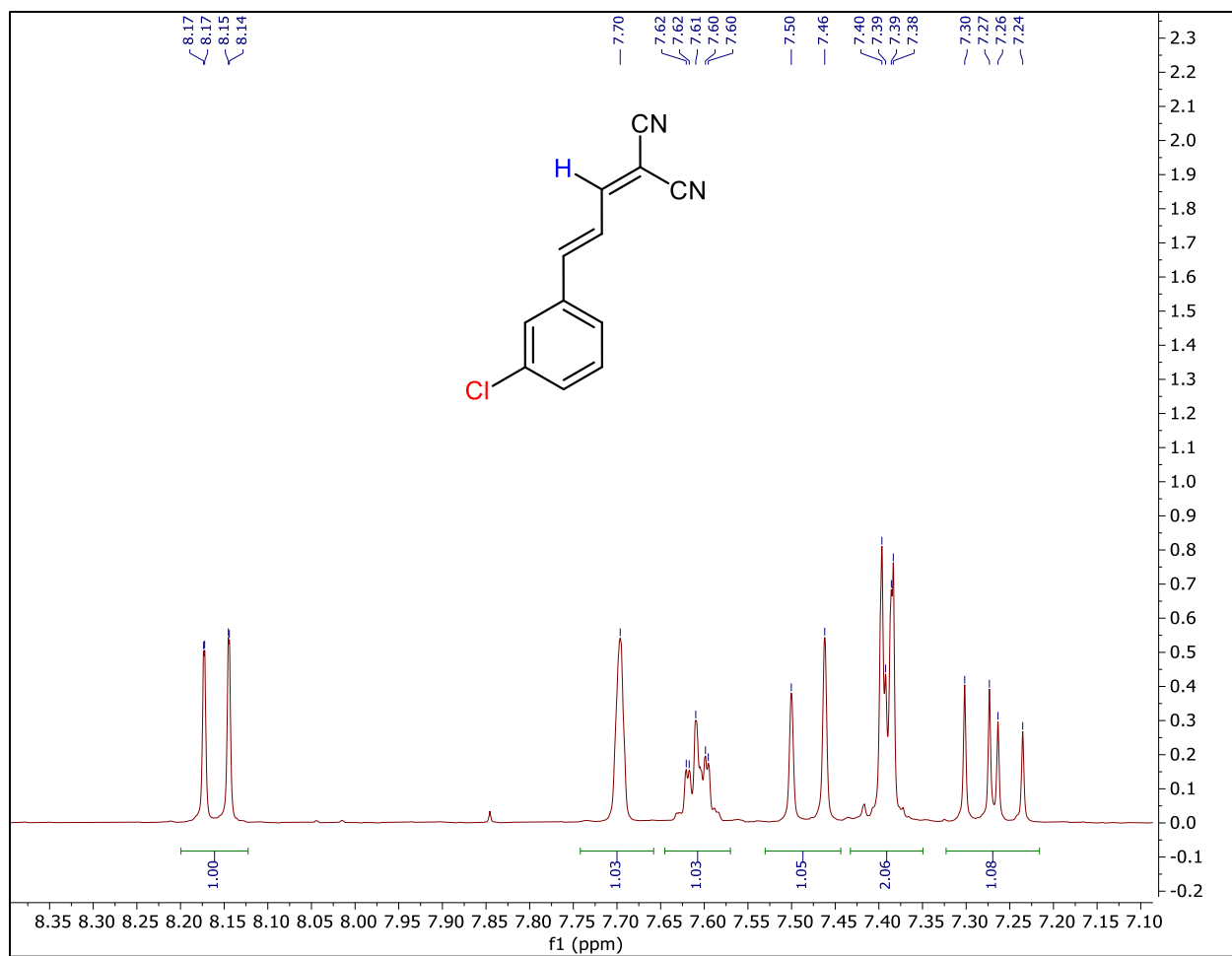


Figure S14-A: The ¹H NMR spectra of 3CICM in DMSO-D₆.

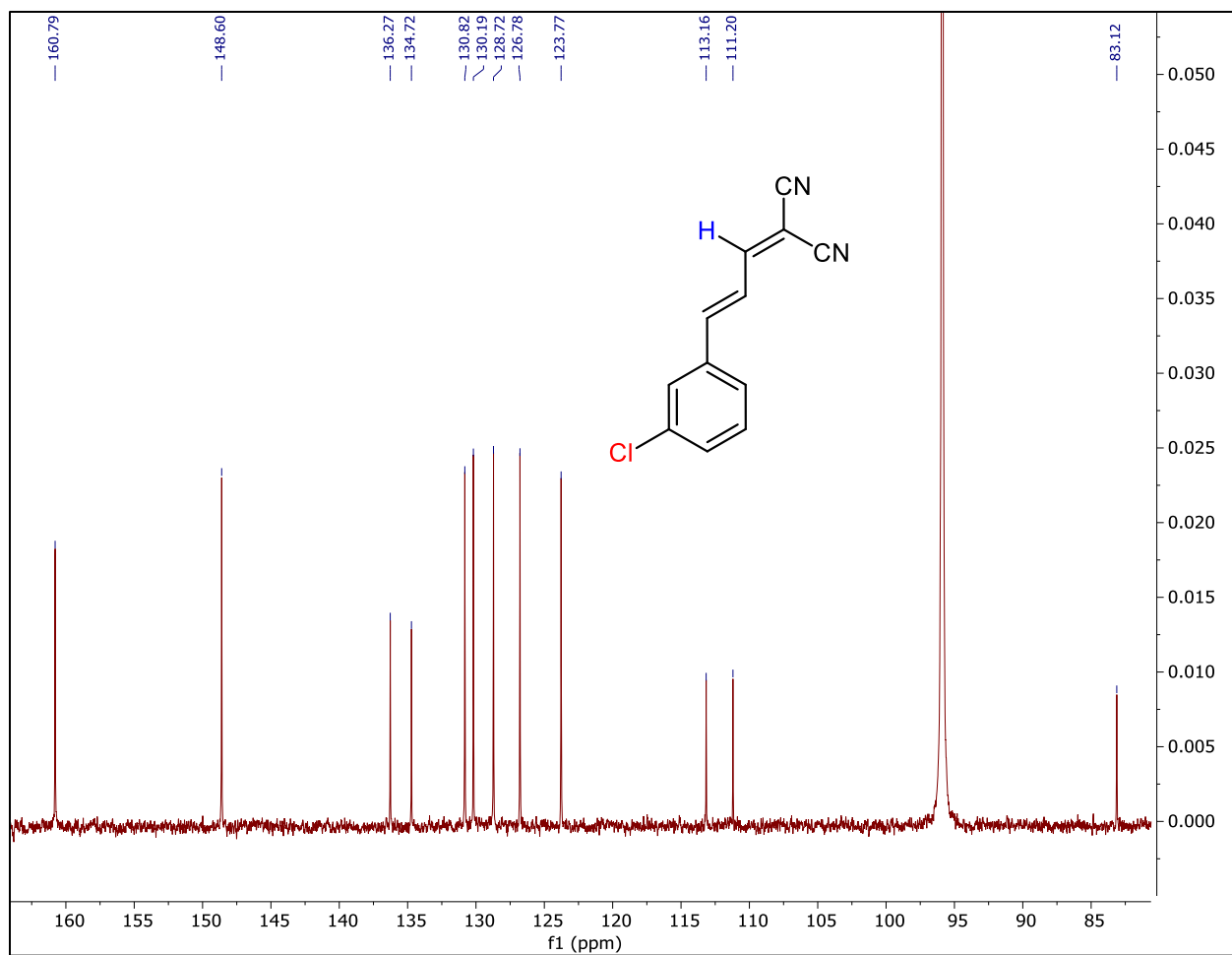


Figure S14-B: The ^{13}C NMR spectra of **3CICM** in DMSO-D_6 .

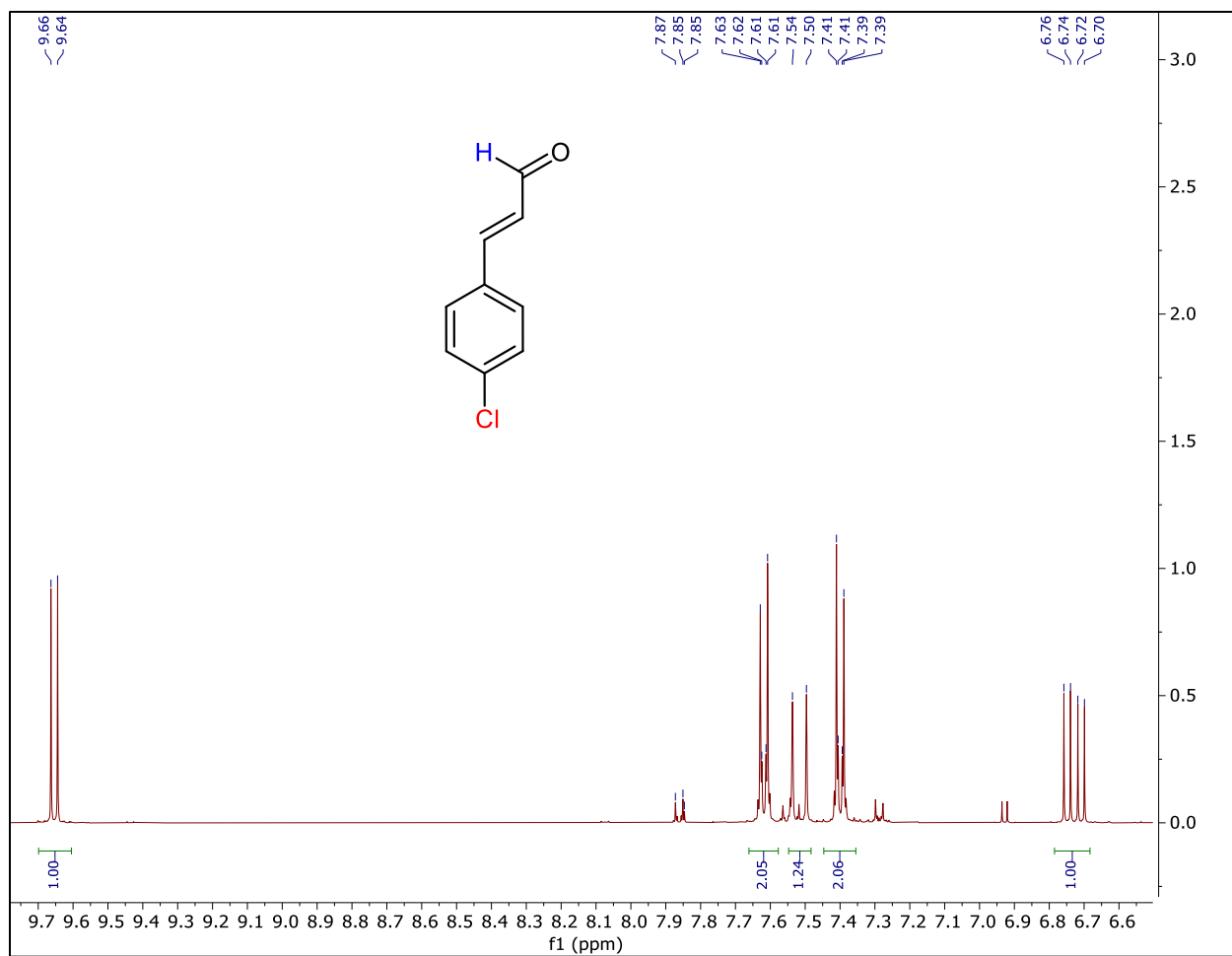


Figure S15: The ¹H NMR spectrum of trans-4-Chlorocinnamaldehyde in DMSO-D₆.

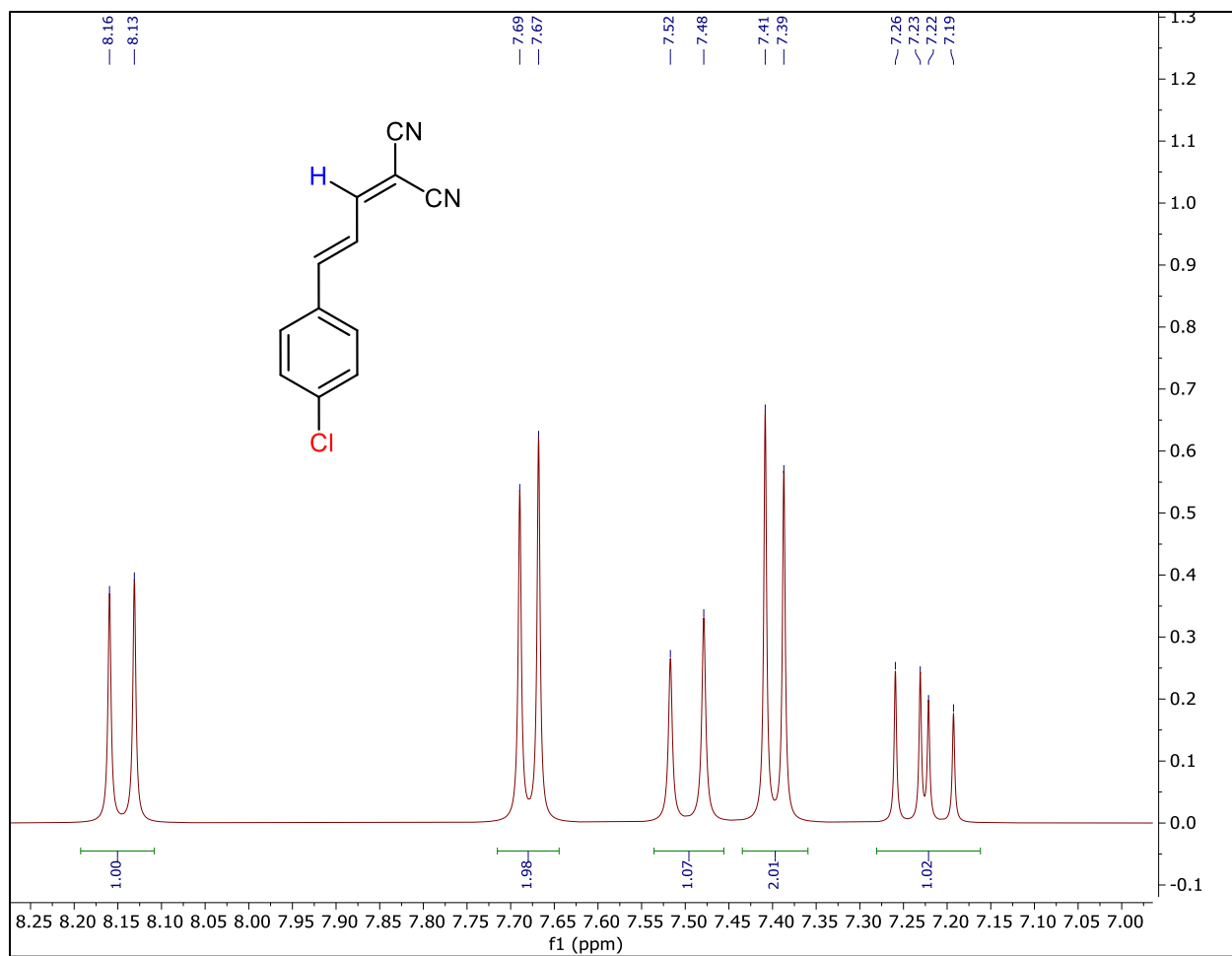


Figure S16-A: The ¹H NMR spectra of 4CICM in DMSO-D₆.

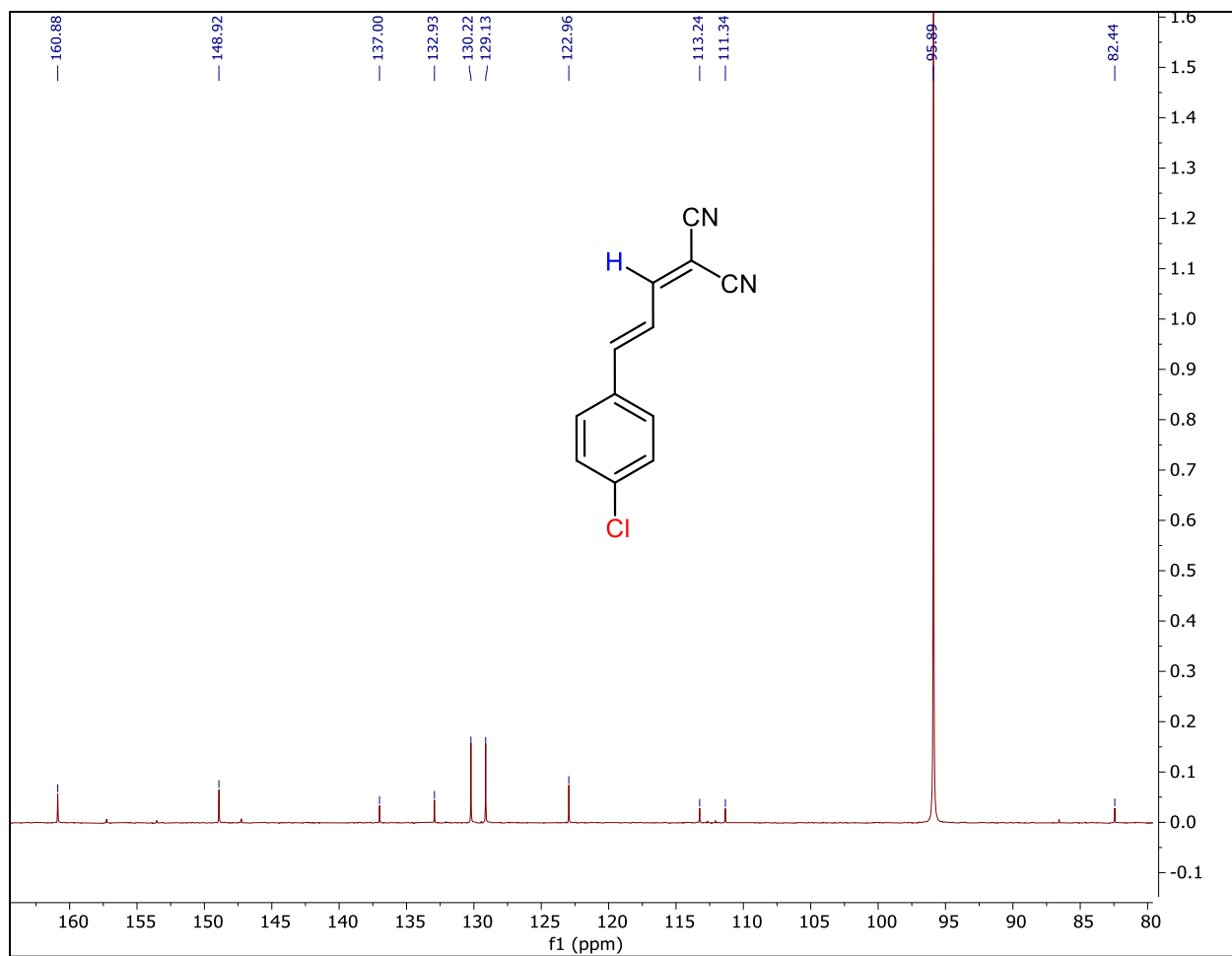


Figure S16-A: The ^{13}C NMR spectra of 4ClCM in $\text{DMSO-}D_6$.

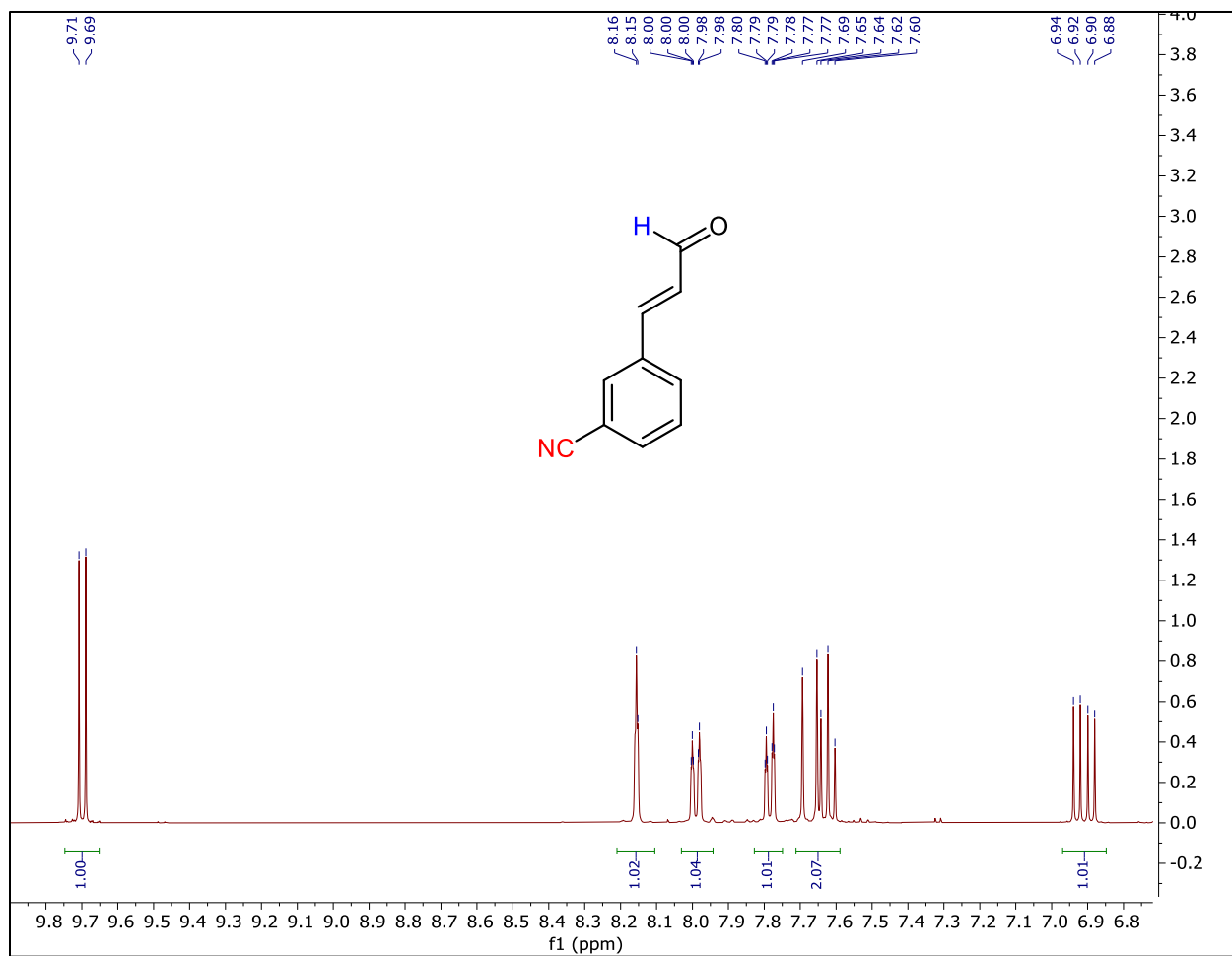


Figure S17: The ¹H NMR spectra of trans-4-Cyanocinnamaldehyde in DMSO-D₆.

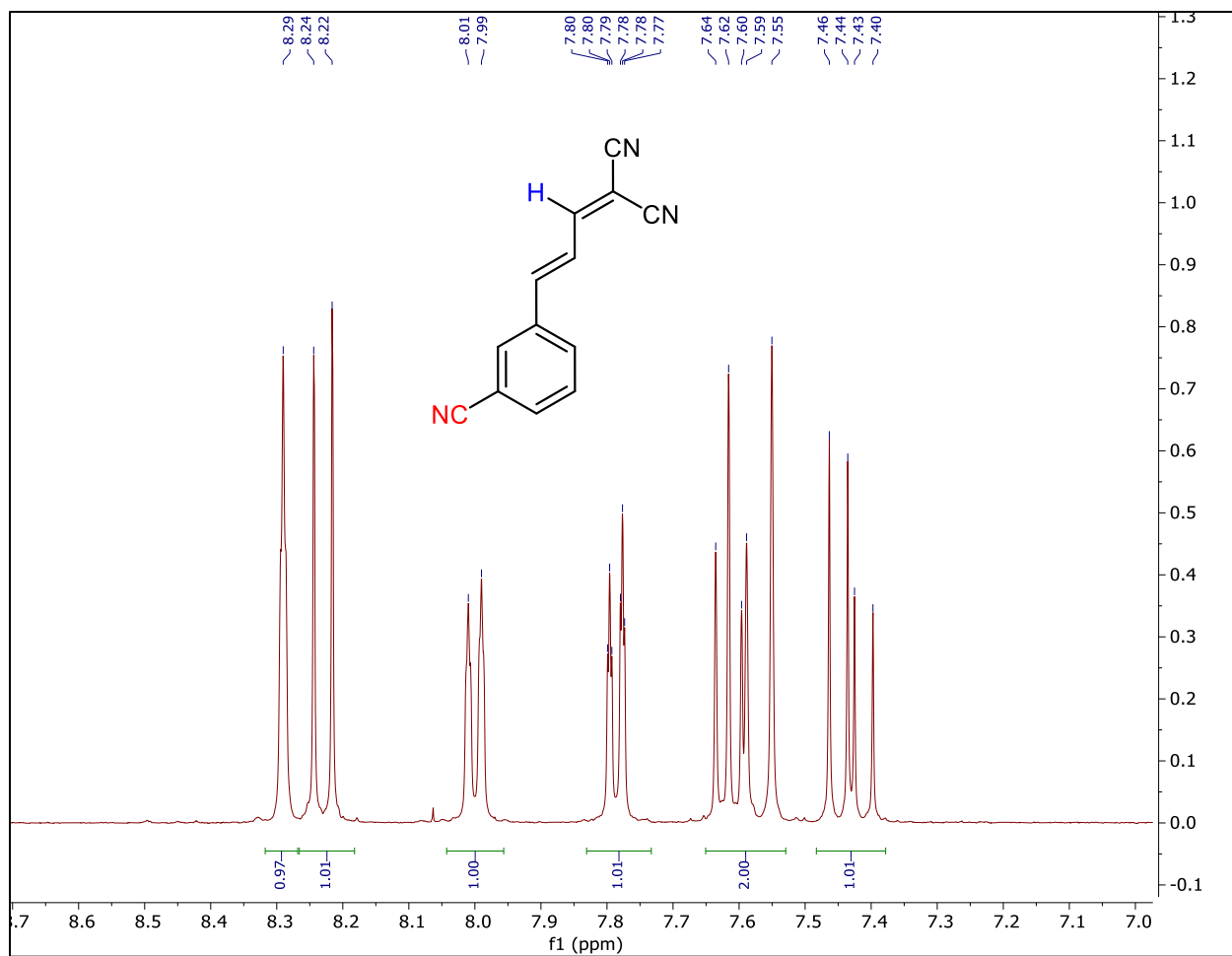


Figure S18-A: The ^1H NMR spectra of **3CNM** in DMSO-D_6 .

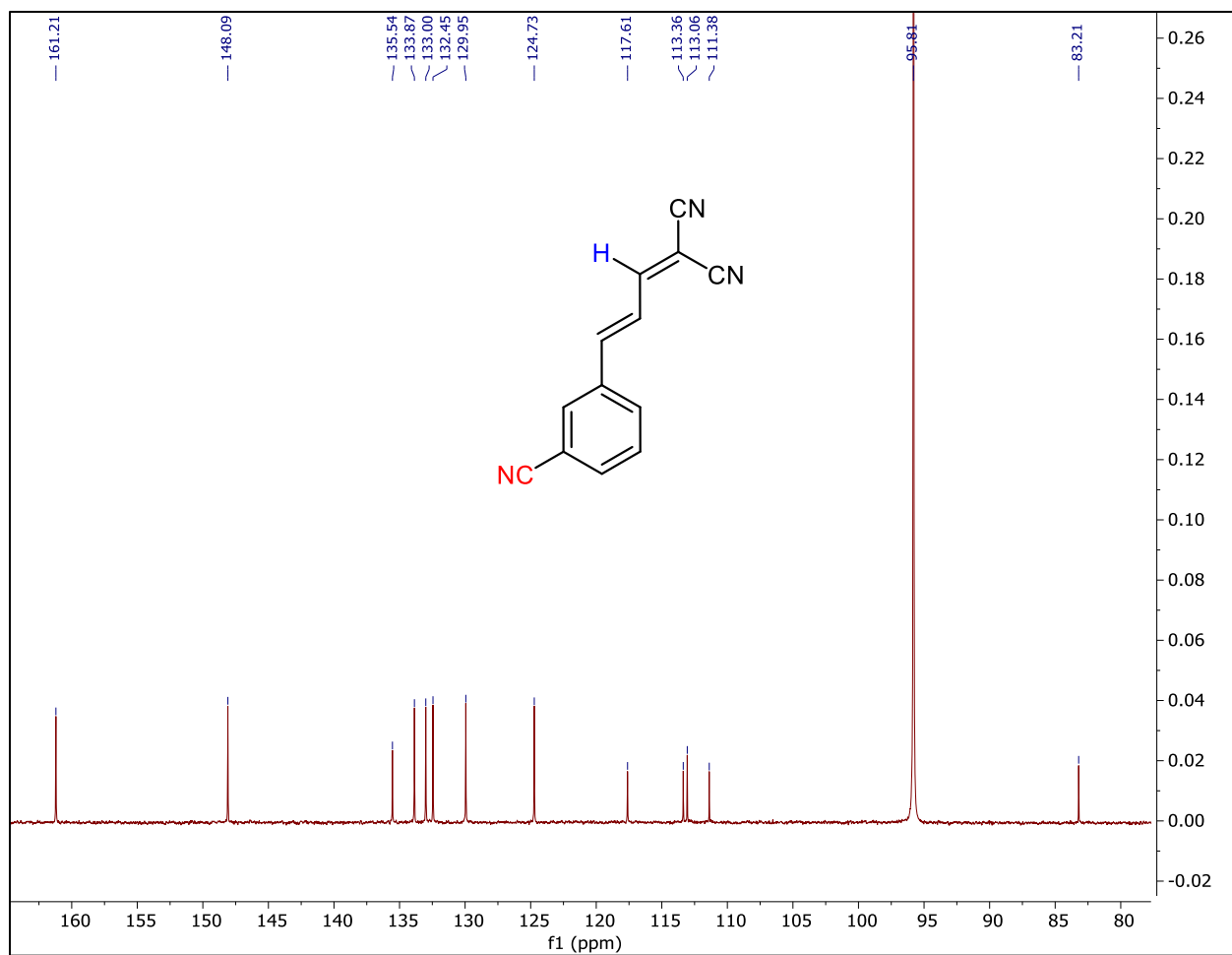


Figure S18-B: The ^{13}C NMR spectra of 3CNCM in DMSO- D_6 .

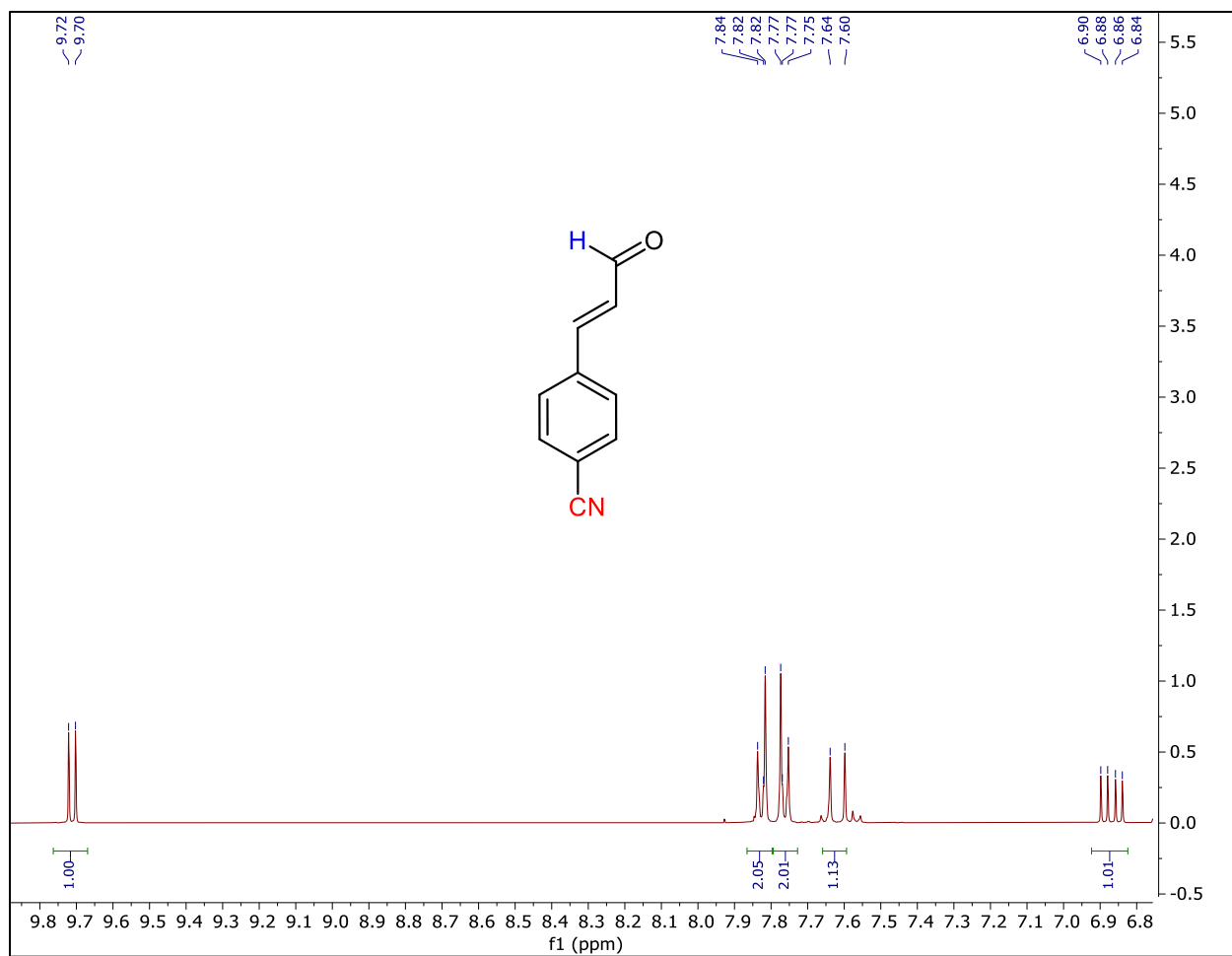


Figure S19: The ¹H NMR spectra of trans-4-Cyanocinnamaldehyde in DMSO-D₆.

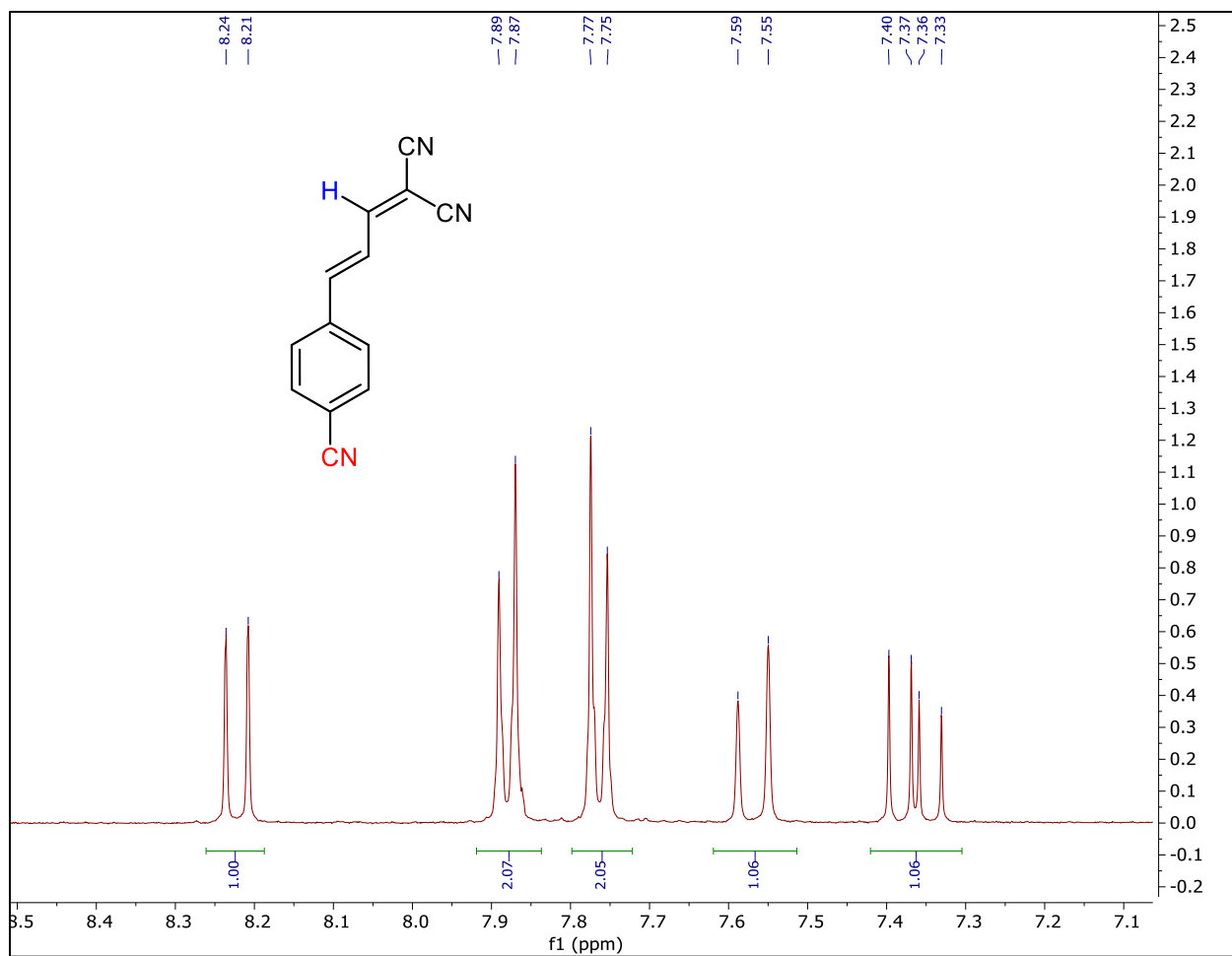


Figure S20-A: The ^1H NMR spectra of **4CNCM** in DMSO-D_6 .

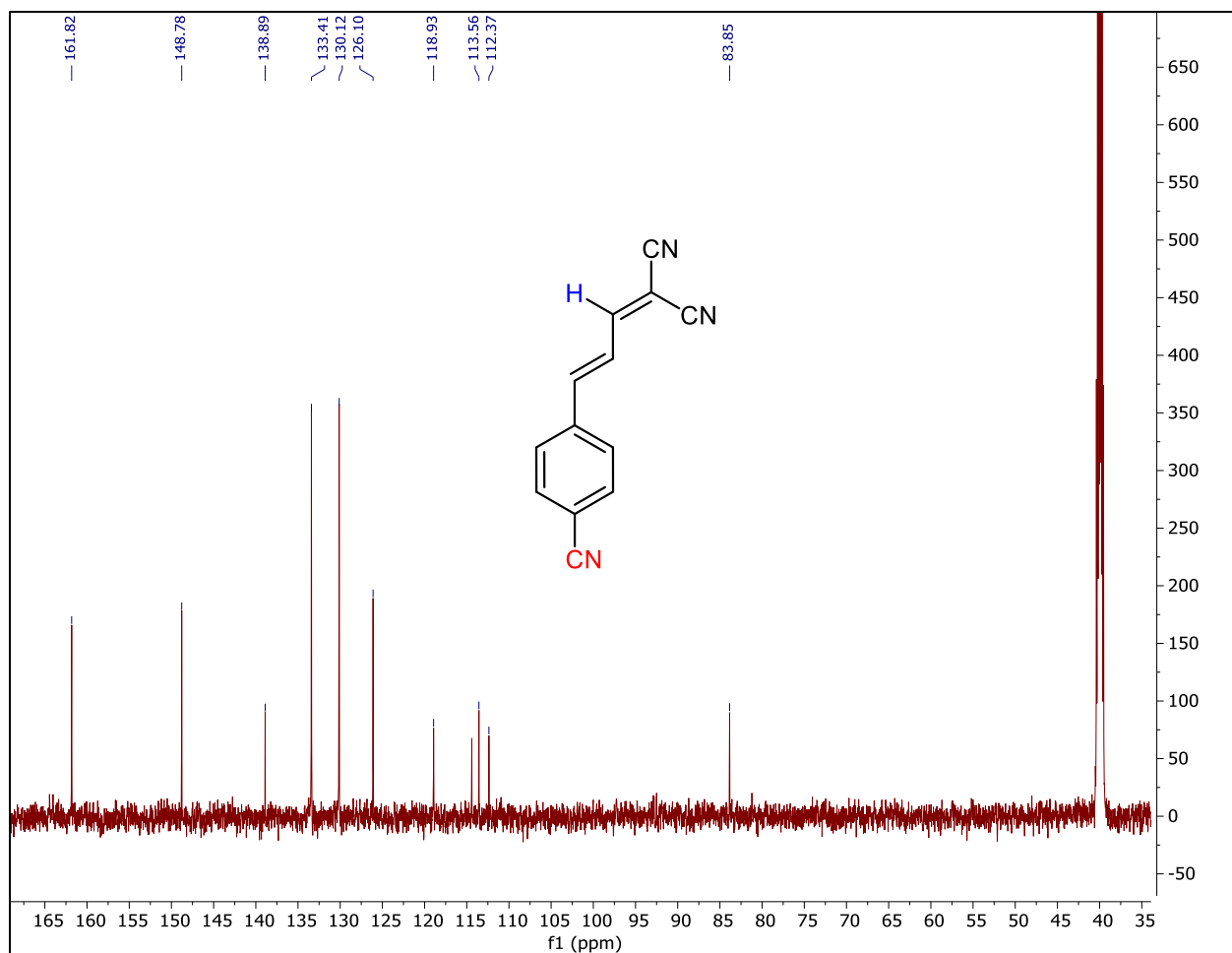


Figure S20-B: The ¹³C NMR spectra of 4CNCM in DMSO-D₆.

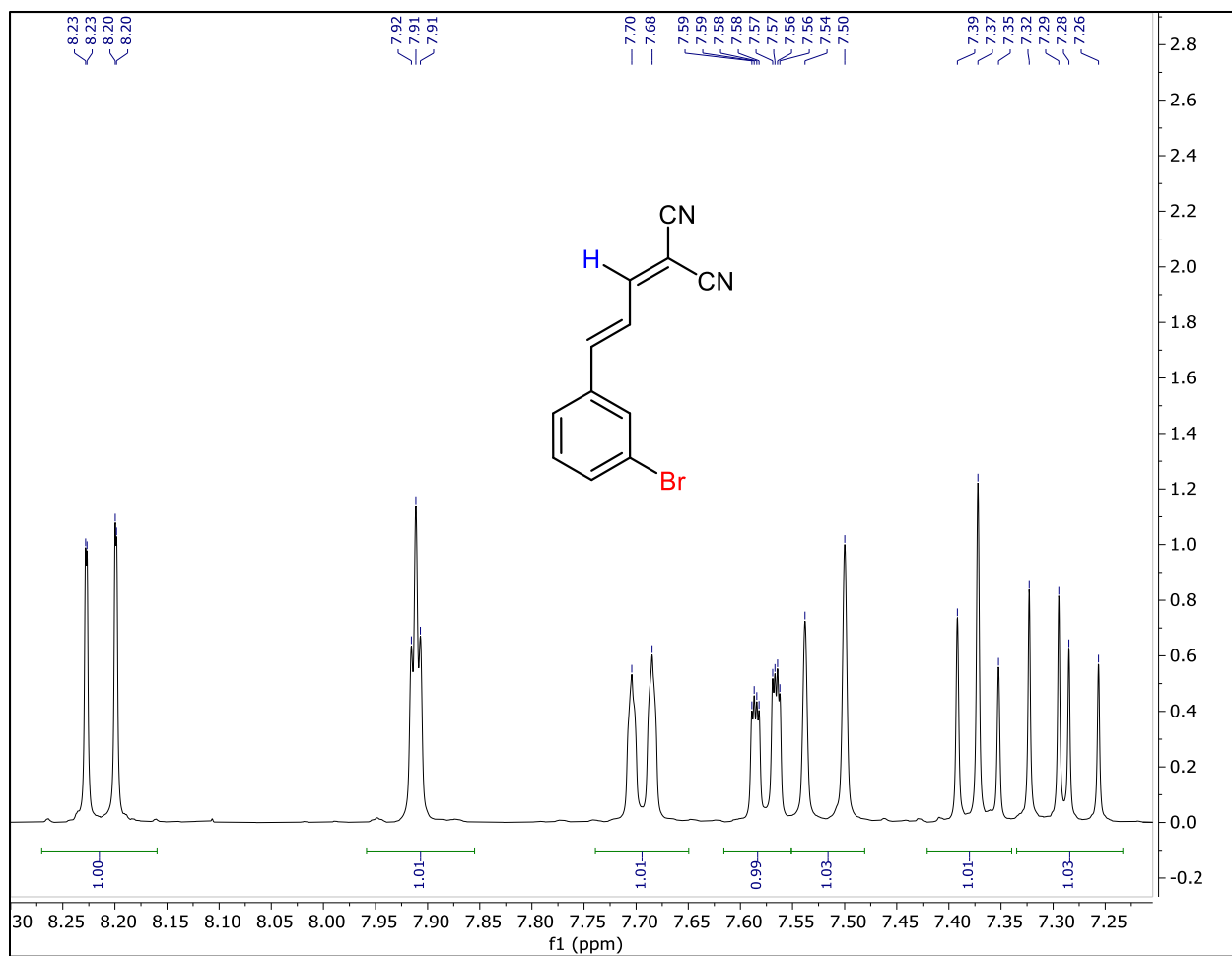


Figure S21-A: The ¹H NMR spectra of 3BrCM in DMSO-D₆.

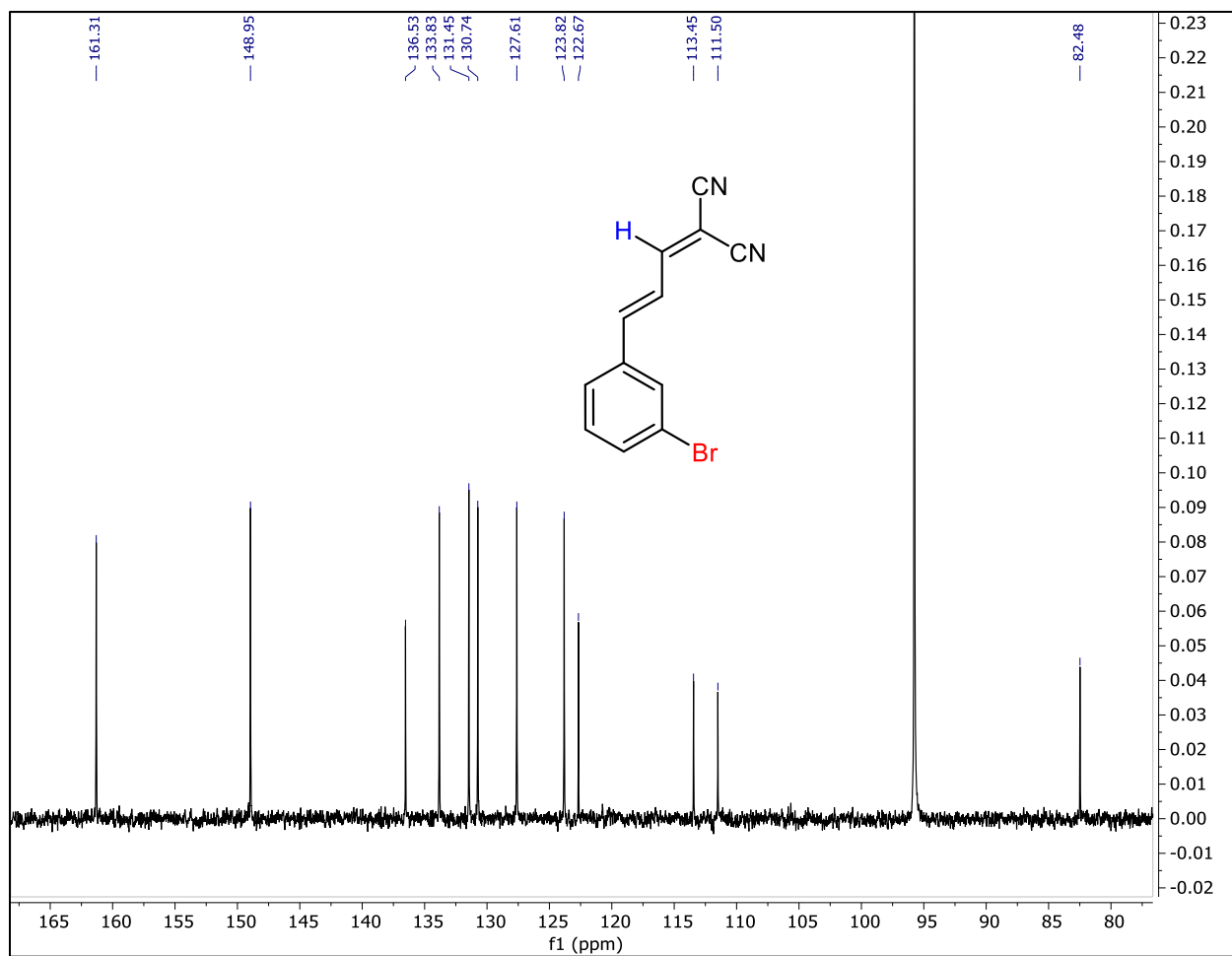


Figure S21-B: The ¹³C NMR spectra of **3BrCM** in DMSO-D₆.

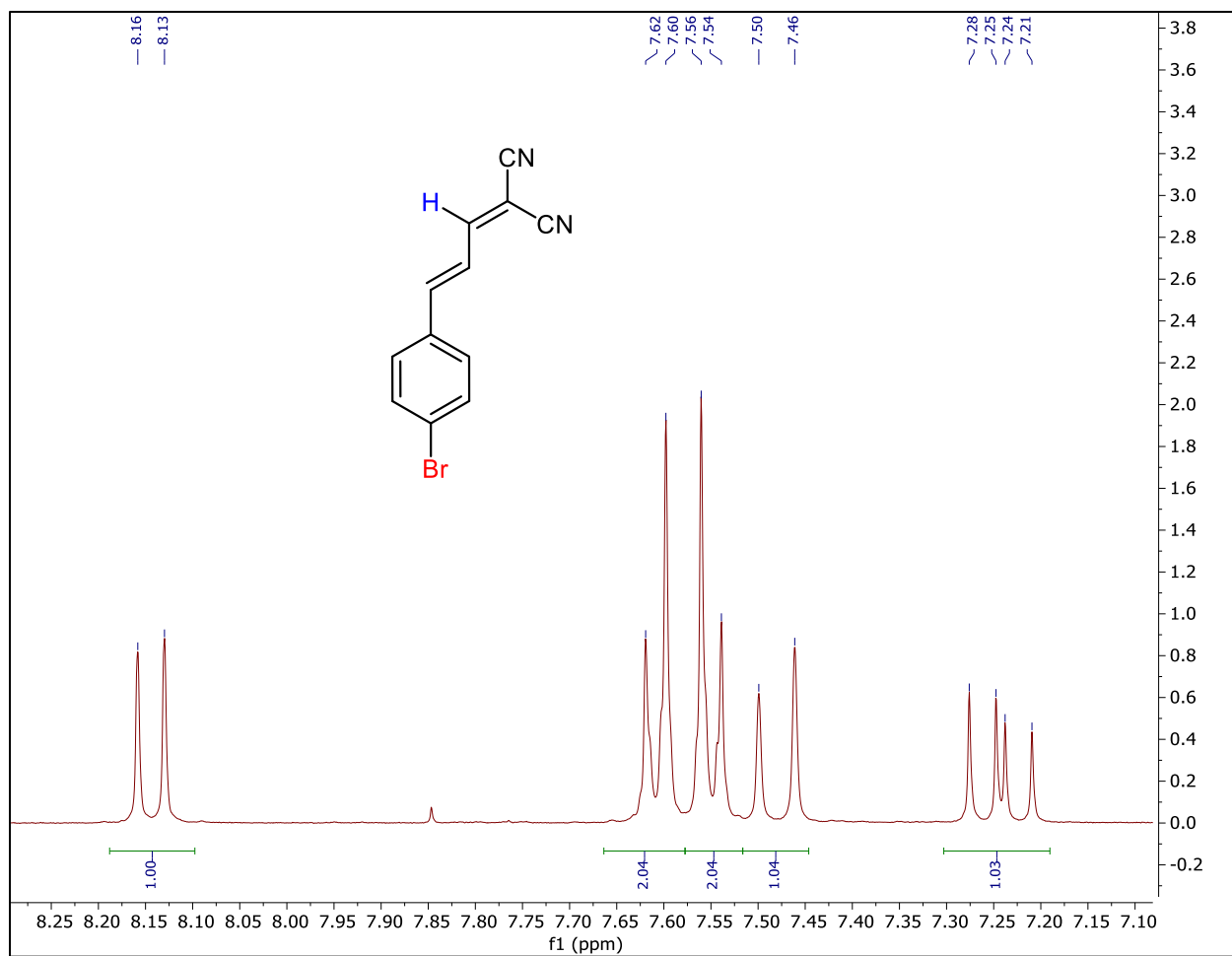


Figure S22-A: The ¹H NMR spectra of **4BrCM** in DMSO-D₆.

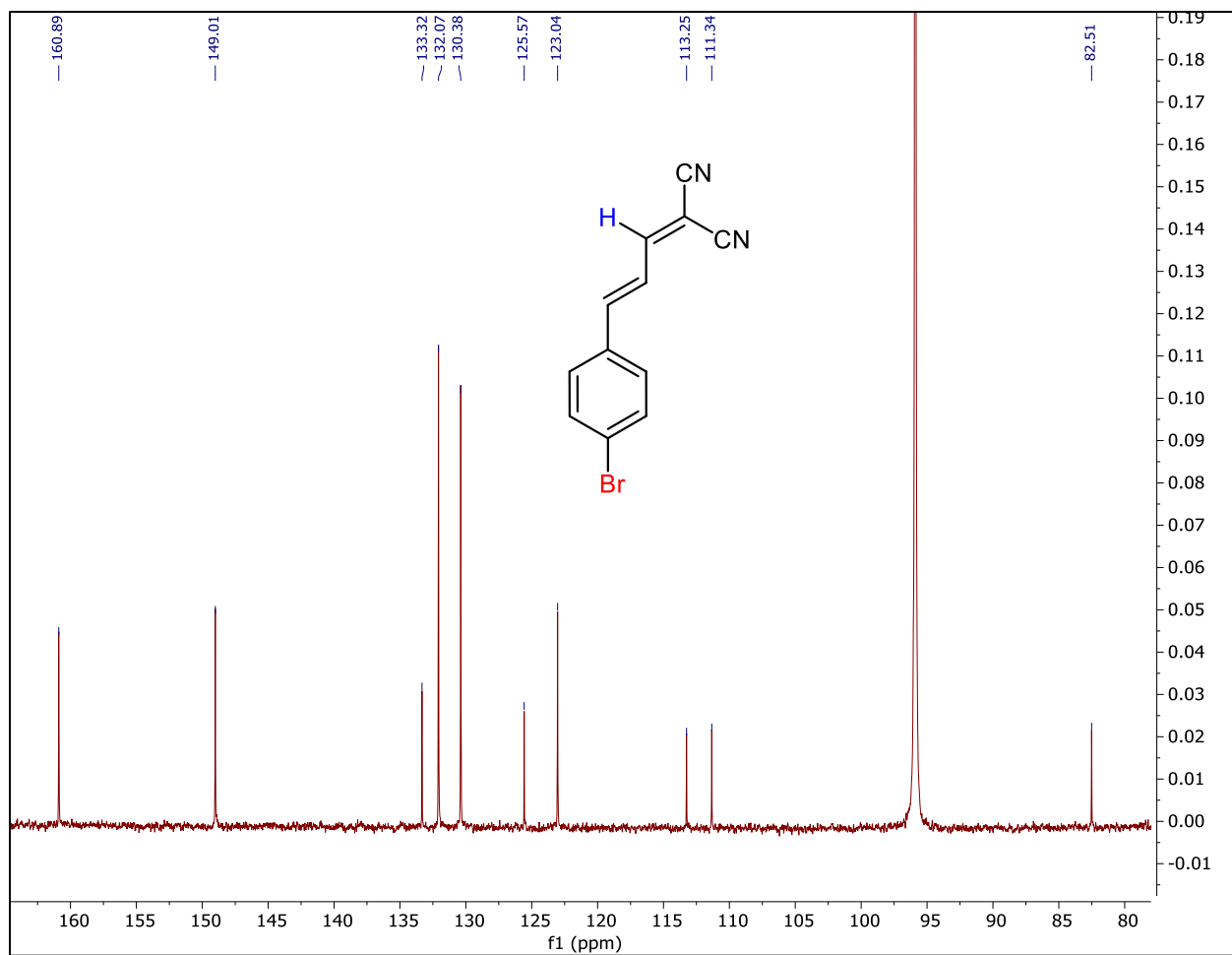


Figure S22-B: The ^{13}C NMR spectra of **4BrCM** in DMSO-D_6 .

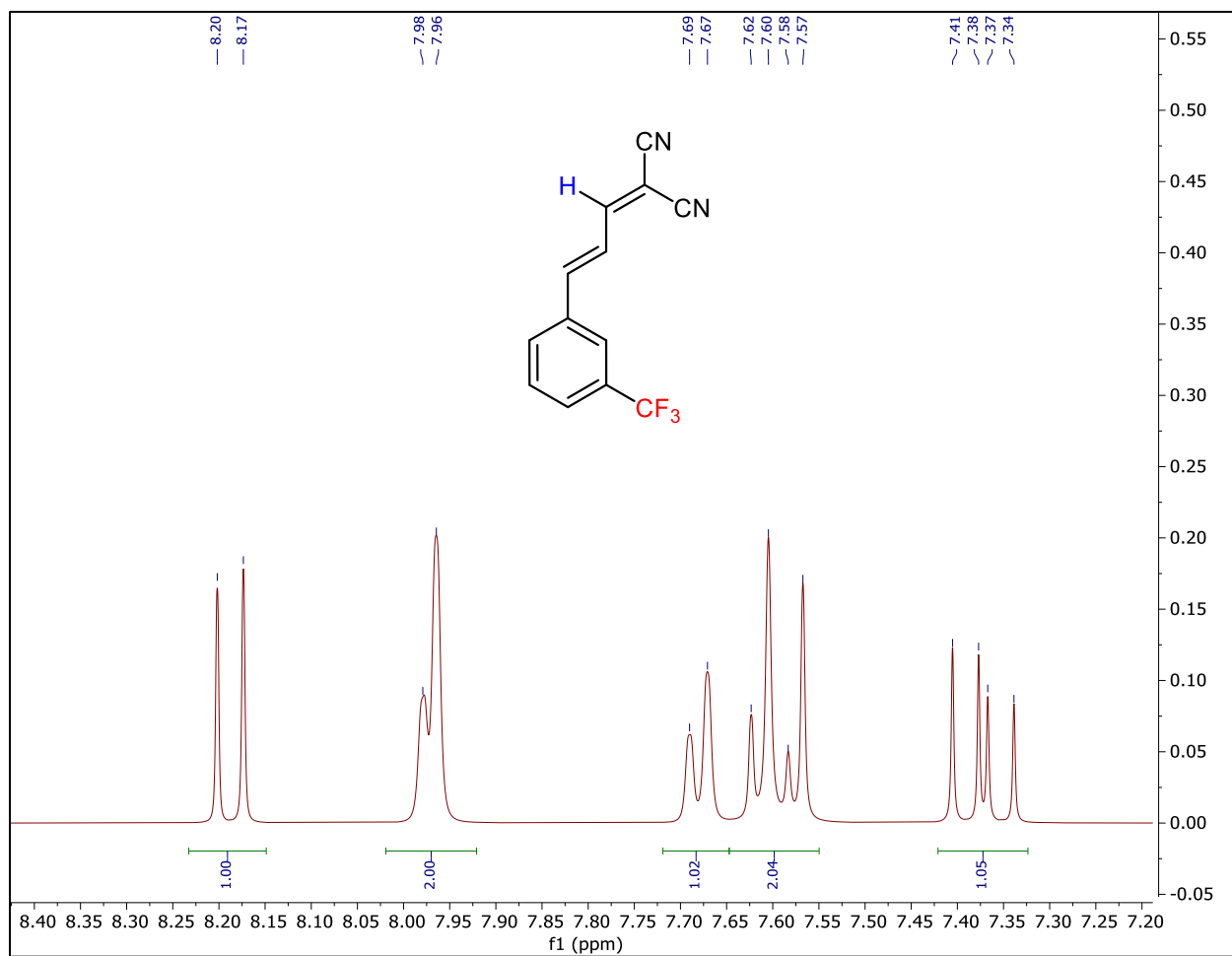


Figure S23-A: The ¹H NMR spectra of 3CF3CM in DMSO-D₆.

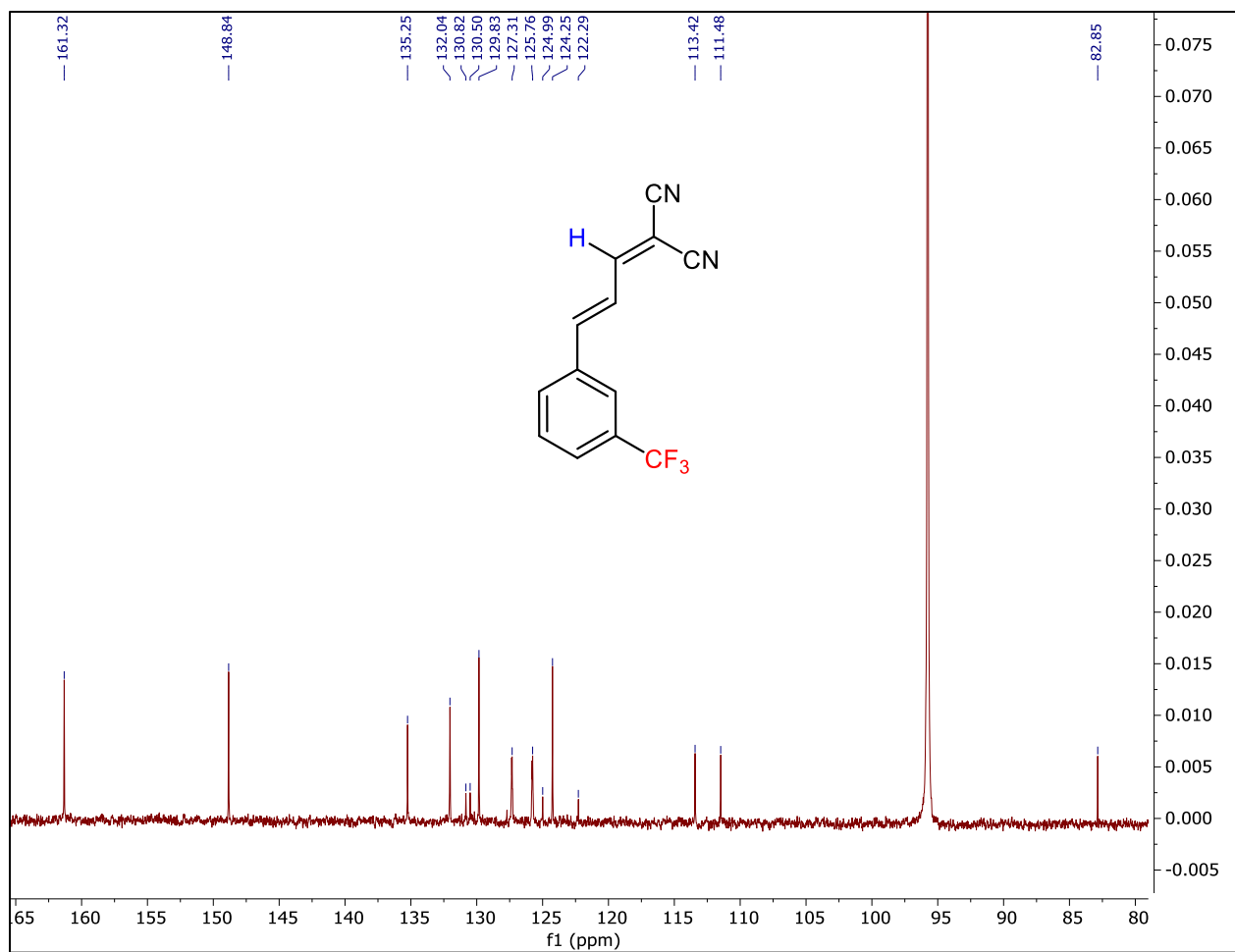


Figure S23-B: The ¹³C NMR spectra of 3CF3CM in DMSO-D₆.

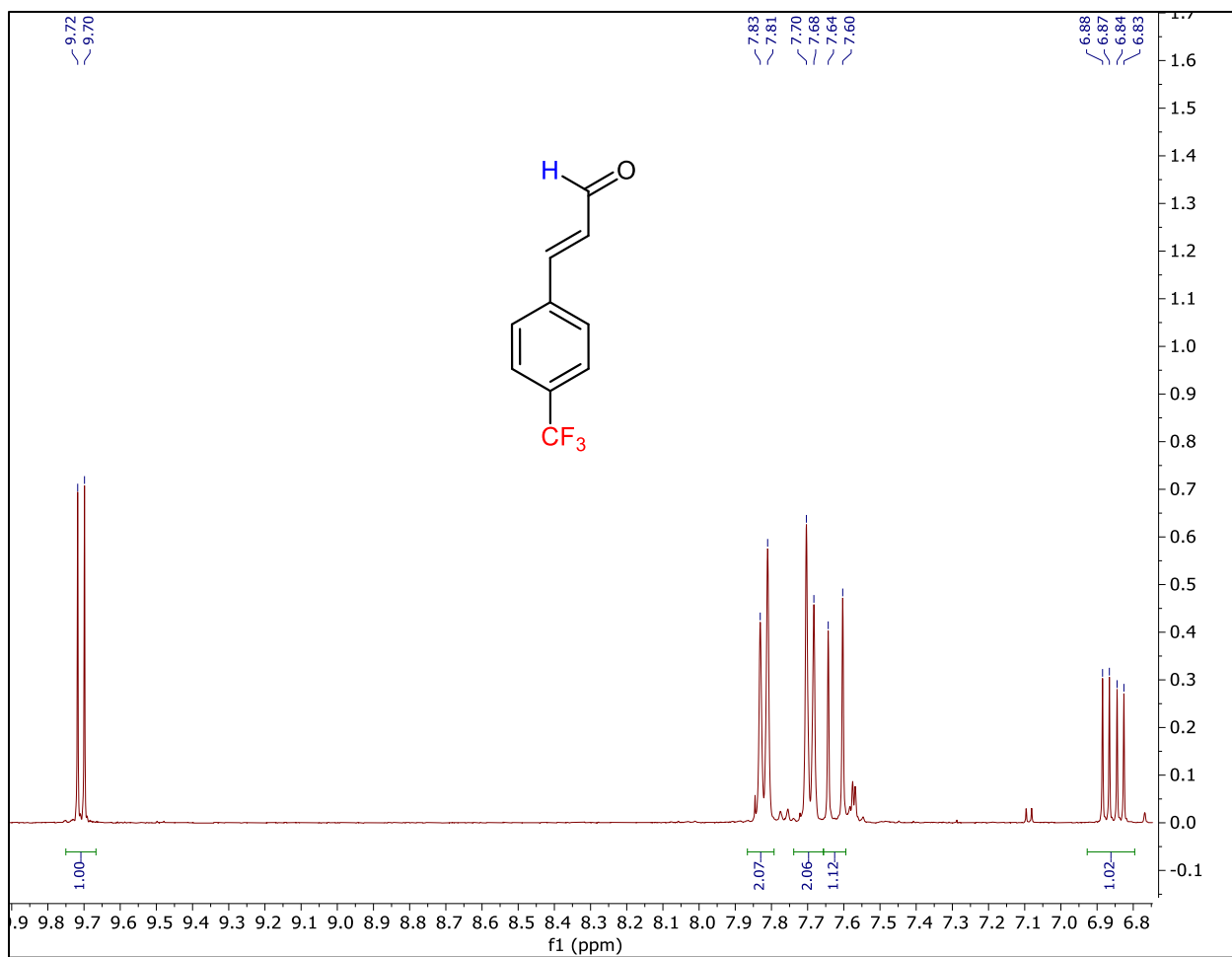


Figure S24: The ¹H NMR spectra of trans-4-Trifluoromethylcinnamaldehyde in DMSO-D₆.

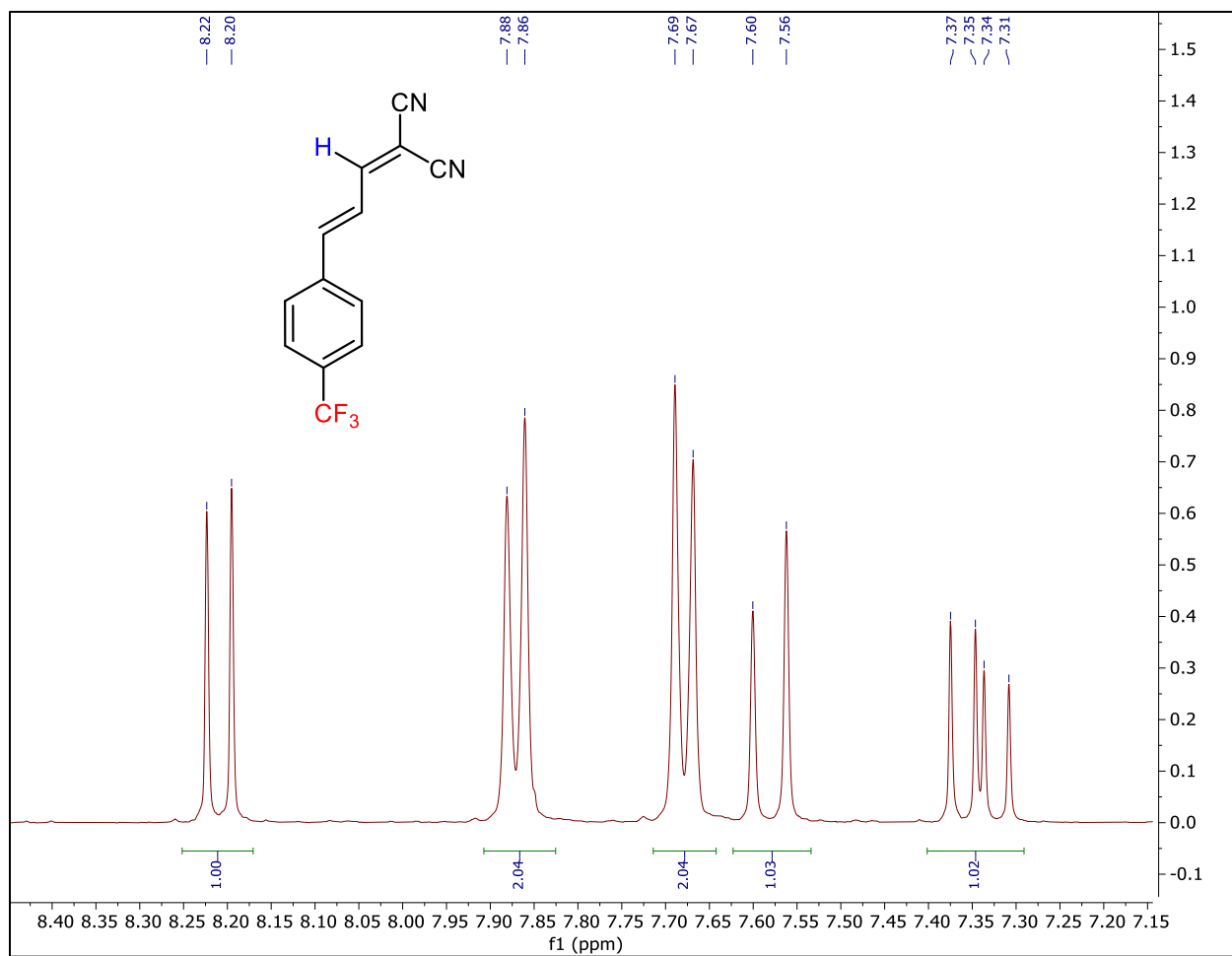


Figure S25-A: The ^1H NMR spectra of **4CF3CM** in $\text{DMSO-}D_6$.

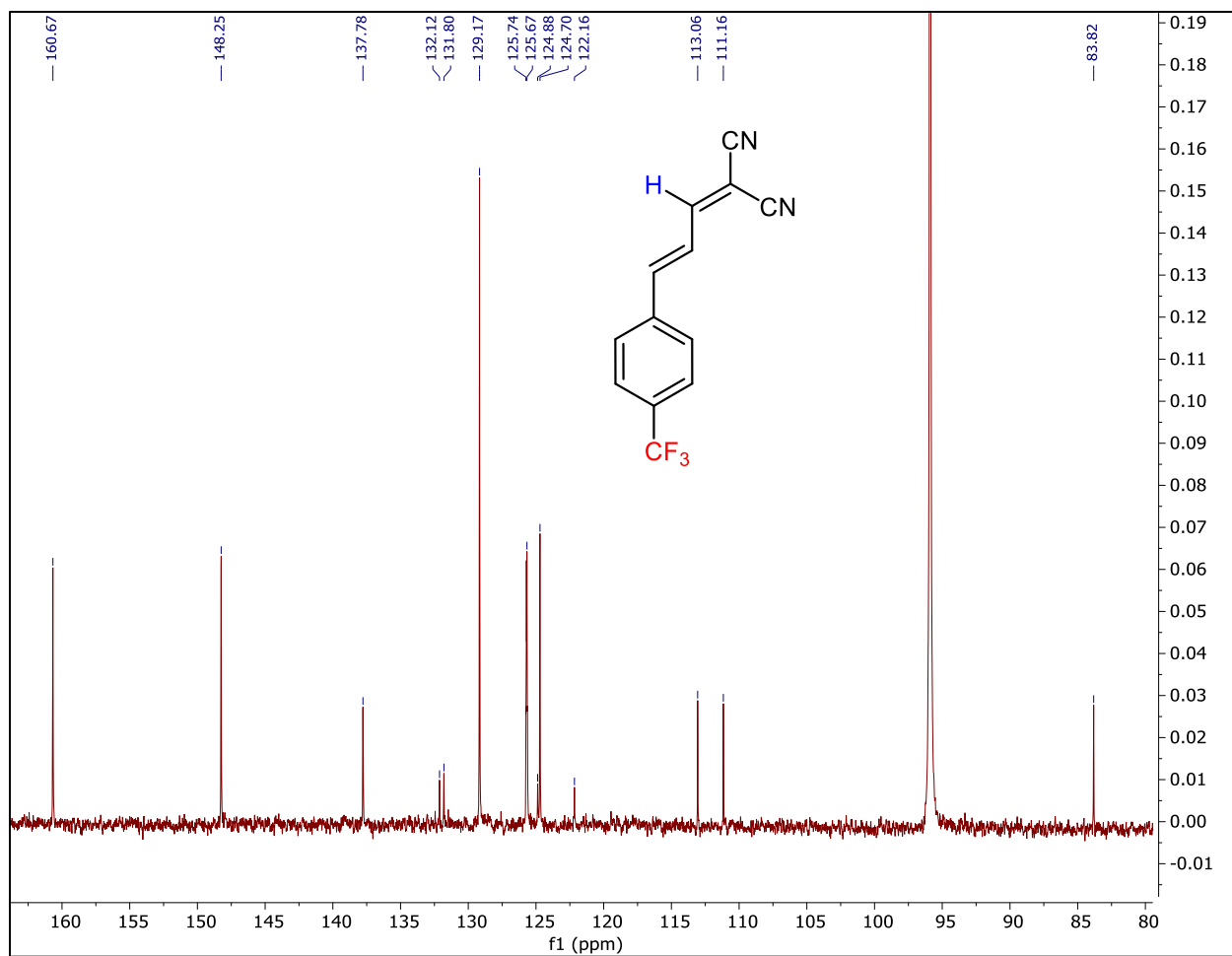


Figure S25-B: The ^{13}C NMR spectra of **4CF3CM** in $\text{DMSO-}D_6$.

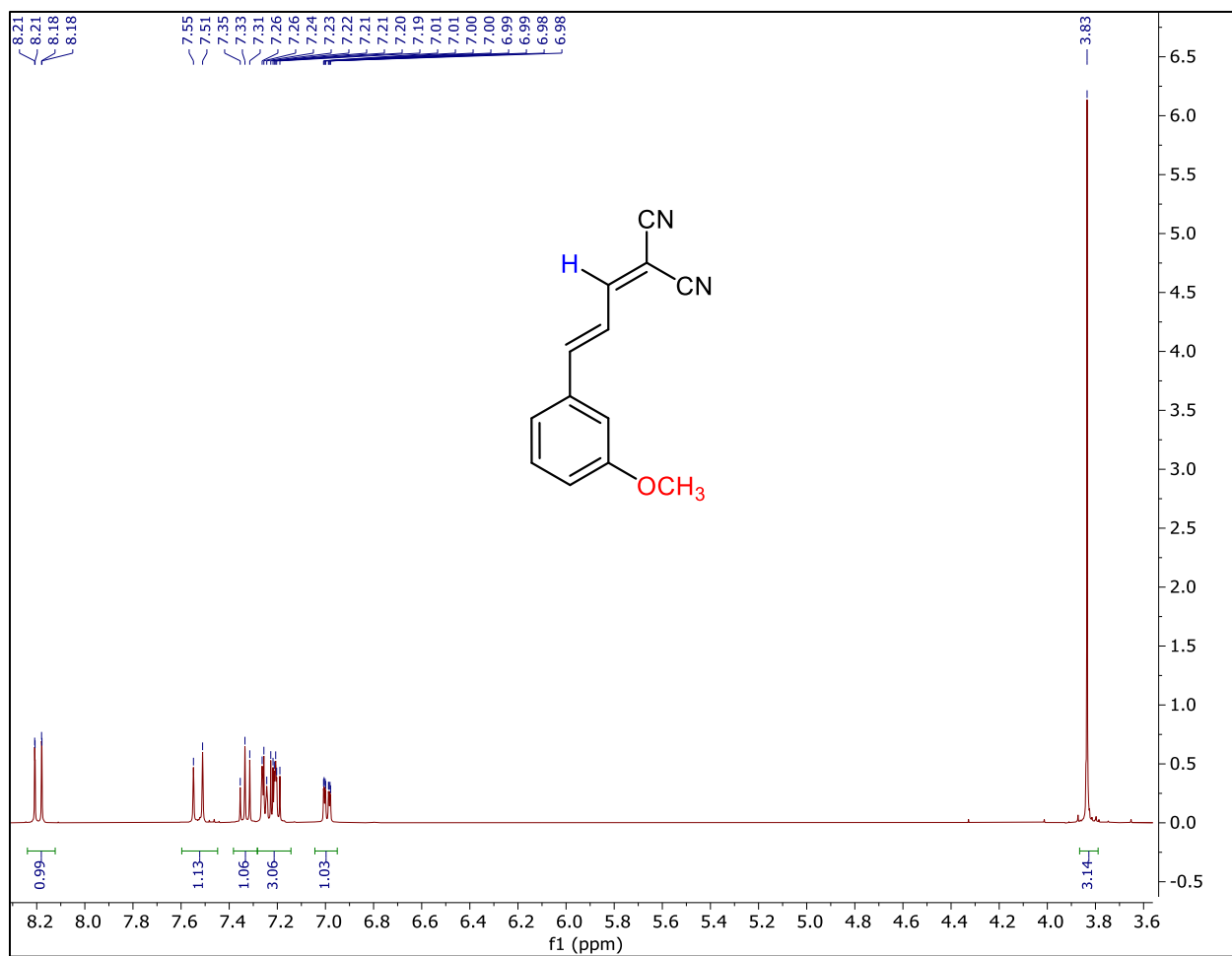


Figure S26-A: The ¹H NMR spectra of 3MethoxyCM in DMSO-D₆.

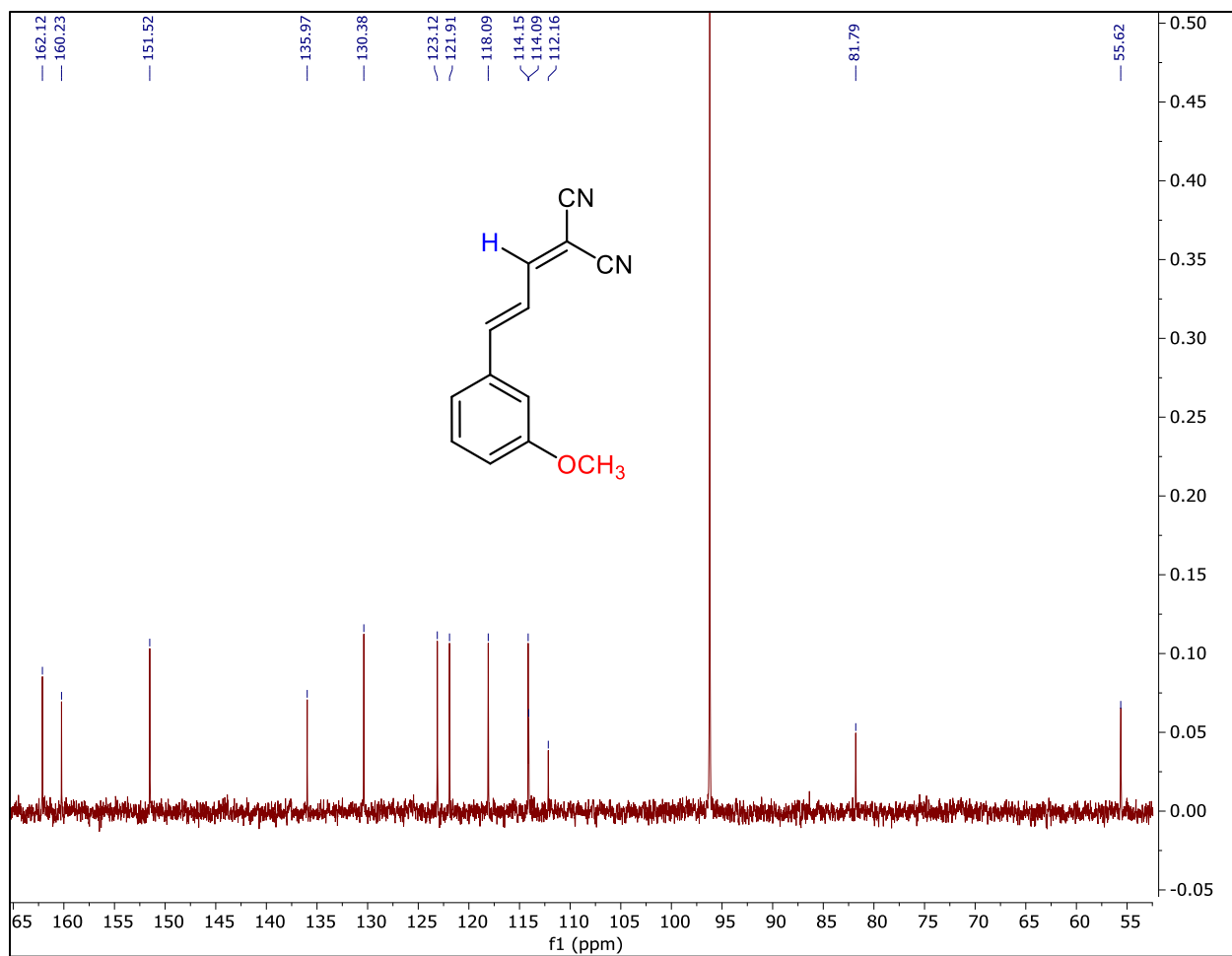


Figure S26-B: The ^{13}C NMR spectra of 3MethoxyCM in DMSO-D_6 .

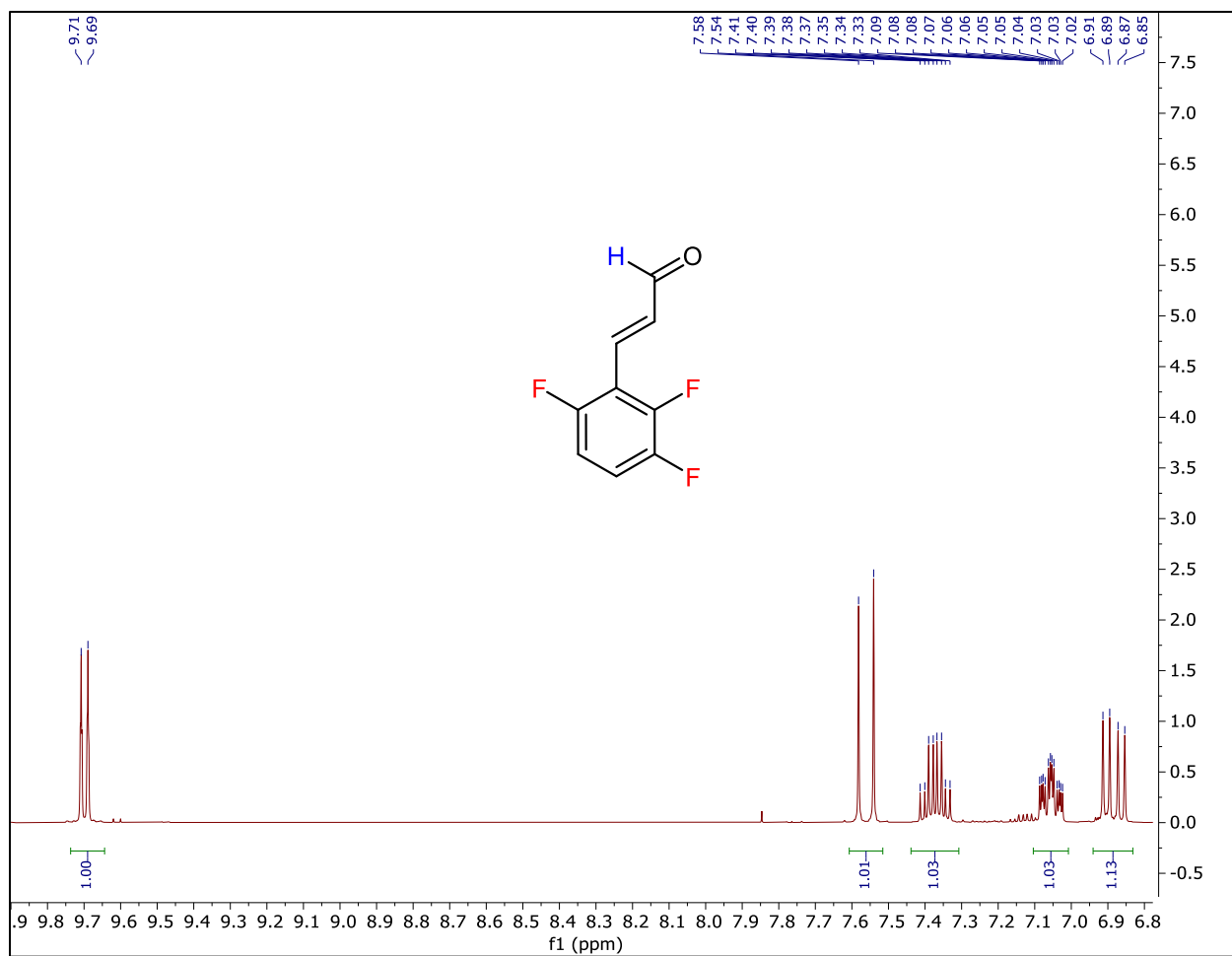


Figure S27: The ¹H NMR spectra of trans-2,3,6-Trifluorocinnamaldehyde in DMSO-D₆.

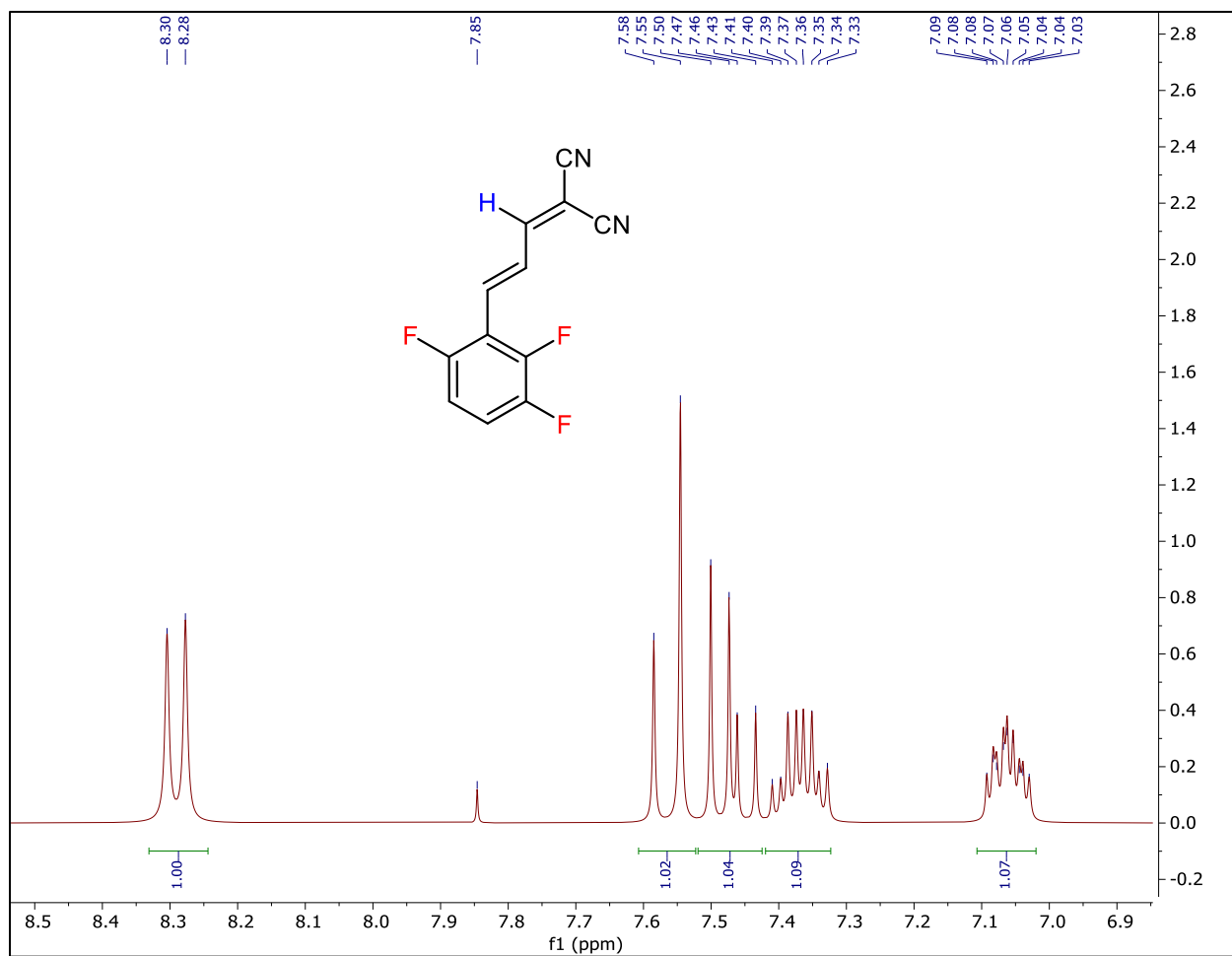


Figure S28-A: The ¹H NMR spectra of **236FCM** in DMSO-D₆.

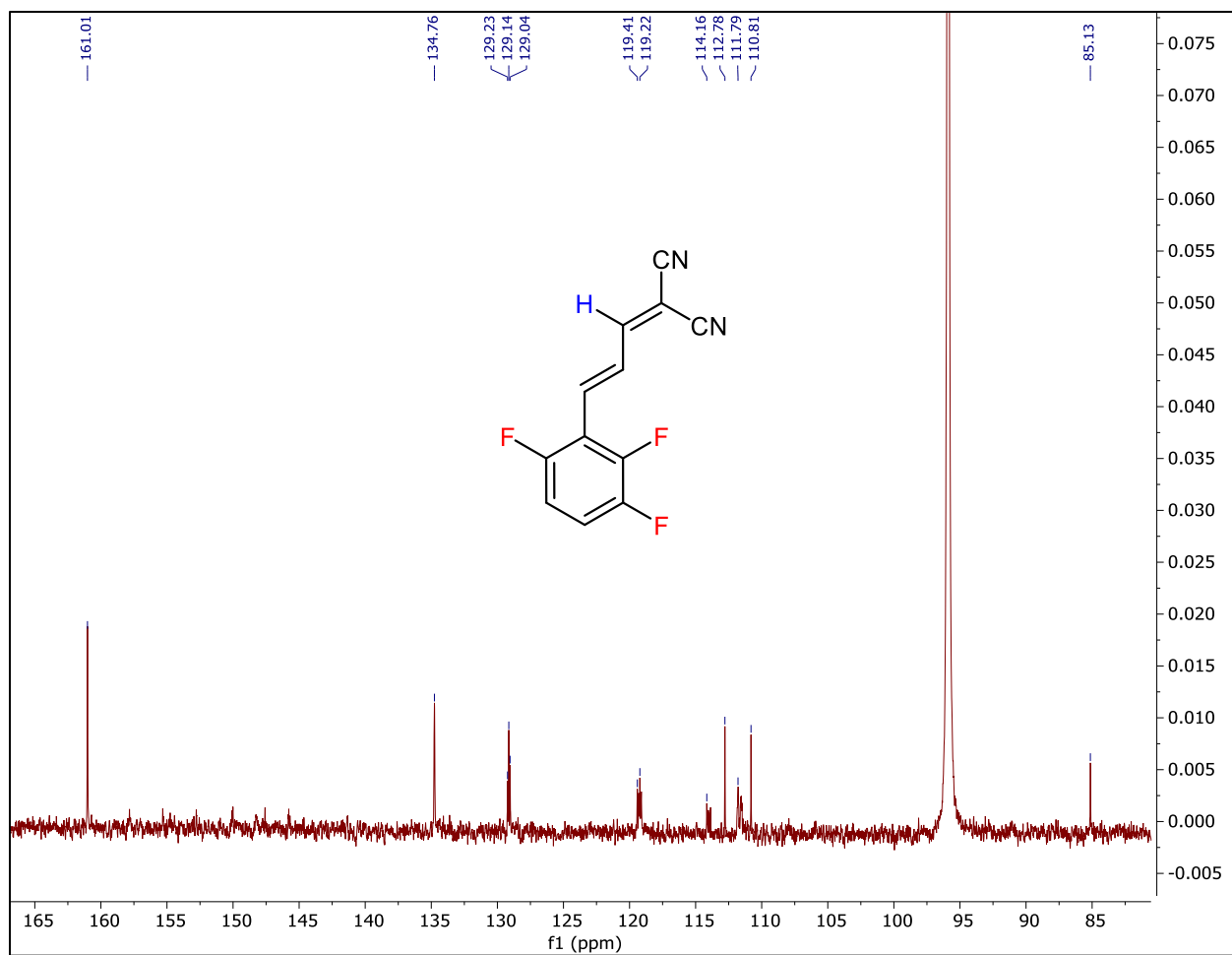


Figure S28-B: The ¹³C NMR spectra of **236FCM** in DMSO-D₆.

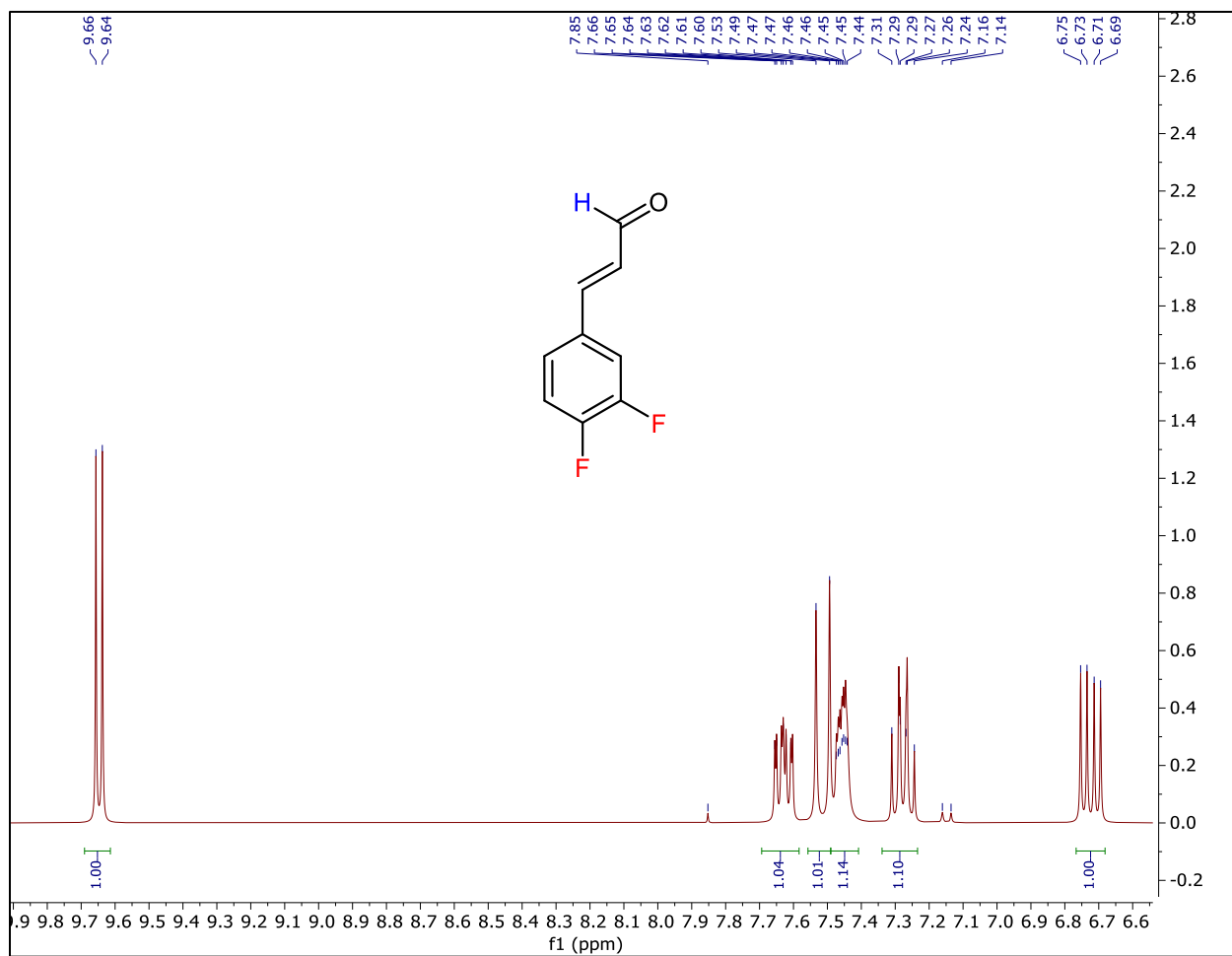


Figure S29: The ¹H NMR spectra of trans-3,4-Difluorocinnamaldehyde in DMSO-D₆.

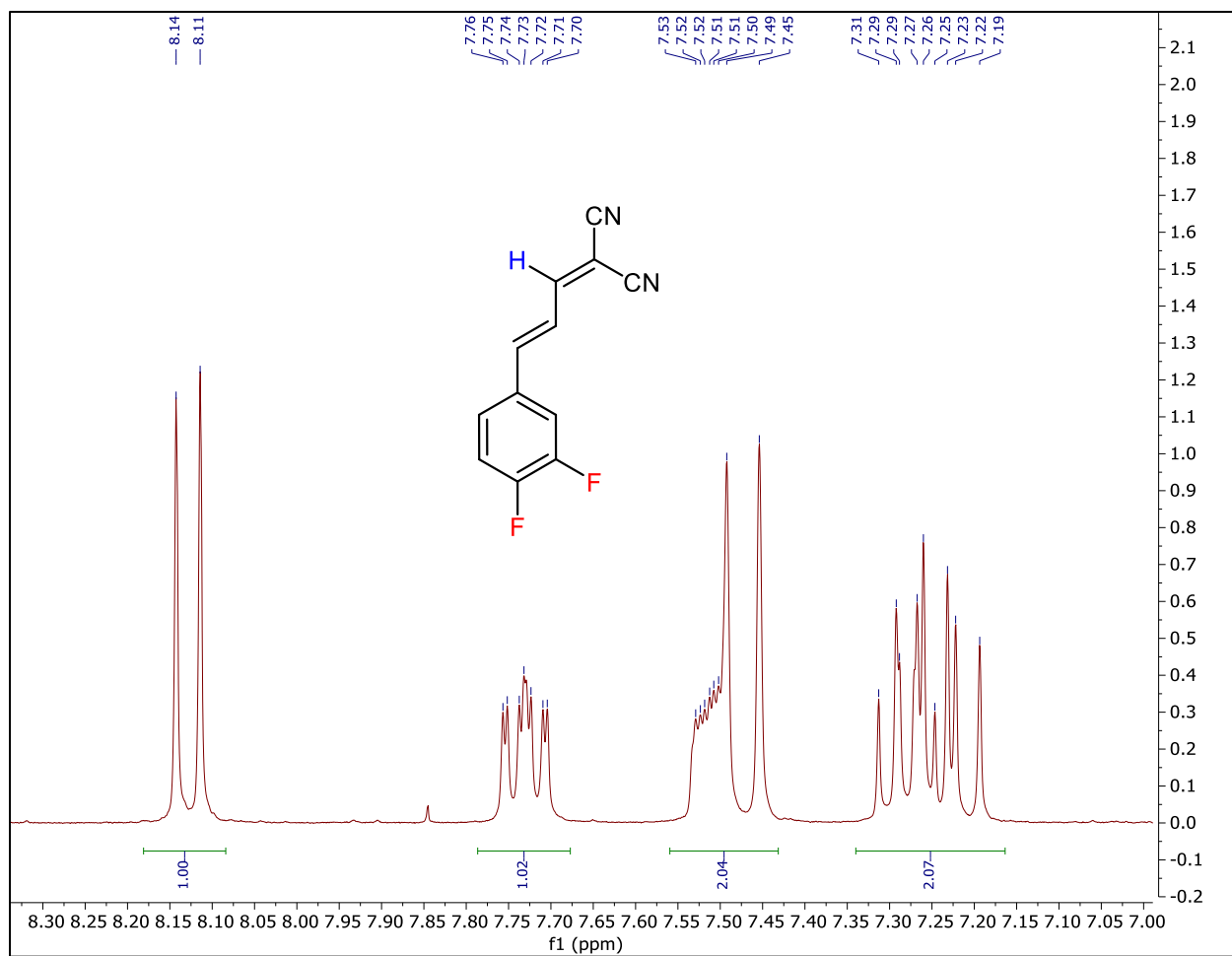


Figure S30-A: The ¹H NMR spectra of **34FCM** in DMSO-D₆.

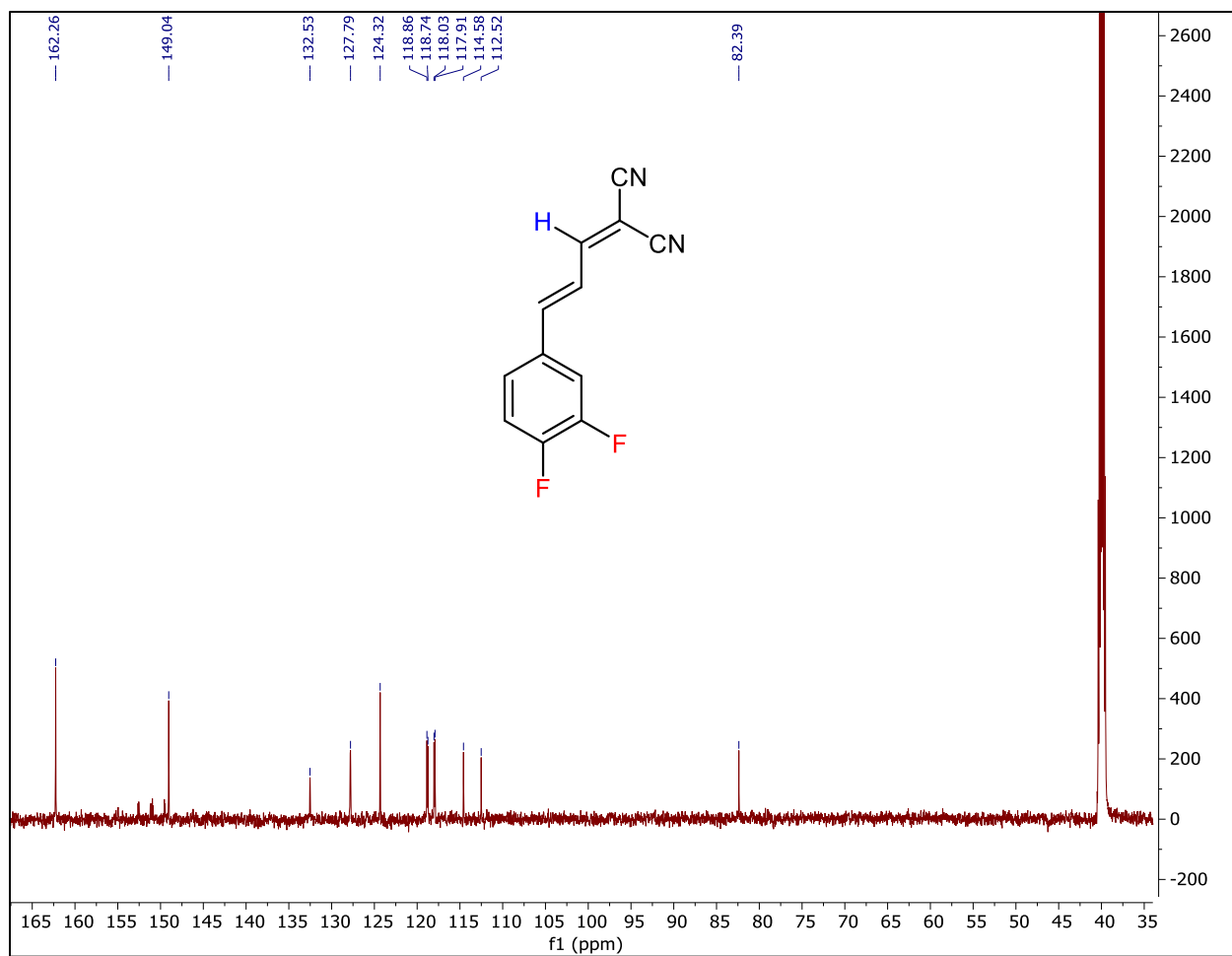


Figure S30-B: The ^{13}C NMR spectra of 34FCM in DMSO- D_6 .

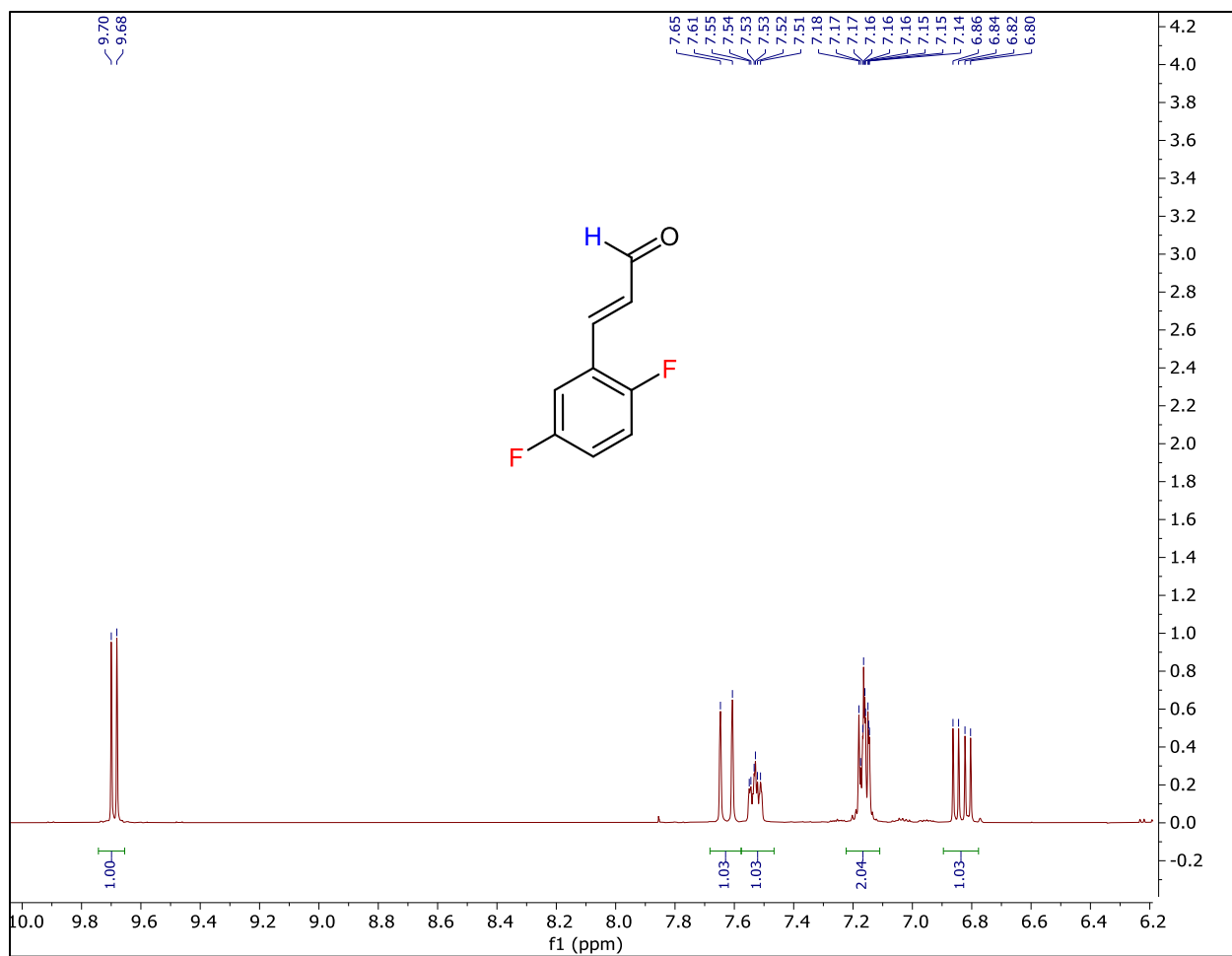


Figure S31: The ^1H NMR spectra of trans-2,5-Difluorocinnamaldehyde in DMSO- D_6 .

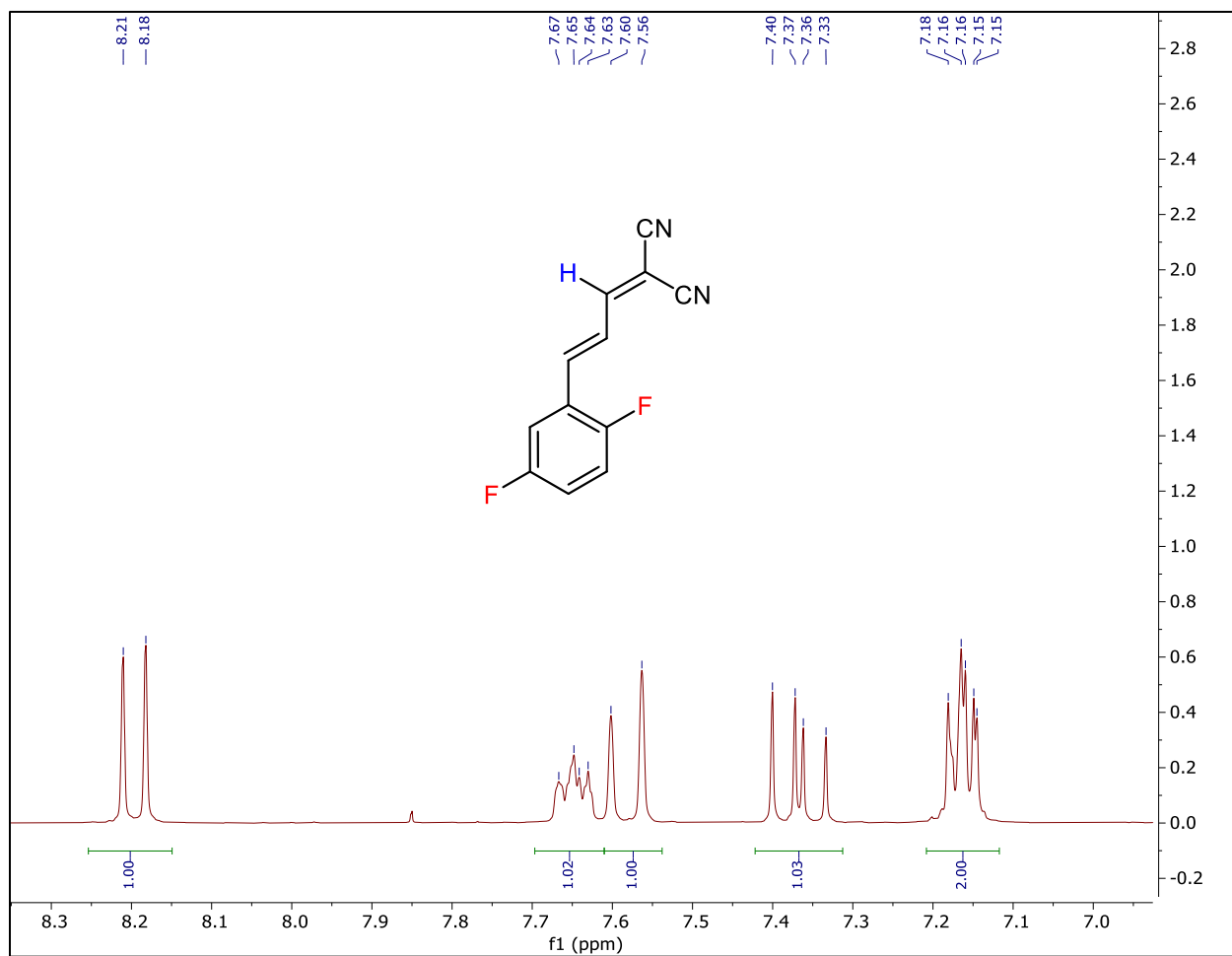


Figure S32-A: The ^1H NMR spectra of **25FCM** in $\text{DMSO-}D_6$.

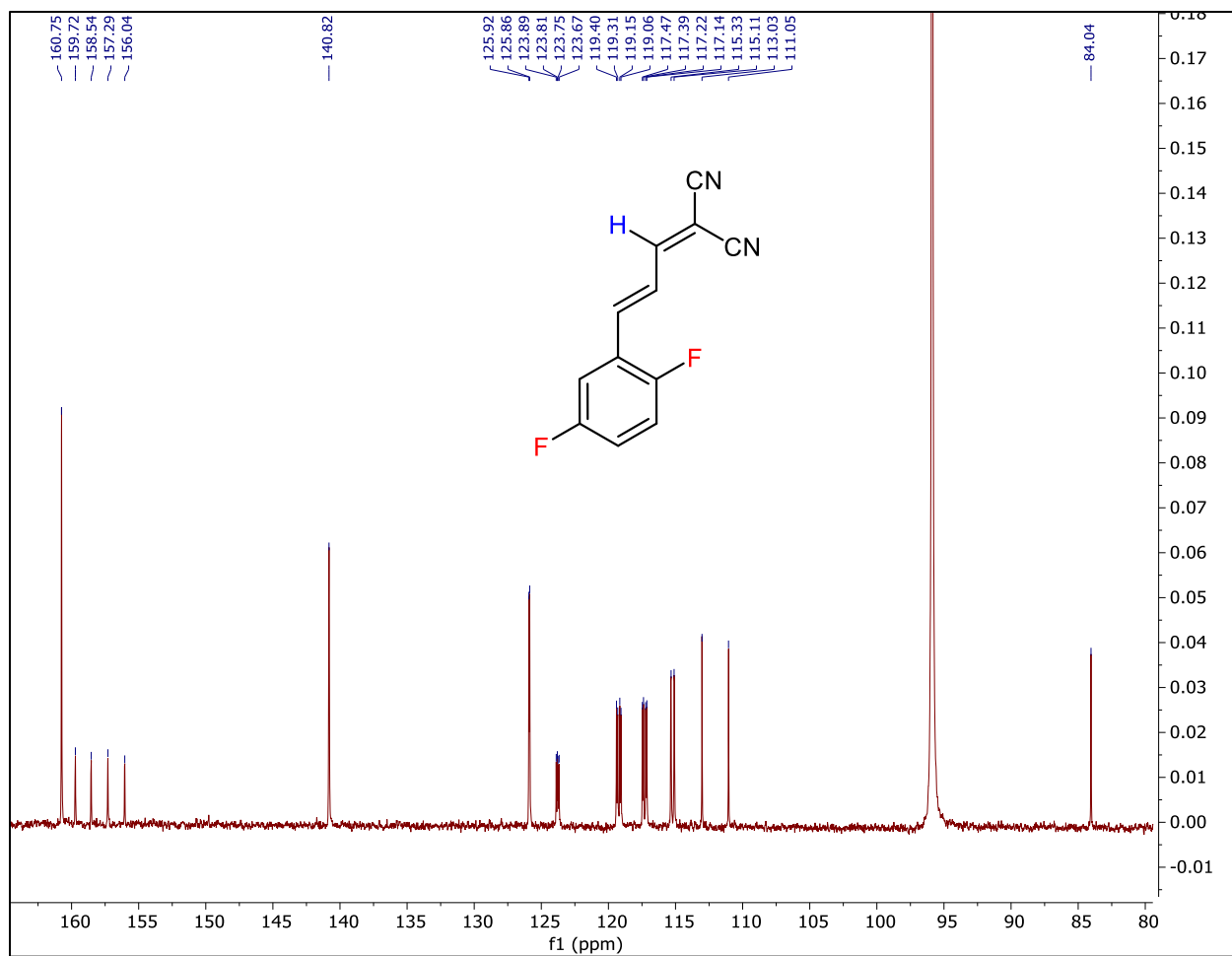


Figure S32-B: The ^{13}C NMR spectra of **25FCM** in DMSO-D_6 .

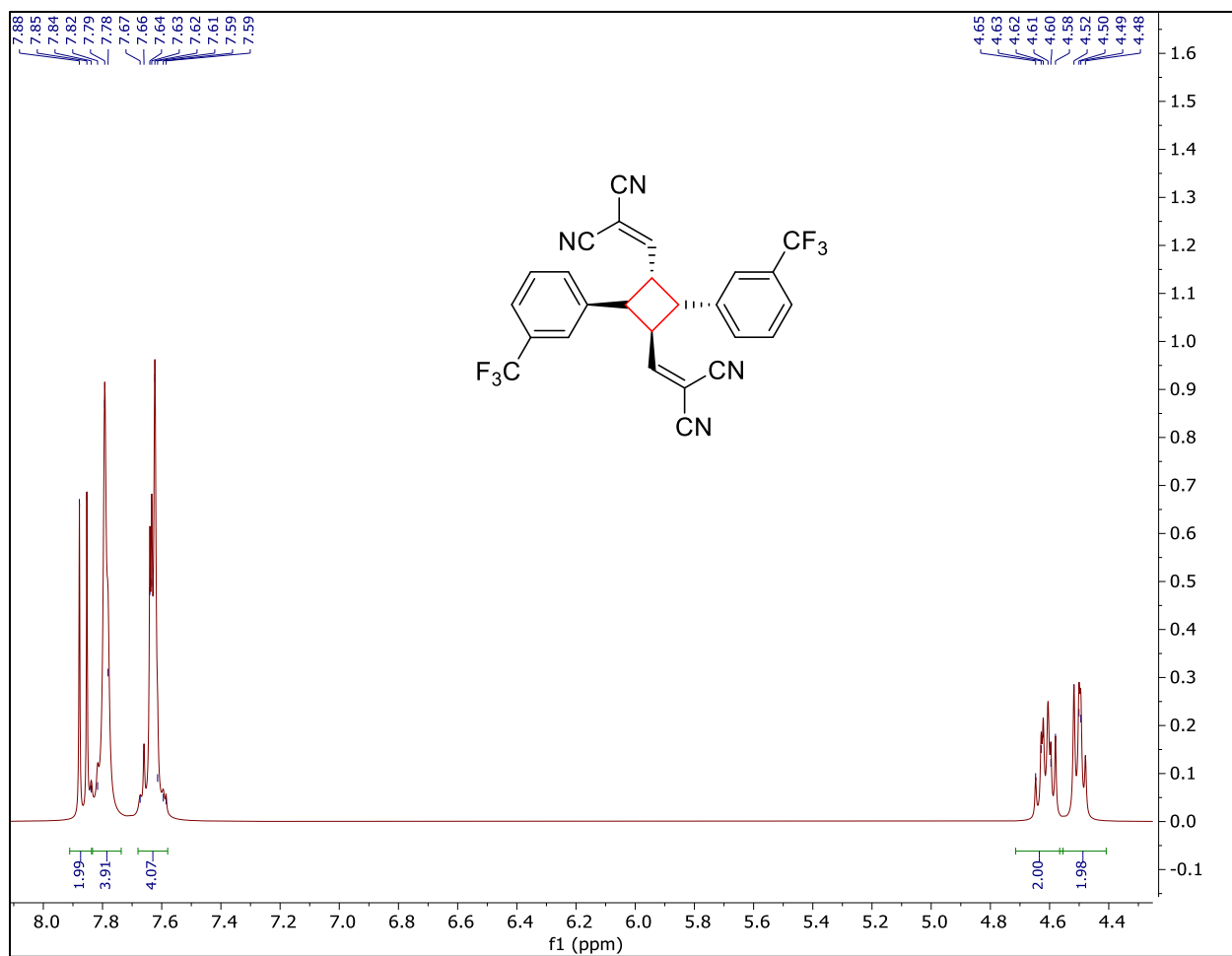


Figure S33: The ¹H NMR spectra of the dimer of 3CF₃CM in DMSO-D₆.

Table S1: Crystal Data and Structure Refinement for various CMs

	34FCM	4CF3CM	236FCM
Empirical formula	C12 H6 F2 N2	C13 H7 F3 N2	C12 H5 F3 N2
Formula weight	216.19	248.21	234.18
Crystal color, shape, size	light yellow needle, 0.53 × 0.05 × 0.03 mm ³	yellow plate, 0.46 × 0.22 × 0.09 mm ³	light yellow plate, 0.37 × 0.06 × 0.02 mm ³
Temperature	147.00 K	220.00 K	147.00 K
Wavelength	1.54178 Å	0.71073 Å	0.71073 Å
Crystal system, space group	Monoclinic, P 1 21/c 1	Orthorhombic, Pnma	Monoclinic, P 1 21/c 1
Unit cell dimensions	a = 3.7859(2) Å b = 24.6620(12) Å c = 11.1436(5) Å	a = 13.3314(13) Å b = 6.7090(7) Å c = 13.1505(13) Å	a = 3.8210(7) Å b = 11.5594(19) Å c = 23.208(3) Å
Volume	1040.33(9) Å ³	1176.2(2) Å ³	1024.6(3) Å ³
Z	4	4	4
Density (calculated)	1.380 g/cm ³	1.402 g/cm ³	1.518 g/cm ³
Absorption coefficient	0.932 mm ⁻¹	0.118 mm ⁻¹	0.131 mm ⁻¹
F(000)	440	504	472
Data collection			
Diffractometer	Bruker D8 Venture	Bruker D8 Venture	Bruker D8 Venture
Theta range for data collection	3.584 to 70.033°.	2.175 to 25.795°.	1.756 to 25.358°.
Index ranges	-4 ≤ h ≤ 4, -30 ≤ k ≤ 30, -13 ≤ l ≤ 13	-15 ≤ h ≤ 16, -8 ≤ k ≤ 8, -16 ≤ l ≤ 16	-4 ≤ h ≤ 4, -13 ≤ k ≤ 13, -27 ≤ l ≤ 27
Reflections collected	32018	23676	31165
Independent reflections	1987 [R _{int} = 0.0459]	1227 [R _{int} = 0.0604]	1882 [R _{int} = 0.0952]
Observed Reflections	1795	806	1300
Completeness to theta	99.9 %	99.7 %	99.9 %
Solution and Refinement			
Absorption correction	Semi-empirical from equivalents	Semi-empirical from equivalents	Semi-empirical from equivalents
Max. and min. transmission	0.7533 and 0.6794	0.7453 and 0.6868	0.7452 and 0.7006
Solution	Intrinsic methods	Intrinsic methods	Intrinsic methods
Refinement method	Full-matrix least-squares on F ²	Full-matrix least-squares on F ²	Full-matrix least-squares on F ²
Weighting scheme	w = [σ ² Fo ² + AP ² + BP] ⁻¹ , with P = (Fo ² + 2 Fc ²)/3, A = 0.04, B = 0.306	w = [σ ² Fo ² + AP ² + BP] ⁻¹ , with P = (Fo ² + 2 Fc ²)/3, A = 0.086, B = 0.476	w = [σ ² Fo ² + AP ² + BP] ⁻¹ , with P = (Fo ² + 2 Fc ²)/3, A = 0.075, B = 0.444
Data / restraints / parameters	1987 / 0 / 155	1227 / 24 / 117	1882 / 0 / 164

Empirical formula	3C1CM (yellow) C12 H7 Cl N2	4CF3CM C13 H7 F3 N2
Formula weight	214.65	248.21
Crystal color, shape, size	yellow block, 0.29 × 0.27 × 0.15 mm ³	yellow plate, 0.4 × 0.3 × 0.04 mm ³
Temperature	147.00 K	100.00 K
Wavelength	0.71073 Å	0.71073 Å
Crystal system, space group	Triclinic, P-1	Monoclinic, P 1 21/c 1
Unit cell dimensions	a = 7.2750(5) Å b = 9.8672(8) Å c = 15.2788(11) Å	a = 7.3922(8) Å b = 8.8613(10) Å c = 17.890(2) Å
Volume	1048.09(14) Å ³	1150.8(2) Å ³
Z	4	4
Density (calculated)	1.360 g/cm ³	1.433 g/cm ³
Absorption coefficient	0.328 mm ⁻¹	0.121 mm ⁻¹
F(000)	440	504
Data collection		
Diffractometer	Bruker D8 Venture	Bruker D8 Venture
Theta range for data collection	1.388 to 27.514°.	2.319 to 27.571°.
Index ranges	-9 ≤ h ≤ 9, -12 ≤ k ≤ 12, -19 ≤ l ≤ 19	-9 ≤ h ≤ 9, -11 ≤ k ≤ 11, -23 ≤ l ≤ 23
Reflections collected	44323	37061
Independent reflections	4823 [R _{int} = 0.0877]	2648 [R _{int} = 0.0836]
Observed Reflections	3808	2126
Completeness to theta	99.9 %	99.5 %
Solution and Refinement		
Absorption correction	Semi-empirical from equivalents	Semi-empirical from equivalents
Max. and min. transmission	0.7448 and 0.7177	0.7456 and 0.6021
Solution	Intrinsic methods	Intrinsic methods
Refinement method	Full-matrix least-squares on F ²	Full-matrix least-squares on F ²
Weighting scheme	w = [σ ² Fo ² + AP ² + BP] ⁻¹ , with P = (Fo ² + 2 Fc ²)/3, A = 0.048, B = 0.417	w = [σ ² Fo ² + AP ² + BP] ⁻¹ , with P = (Fo ² + 2 Fc ²)/3, A = 0.059, B = 1.21
Data / restraints / parameters	4823 / 0 / 271	2648 / 10 / 172

	25FCM	3CICM (colorless)	4CICM
Empirical formula	C ₁₂ H ₆ F ₂ N ₂	C ₁₂ H ₇ ClN ₂	C ₁₂ H ₇ ClN ₂
Formula weight	216.19	214.65	214.65
Crystal color, shape, size	yellow needle, 0.6 × 0.08 × 0.03 mm ³	colourless plate, 0.27 × 0.09 × 0.03 mm ³	yellow plate, 0.12 × 0.1 × 0.02 mm ³
Temperature	147.00 K	148.00 K	100.00 K
Wavelength	0.71073 Å	1.54178 Å	1.54178 Å
Crystal system, space group	Monoclinic, P 1 21/c 1	Monoclinic, P 1 21/c 1	Monoclinic, C 1 c 1
Unit cell dimensions	a = 3.823(3) Å a = 90°. b = 11.371(11) Å b = 90.09(2)°. c = 23.01(2) Å g = 90°.	a = 7.2875(6) Å □ = 90°. b = 7.4135(5) Å □ = 98.406(6)°. c = 20.1102(18) Å □ = 90°.	a = 23.024(2) Å a = 90°. b = 3.7968(4) Å b = 89.952(7)°. c = 23.469(2) Å g = 90°.
Volume	1000.4(16) Å ³	1074.80(15) Å ³	2051.6(4) Å ³
Z	4	4	8
Density (calculated)	1.435 g/cm ³	1.326 g/cm ³	1.390 g/cm ³
Absorption coefficient	0.114 mm ⁻¹	2.854 mm ⁻¹	2.991 mm ⁻¹
F(000)	440	440	880
Data collection			
Diffractometer	Bruker D8 Venture	Bruker D8 Venture	Bruker D8 Venture
Theta range for data collection	1.770 to 26.091°. -4<=h<=4, -13<=k<=14, -28<=l<=28	2.221 to 66.592°. -8<=h<=8, -8<=k<=8, -23<=l<=23	1.882 to 66.573°. -26<=h<=26, -4<=k<=4, -27<=l<=27
Index ranges	20813	18093	8469
Reflections collected	1969 [R _{int} = 0.1419]	1926 [R _{int} = 0.0755]	3425 [R _{int} = 0.0846]
Independent reflections	1287	1674	3189
Observed Reflections	99.9 %	99.2 %	100.0 %
Completeness to theta			
Solution and Refinement			
Absorption correction	Semi-empirical from equivalents	Semi-empirical from equivalents	Semi-empirical from equivalents
Max. and min. transmission	0.7453 and 0.5397	0.7533 and 0.4764	0.7494 and 0.5369
Solution	Intrinsic methods	Intrinsic methods	Intrinsic methods
Refinement method	Full-matrix least-squares on F ²	Full-matrix least-squares on F ²	Full-matrix least-squares on F ²
Weighting scheme	w = [s ² Fo ² + AP ² + BP] ⁻¹ , with P = (Fo ² + 2 Fc ²)/3, A = 0.129, B = 0.0	w = [□ ² Fo ² + AP ² + BP] ⁻¹ , with P = (Fo ² + 2 Fc ²)/3, A = 0.195, B = 5.55	w = [s ² Fo ² + AP ² + BP] ⁻¹ , with P = (Fo ² + 2 Fc ²)/3, A = 0.121, B = 7.73
Data / restraints / parameters	1969 / 0 / 146	1926 / 0 / 137	3425 / 194 / 274
Goodness-of-fit on F ²	1.001	1.034	1.087
Final R indices [I>2s(I)]	R1 = 0.0690, wR2 = 0.1765	R1 = 0.1216, wR2 = 0.3301	R1 = 0.0868, wR2 = 0.2147
R indices (all data)	R1 = 0.1018, wR2 = 0.2116	R1 = 0.1323, wR2 = 0.3430	R1 = 0.0929, wR2 = 0.2211
Largest diff. peak and hole	0.241 and -0.293 e.Å ⁻³	1.383 and -0.450 e.Å ⁻³	0.09(5) and 0.06(5) 0.993 and -0.487 e.Å ⁻³
Twin Details			
Type, twin law	pseudomerohedral -1 0 0, 0 -1 0, 0.02 0 1	pseudomerohedral, -1 0 0, 0 -1 0, 0.8 0 1	pseudomerohedral (-1 0 0, 0 -1 0, 0 0 1)
Twin element, domain ratio	2-fold rotation about c, 47:63	180° rotation around c, 89:11	inversion (-1 0 0, 0 -1 0, 0 -1) 2-fold rotation around [0 0 1] 57:43

	3MethoxyCM	4BrCM	4ClCM
Empirical formula	C13 H10 N2 O	C12 H7 Br N2	C12 H7 Br N2
Formula weight	210.23	259.11	259.11
Crystal color, shape, size	light yellow plate, 0.11 × 0.07 × 0.03 mm ³	yellow plate, 0.4 × 0.11 × 0.04 mm ³	yellow block, 0.26 × 0.16 × 0.12 mm ³
Temperature	100.00 K	148.00 K	100.00 K
Wavelength	0.71073 Å	0.71073 Å	0.71073 Å
Crystal system, space group	Monoclinic, P 1 21/m 1	Orthorhombic, Pca2 ₁	Triclinic, P-1
Unit cell dimensions	a = 6.6557(10) Å a = 90°. b = 6.1102(12) Å b = 97.669(6)°. c = 13.441(3) Å g = 90°.	a = 25.484(3) Å a = 90°. b = 3.8756(4) Å b = 90°. c = 10.6963(9) Å g = 90°.	a = 7.2852(5) Å a = 102.831(2)°. b = 9.6296(6) Å b = 98.093(2)°. c = 15.9604(9) Å g = 97.966(2)°.
Volume	541.74(17) Å ³	1056.44(17) Å ³	1063.98(12) Å ³
Z	2	4	4
Density (calculated)	1.289 g/cm ³	1.629 g/cm ³	1.618 g/cm ³
Absorption coefficient	0.084 mm ⁻¹	3.855 mm ⁻¹	3.828 mm ⁻¹
F(000)	220	512	512
Data collection			
Diffractometer	Bruker D8 Venture	Bruker D8 Venture	Bruker D8 Venture
Theta range for data collection	1.529 to 25.345°.	1.598 to 25.681°.	2.203 to 26.370°.
Index ranges	-7<=h<=8, -7<=k<=7, -16<=l<=16	-31<=h<=31, -4<=k<=4, -12<=l<=13	-9<=h<=9, -12<=k<=12, -19<=l<=19
Reflections collected	16638	21824	38269
Independent reflections	1086 [R _{int} = 0.1095]	1983 [R _{int} = 0.0798]	4330 [R _{int} = 0.0680]
Observed Reflections	751	1794	3574
Completeness to theta	99.7 %	100.0 %	99.9 %
Solution and Refinement			
Absorption correction	Semi-empirical from equivalents	Semi-empirical from equivalents	Semi-empirical from equivalents
Max. and min. transmission	0.7453 and 0.6756	0.7454 and 0.6045	0.7454 and 0.6413
Solution	Intrinsic methods	Intrinsic methods	Intrinsic methods
Refinement method	Full-matrix least-squares on F ²	Full-matrix least-squares on F ²	Full-matrix least-squares on F ²
Weighting scheme	w = [s ² Fo ² + AP ² + BP] ⁻¹ , with P = (Fo ² + 2 Fc ²)/3, A = 0.089, B = 0.134	w = [s ² Fo ² + AP ² + BP] ⁻¹ , with P = (Fo ² + 2 Fc ²)/3, A = 0.00, B = 3.19	w = [s ² Fo ² + AP ² + BP] ⁻¹ , with P = (Fo ² + 2 Fc ²)/3, A = 0.0606, B = 4.8015
Data / restraints / parameters	1086 / 0 / 97	1983 / 111 / 137	4330 / 0 / 271
Goodness-of-fit on F2	1.071	1.198	1.076
Final R indices [I>2s(I)]	R1 = 0.0527, wR2 = 0.1353	R1 = 0.0408, wR2 = 0.0817	R1 = 0.0544, wR2 = 0.1352
R indices (all data)	R1 = 0.0815, wR2 = 0.1611	R1 = 0.0457, wR2 = 0.0840	R1 = 0.0667, wR2 = 0.1421
Largest diff. peak and hole	0.277 and -0.298 e.Å ⁻³	0.06(3) and -0.625 e.Å ⁻³	2.527 and -0.812 e.Å ⁻³

	3CNCM	4CNCM	4CICM
Empirical formula	C13 H7 N3	C13 H7 N3	C13 H7 F3 N2
Formula weight	205.22	205.22	248.21
Crystal color, shape, size	yellow needle, 0.466 ×	yellow plate, 0.49 × 0.13 ×	yellow plate, 0.23 × 0.05 ×
Temperature	0.04 × 0.02 mm ³	0.06 mm ³	0.03 mm ³
Wavelength	100.00 K	147.00 K	147.00 K
Crystal system, space group	1.54178 Å Orthorhombic, Pca2 ₁	0.71073 Å Orthorhombic, Pca2 ₁	1.54178 Å Orthorhombic, P2 ₁ 2 ₁ 2 ₁
Unit cell dimensions	a = 24.159(2) Å a = 90°. b = 5.0613(4) Å b = 90°. c = 17.6873(13) Å g = 90°.	a = 23.323(14) Å a = 90°. b = 3.875(3) Å b = 90°. c = 11.538(7) Å g = 90°.	a = 6.7547(5) Å a = 90°. b = 8.1110(6) Å b = 90°. c = 43.448(3) Å g = 90°.
Volume	2162.7(3) Å ³	1042.6(11) Å ³	2380.4(3) Å ³
Z	8	4	8
Density (calculated)	1.261 g/cm ³	1.307 g/cm ³	1.385 g/cm ³
Absorption coefficient	0.626 mm ⁻¹	0.082 mm ⁻¹	1.013 mm ⁻¹
F(000)	848	424	1008
Data collection			
Diffractometer	Bruker D8 Venture	Bruker D8 Venture	Bruker D8 Venture
Theta range for data collection	3.659 to 66.591°.	1.746 to 25.032°.	4.070 to 68.224°.
Index ranges	-28<=h<=28, -6<=k<=6, -21<=l<=21	-27<=h<=27, -4<=k<=4, -13<=l<=13	-8<=h<=8, -9<=k<=9, -52<=l<=52
Reflections collected	23833	17068	49346
Independent reflections	3686 [R _{int} = 0.0961]	1833 [R _{int} = 0.1473]	4342 [R _{int} = 0.0887]
Observed Reflections	3070	1477	3788
Completeness to theta	99.9 %	99.8 %	99.8 %
Solution and Refinement			
Absorption correction	Semi-empirical from equivalents	Semi-empirical from equivalents	Semi-empirical from equivalents
Max. and min. transmission	0.7533 and 0.5427	0.7454 and 0.3802	0.7533 and 0.6070
Solution	Intrinsic methods	Intrinsic methods	Intrinsic methods
Refinement method	Full-matrix least-squares on F ²	Full-matrix least-squares on F ²	Full-matrix least-squares on F ²
Weighting scheme	w = [s ² Fo ² + AP ² + BP] ⁻¹ , with P = (Fo ² + 2 Fc ²)/3, A = 0.145, B = 6.81	w = [s ² Fo ² + AP ² + BP] ⁻¹ , with P = (Fo ² + 2 Fc ²)/3, A = 0.00, B = 0.499	w = [s ² Fo ² + AP ² + BP] ⁻¹ , with P = (Fo ² + 2 Fc ²)/3, A = 0.054, B = 14.3
Data / restraints / parameters	3686 / 1 / 290	1833 / 1 / 145	4342 / 313 / 316
Goodness-of-fit on F ²	1.071	1.050	1.115
Final R indices [I>2s(I)]	R1 = 0.1057, wR2 = 0.2655	R1 = 0.0596, wR2 = 0.1451	R1 = 0.1191, wR2 = 0.2728
R indices (all data)	R1 = 0.1218, wR2 = 0.2814	R1 = 0.0770, wR2 = 0.1596	R1 = 0.1297, wR2 = 0.2794
Largest diff. peak and hole	0(2) 0.846 and -0.399 e.Å ⁻³	-0.4(10) 0.209 and -0.246 e.Å ⁻³	0.6(10) 0.511 and -0.586 e.Å ⁻³
Twin Details			
Type, twin law			Merohedral, -1 0 0 0 -1 0 0
Twin element, domain ratio			0 -1 Inversion twin, 60:40

S4.1: Crystallographic data for 34FCM:

Data collection

Single crystals suitable for X-ray diffraction were grown by slow evaporation of a solution of chloroform and methanol. A light yellow crystal (needle, approximate dimensions $0.53 \times 0.05 \times 0.03 \text{ mm}^3$) was placed onto the tip of a MiTeGen pin and mounted on a Bruker Venture D8 diffractometer equipped with a PhotonIII detector at 147.00 K. The data collection was carried out using Mo $K\alpha$ radiation ($\lambda = 1.54178 \text{ \AA}$, $I_{\mu\text{S}}$ micro-source) with a frame time of 2 seconds and a detector distance of 40 mm. A collection strategy was calculated and complete data to a resolution of 0.80 \AA with a redundancy of 8.3 were collected. The frames were integrated with the Bruker SAINT¹ software package using a narrow-frame algorithm to 0.82 \AA resolution. Data were corrected for absorption effects using the multi-scan method (SADABS).² Please refer to Table 1 for additional crystal and refinement information.

Structure solution and refinement

The space group $P 1 21/c 1$ was determined based on intensity statistics and systematic absences. The structure was solved using the SHELX suite of programs³ and refined using full-matrix least-squares on F^2 within the OLEX2 suite.⁴ An intrinsic phasing solution was calculated, which provided most non-hydrogen atoms from the E-map. Full-matrix least squares / difference Fourier cycles were performed, which located the remaining non-hydrogen atoms. All non-hydrogen atoms were refined with anisotropic displacement parameters. The hydrogen atoms were placed in ideal positions and refined as riding atoms with relative isotropic displacement parameters. The final full matrix least squares refinement converged to $R1 = 0.0347$ and $wR2 = 0.0878$ (F^2 , all data). The goodness-of-fit was 1.072. On the basis of the final model, the calculated density was 1.380 g/cm^3 and $F(000)$, 440 e⁻. Disordered was model for one of the fluorine atoms.

¹SAINT, V8.30A, Bruker Analytical X-Ray Systems, Madison, WI, 2012.

²SADABS, 2.03, Bruker Analytical X-Ray Systems, Madison, WI, 2016.

³G. M. Sheldrick, *Acta Cryst.* A64, 112 - 122 (2008). Sheldrick, G.M. (2015). *Acta Cryst.* A71, 3-8.

⁴O. V. Dolomanov, L. J. Bourhis, R. J. Gildea, J. A. K. Howard and H. Puschmann, *J. Appl. Crystallogr.*, 2009, 42, 339–341.

S4.2: Crystallographic data for 236FCM

Data collection

Single crystals suitable for X-ray diffraction were grown by slow evaporation of methanol and chloroform. A light yellow crystal (plate, approximate dimensions $0.37 \times 0.06 \times 0.02 \text{ mm}^3$) was placed onto the tip of a MiTeGen pin and mounted on a Bruker Venture D8 diffractometer equipped with a PhotonIII detector at 147.00 K. The data collection was carried out using Mo $K\alpha$ radiation ($\lambda = 0.71073 \text{ \AA}$, $I_{\mu\text{S}}$ micro-source) with a frame time of 12 seconds and a detector distance of 40 mm. A collection strategy was calculated and complete data to a resolution of 0.83 \AA with a redundancy of 5.5 were collected. The frames were integrated with the Bruker SAINT¹ software package using a narrow-frame algorithm to 0.83 \AA resolution. Data were corrected for absorption effects using the multi-scan method (SADABS).² Please refer to Table 1 for additional crystal and refinement information.

Structure solution and refinement

The space group $P 2_1/c$ was determined based on intensity statistics and systematic absences. The structure was solved using the SHELX suite of programs³ and refined using full-matrix least-squares on F^2 within the OLEX2 suite.⁴ An intrinsic phasing solution was calculated, which provided most non-hydrogen atoms from the E-map. Full-matrix least squares / difference Fourier cycles were performed, which located the remaining non-hydrogen atoms. All non-hydrogen atoms were refined with anisotropic displacement parameters. The hydrogen atoms were placed in ideal positions and refined as riding atoms with relative isotropic displacement parameters. The final full matrix least squares refinement converged to $R1 = 0.0493$ and $wR2 = 0.1499$ (F^2 , all data). The goodness-of-fit was 1.032. On the basis of the final model, the calculated density was 1.518 g/cm^3 and $F(000)$, 472 e⁻. One of the fluorine atoms is disordered over two positions with occupancies 0.753 and 0.247.

¹SAINT, V8.30A, Bruker Analytical X-Ray Systems, Madison, WI, 2012.

²SADABS, 2.03, Bruker Analytical X-Ray Systems, Madison, WI, 2016.

³G. M. Sheldrick, *Acta Cryst. A*64, 112 - 122 (2008). Sheldrick, G.M. (2015). *Acta Cryst. A*71, 3-8.

⁴O. V. Dolomanov, L. J. Bourhis, R. J. Gildea, J. A. K. Howard and H. Puschmann, *J. Appl. Crystallogr.*, 2009, 42, 339–341.

S4.3: Crystallographic data for 25FCM

Data collection

Single crystals suitable for X-ray diffraction were grown by slow evaporation of methanol and chloroform. A yellow crystal (needle, approximate dimensions $0.6 \times 0.08 \times 0.03 \text{ mm}^3$) was placed onto the tip of a MiTeGen pin and mounted on a Bruker Venture D8 diffractometer equipped with a PhotonIII detector at 147.00 K. The data collection was carried out using Mo $K\alpha$ radiation ($\lambda = 0.71073 \text{ \AA}$, I μ S micro-source) with a frame time of 10 seconds and a detector distance of 40 mm. A collection strategy was calculated and complete data to a resolution of 0.81 \AA with a redundancy of 5.5 were collected. The frames were integrated with the Bruker SAINT¹ software package using a narrow-frame algorithm to 0.81 \AA resolution. Data were corrected for absorption effects using the multi-scan method (SADABS).² Please refer to Table 1 for additional crystal and refinement information.

Structure solution and refinement

The space group $P 2_1/c$ was determined based on intensity statistics and systematic absences. The structure was solved using the SHELX suite of programs³ and refined using full-matrix least-squares on F^2 within the OLEX2 suite.⁴ An intrinsic phasing solution was calculated, which provided most non-hydrogen atoms from the E-map. Full-matrix least squares / difference Fourier cycles were performed, which located the remaining non-hydrogen atoms. All non-hydrogen atoms were refined with anisotropic displacement parameters. The hydrogen atoms were placed in ideal positions and refined as riding atoms with relative isotropic displacement parameters. The final full matrix least squares refinement converged to $R1 = 0.0690$ and $wR2 = 0.2116$ (F^2 , all data). The goodness-of-fit was 1.001. On the basis of the final model, the calculated density was 1.435 g/cm^3 and $F(000)$, 440 e⁻. The structure has pseudomerohedral twinning, with twin law $-1 \ 0 \ 0, 0 \ -1 \ 0, 0.02 \ 0 \ 1$. Platon Addsym⁵ doesn't suggest any missed symmetry despite the β angle is close to 90° .

¹SAINT, V8.30A, Bruker Analytical X-Ray Systems, Madison, WI, 2012.

²SADABS, 2.03, Bruker Analytical X-Ray Systems, Madison, WI, 2016.

³G. M. Sheldrick, Acta Cryst. A64, 112 - 122 (2008). Sheldrick, G.M. (2015). Acta Cryst. A71, 3-8.

⁴O. V. Dolomanov, L. J. Bourhis, R. J. Gildea, J. A. K. Howard and H. Puschmann, J. Appl. Crystallogr., 2009, 42, 339–341.

⁵A.L.Spek, Acta Cryst. 2009, D65, 148-155

S4.4: Crystallographic data for **4CF3CM**

Data collection

Single crystals suitable for X-ray diffraction were grown by slow evaporation of methanol and chloroform. A yellow crystal (plate, approximate dimensions $0.46 \times 0.22 \times 0.09 \text{ mm}^3$) was placed onto the tip of a MiTeGen pin and mounted on a Bruker Venture D8 diffractometer equipped with a PhotonIII detector at 220.00 K. This temperature was chosen because the crystal suffers from pseudomeroheredral twinning and modulation at low temperature, making the structure solution unsuccessful. The data collection was carried out using Mo $K\alpha$ radiation ($\lambda = 0.71073 \text{ \AA}$, I μ S micro-source) with a frame time of 10 seconds and a detector distance of 50 mm. A collection strategy was calculated and complete data to a resolution of 0.82 \AA with a redundancy of 4.8 were collected. The frames were integrated with the Bruker SAINT¹ software package using a narrow-frame algorithm to 0.82 \AA resolution. Data were corrected for absorption effects using the multi-scan method (SADABS).² Please refer to Table 1 for additional crystal and refinement information.

Structure solution and refinement

The space group Pnma was determined based on intensity statistics and systematic absences. The structure was solved using the SHELX suite of programs³ and refined using full-matrix least-squares on F^2 within the OLEX2 suite.⁴ An intrinsic phasing solution was calculated, which provided most non-hydrogen atoms from the E-map. Full-matrix least squares / difference Fourier cycles were performed, which located the remaining non-hydrogen atoms. All non-hydrogen atoms were refined with anisotropic displacement parameters. The hydrogen atoms were placed in ideal positions and refined as riding atoms with relative isotropic displacement parameters. The final full matrix least squares refinement converged to $R1 = 0.0535$ and $wR2 = 0.1763$ (F^2 , all data). The goodness-of-fit was 1.016. On the basis of the final model, the calculated density was 1.402 g/cm^3 and $F(000)$, 504 e⁻. Disorder was modelled for the CF₃ group.

¹SAINT, V8.30A, Bruker Analytical X-Ray Systems, Madison, WI, 2012.

²SADABS, 2.03, Bruker Analytical X-Ray Systems, Madison, WI, 2016.

³G. M. Sheldrick, *Acta Cryst.* A64, 112 - 122 (2008). Sheldrick, G.M. (2015). *Acta Cryst.* A71, 3-8.

⁴O. V. Dolomanov, L. J. Bourhis, R. J. Gildea, J. A. K. Howard and H. Puschmann, *J. Appl. Crystallogr.*, 2009, 42, 339–341.

S4.5 Crystallographic data for 3CI3CM (colorless plates)

Data collection

Single crystals suitable for X-ray diffraction were grown by slow evaporation of methanol. A colourless crystal (plate, approximate dimensions $0.27 \times 0.09 \times 0.03 \text{ mm}^3$) was placed onto the tip of a MiTeGen pin and mounted on a Bruker Venture D8 diffractometer equipped with a PhotonIII detector at 148.00 K. The data collection was carried out using Cu K α radiation ($\lambda = 1.54178 \text{ \AA}$, I μ S micro-source) with a frame time of 8 seconds and a detector distance of 40 mm. A collection strategy was calculated and complete data to a resolution of 0.82 \AA with a redundancy of 8.8 were collected. The frames were integrated with the Bruker SAINT¹ software package using a narrow-frame algorithm to 0.84 \AA resolution. Data were corrected for absorption effects using the multi-scan method (SADABS).² Please refer to Table 1 for additional crystal and refinement information.

Structure solution and refinement

The space group P $2_1/c$ was determined based on intensity statistics and systematic absences. The structure was solved using the SHELX suite of programs³ and refined using full-matrix least-squares on F^2 within the OLEX2 suite.⁴ An intrinsic phasing solution was calculated, which provided most non-hydrogen atoms from the E-map. Full-matrix least squares / difference Fourier cycles were performed, which located the remaining non-hydrogen atoms. All non-hydrogen atoms were refined with anisotropic displacement parameters. The hydrogen atoms were placed in ideal positions and refined as riding atoms with relative isotropic displacement parameters. The final full matrix least squares refinement converged to $R1 = 0.1216$ and $wR2 = 0.3430$ (F^2 , all data). The goodness-of-fit was 1.034. On the basis of the final model, the calculated density was 1.326 g/cm^3 and $F(000)$, 440 e $^-$.

¹SAINT, V8.30A, Bruker Analytical X-Ray Systems, Madison, WI, 2012.

²SADABS, 2.03, Bruker Analytical X-Ray Systems, Madison, WI, 2016.

³G. M. Sheldrick, Acta Cryst. A64, 112 - 122 (2008). Sheldrick, G.M. (2015). Acta Cryst. A71, 3-8.

⁴O. V. Dolomanov, L. J. Bourhis, R. J. Gildea, J. A. K. Howard and H. Puschmann, J. Appl. Crystallogr., 2009, 42, 339–341.

S4.6: Crystallographic data for 3CICM (yellow block)

Data collection

Single crystals suitable for X-ray diffraction were grown by slow evaporation of methanol. A yellow crystal (block, approximate dimensions $0.29 \times 0.27 \times 0.15 \text{ mm}^3$) was placed onto the tip of a MiTeGen pin and mounted on a Bruker Venture D8 diffractometer equipped with a PhotonIII detector at 147.00 K. The data collection was carried out using Mo K α radiation ($\lambda = 0.71073 \text{ \AA}$, I μ S micro-source) with a frame time of 2 seconds and a detector distance of 40 mm. A collection strategy was calculated and complete data to a resolution of 0.77 \AA with a redundancy of 5.3 were collected. The frames were integrated with the Bruker SAINT¹ software package using a narrow-frame algorithm to 0.77 \AA resolution. Data were corrected for absorption effects using the multi-scan method (SADABS).² Please refer to Table 1 for additional crystal and refinement information.

Structure solution and refinement

The space group P-1 was determined based on intensity statistics and systematic absences. The structure was solved using the SHELX suite of programs³ and refined using full-matrix least-squares on F² within the OLEX2 suite.⁴ An intrinsic phasing solution was calculated, which provided most non-hydrogen atoms from the E-map. Full-matrix least squares / difference Fourier cycles were performed, which located the remaining non-hydrogen atoms. All non-hydrogen atoms were refined with anisotropic displacement parameters. The hydrogen atoms were placed in ideal positions and refined as riding atoms with relative isotropic displacement parameters. The final full matrix least squares refinement converged to R1 = 0.0428 and wR2 = 0.1167 (F², all data). The goodness-of-fit was 1.037. On the basis of the final model, the calculated density was 1.360 g/cm^3 and F(000), 440 e⁻.

¹SAINT, V8.30A, Bruker Analytical X-Ray Systems, Madison, WI, 2012.

²SADABS, 2.03, Bruker Analytical X-Ray Systems, Madison, WI, 2016.

³G. M. Sheldrick, *Acta Cryst. A* 64, 112 - 122 (2008). Sheldrick, G.M. (2015). *Acta Cryst. A* 71, 3-8.

⁴O. V. Dolomanov, L. J. Bourhis, R. J. Gildea, J. A. K. Howard and H. Puschmann, *J. Appl. Crystallogr.*, 2009, 42, 339–341.

S4.7: Crystallographic data for 4C1CM

Data collection

Single crystals suitable for X-ray diffraction were grown by vapor diffusion of isopropyl alcohol into chloroform. A yellow crystal (plate, approximate dimensions $0.12 \times 0.1 \times 0.02 \text{ mm}^3$) was placed onto the tip of a MiTeGen pin and mounted on a Bruker Venture D8 diffractometer equipped with a PhotonIII detector at 100.00 K. The data collection was carried out using Cu $K\alpha$ radiation ($\lambda = 1.54178 \text{ \AA}$, I μ S micro-source) with a frame time of 10 seconds and a detector distance of 40 mm. A collection strategy was calculated and complete data to a resolution of 0.82 \AA were collected. The frames were integrated with the Bruker SAINT¹ software package using a narrow-frame algorithm to 0.84 \AA resolution. Data were corrected for absorption effects using the multi-scan method (SADABS).² Please refer to Table 1 for additional crystal and refinement information.

Structure solution and refinement

The space group Cc was determined based on intensity statistics and systematic absences. The structure was solved using the SHELX suite of programs³ and refined using full-matrix least-squares on F^2 within the OLEX2 suite.⁴ An intrinsic phasing solution was calculated, which provided most non-hydrogen atoms from the E-map. Full-matrix least squares / difference Fourier cycles were performed, which located the remaining non-hydrogen atoms. All non-hydrogen atoms were refined with anisotropic displacement parameters. The hydrogen atoms were placed in ideal positions and refined as riding atoms with relative isotropic displacement parameters. The structure has pseudomerohedral twinning, with twin law $-1\ 0\ 0, 0\ -1\ 0, 0\ 0\ 1$, corresponding to a 180 rotation around the crystallographic axis c . and it has also inversion twinning. The final full matrix least squares refinement converged to $R1 = 0.0868$ and $wR2 = 0.2211$ (F^2 , all data). The goodness-of-fit was 1.087. On the basis of the final model, the calculated density was 1.390 g/cm^3 and $F(000)$, 880 e⁻.

¹SAINT, V8.30A, Bruker Analytical X-Ray Systems, Madison, WI, 2012.

²SADABS, 2.03, Bruker Analytical X-Ray Systems, Madison, WI, 2016.

³G. M. Sheldrick, Acta Cryst. A64, 112 - 122 (2008). Sheldrick, G.M. (2015). Acta Cryst. A71, 3-8.

⁴O. V. Dolomanov, L. J. Bourhis, R. J. Gildea, J. A. K. Howard and H. Puschmann, J. Appl. Crystallogr., 2009, 42, 339–341.

S4.8: Crystallographic data for 3MethoxyCM

Data collection

A light yellow crystal (plate, approximate dimensions $0.11 \times 0.07 \times 0.03 \text{ mm}^3$) was placed onto the tip of a MiTeGen pin and mounted on a Bruker Venture D8 diffractometer equipped with a PhotonIII detector at 100.00 K. The data collection was carried out using Mo $K\alpha$ radiation ($\lambda = 0.71073 \text{ \AA}$, I μ S micro-source) with a frame time of 12 seconds and a detector distance of 40 mm. A collection strategy was calculated and complete data to a resolution of 0.82 \AA were collected. The frames were integrated with the Bruker SAINT¹ software package using a narrow-frame algorithm to 0.82 \AA resolution. Data were corrected for absorption effects using the multi-scan method (SADABS).² Please refer to Table 1 for additional crystal and refinement information.

Structure solution and refinement

The space group $P 2_1/m$ was determined based on intensity statistics and systematic absences. The structure was solved using the SHELX suite of programs³ and refined using full-matrix least-squares on F^2 within the OLEX2 suite.⁴ An intrinsic phasing solution was calculated, which provided most non-hydrogen atoms from the E-map. Full-matrix least squares / difference Fourier cycles were performed, which located the remaining non-hydrogen atoms. All non-hydrogen atoms were refined with anisotropic displacement parameters. The hydrogen atoms were placed in ideal positions and refined as riding atoms with relative isotropic displacement parameters. The final full matrix least squares refinement converged to $R1 = 0.0527$ and $wR2 = 0.1611$ (F^2 , all data). The goodness-of-fit was 1.071. On the basis of the final model, the calculated density was 1.289 g/cm^3 and $F(000)$, 220 e^- .

¹SAINT, V8.30A, Bruker Analytical X-Ray Systems, Madison, WI, 2012.

²SADABS, 2.03, Bruker Analytical X-Ray Systems, Madison, WI, 2016.

³G. M. Sheldrick, *Acta Cryst.* A64, 112 - 122 (2008). Sheldrick, G.M. (2015). *Acta Cryst.* A71, 3-8.

⁴O. V. Dolomanov, L. J. Bourhis, R. J. Gildea, J. A. K. Howard and H. Puschmann, *J. Appl. Crystallogr.*, 2009, 42, 339–341.

S4.9: Crystallographic data for 4BrCM

Data collection

Single crystals suitable for X-ray diffraction were grown by slow evaporation of toluene. A yellow crystal (plate, approximate dimensions $0.4 \times 0.11 \times 0.04 \text{ mm}^3$) was placed onto the tip of a MiTeGen pin and mounted on a Bruker Venture D8 diffractometer equipped with a PhotonIII detector at 148.00 K. The data collection was carried out using Mo $K\alpha$ radiation ($\lambda = 0.71073 \text{ \AA}$, I μ S micro-source) with a frame time of 10 seconds and a detector distance of 40 mm. A collection strategy was calculated and complete data to a resolution of 0.80 \AA with a redundancy of 4.8 were collected. The frames were integrated with the Bruker SAINT¹ software package using a narrow-frame algorithm to 0.82 \AA resolution. Data were corrected for absorption effects using the multi-scan method (SADABS).² Please refer to Table 1 for additional crystal and refinement information.

Structure solution and refinement

The space group $Pca2_1$ was determined based on intensity statistics and systematic absences. The structure was solved using the SHELX suite of programs³ and refined using full-matrix least-squares on F^2 within the OLEX2 suite.⁴ An intrinsic phasing solution was calculated, which provided most non-hydrogen atoms from the E-map. Full-matrix least squares / difference Fourier cycles were performed, which located the remaining non-hydrogen atoms. All non-hydrogen atoms were refined with anisotropic displacement parameters. The hydrogen atoms were placed in ideal positions and refined as riding atoms with relative isotropic displacement parameters. The final full matrix least squares refinement converged to $R1 = 0.0408$ and $wR2 = 0.0840$ (F^2 , all data). The goodness-of-fit was 1.198. On the basis of the final model, the calculated density was 1.629 g/cm^3 and $F(000)$, 512 e⁻.

¹SAINT, V8.30A, Bruker Analytical X-Ray Systems, Madison, WI, 2012.

²SADABS, 2.03, Bruker Analytical X-Ray Systems, Madison, WI, 2016.

³G. M. Sheldrick, *Acta Cryst. A*64, 112 - 122 (2008). Sheldrick, G.M. (2015). *Acta Cryst. A*71, 3-8.

⁴O. V. Dolomanov, L. J. Bourhis, R. J. Gildea, J. A. K. Howard and H. Puschmann, *J. Appl. Crystallogr.*, 2009, 42, 339–341.

S4.10: Crystallographic Data for 3BrCM

Data collection

A yellow crystal (block, approximate dimensions $0.26 \times 0.16 \times 0.12 \text{ mm}^3$) was placed onto the tip of a MiTeGen pin and mounted on a Bruker Venture D8 diffractometer equipped with a PhotonIII detector at 100.00 K. The data collection was carried out using Mo $K\alpha$ radiation ($\lambda = 0.71073 \text{ \AA}$, I μ S micro-source) with a frame time of 2 seconds and a detector distance of 40 mm. A collection strategy was calculated and complete data to a resolution of 0.77 \AA were collected. The frames were integrated with the Bruker SAINT¹ software package using a narrow-frame algorithm to 0.80 \AA resolution. Data were corrected for absorption effects using the multi-scan method (SADABS).² Please refer to Table 1 for additional crystal and refinement information.

Structure solution and refinement

The space group P-1 was determined based on intensity statistics and systematic absences. The structure was solved using the SHELX suite of programs³ and refined using full-matrix least-squares on F^2 within the OLEX2 suite.⁴ An intrinsic phasing solution was calculated, which provided most non-hydrogen atoms from the E-map. Full-matrix least squares / difference Fourier cycles were performed, which located the remaining non-hydrogen atoms. All non-hydrogen atoms were refined with anisotropic displacement parameters. The hydrogen atoms were placed in ideal positions and refined as riding atoms with relative isotropic displacement parameters. The final full matrix least squares refinement converged to $R1 = 0.0544$ and $wR2 = 0.1421$ (F^2 , all data). The goodness-of-fit was 1.076. On the basis of the final model, the calculated density was 1.618 g/cm^3 and $F(000)$, 512 e⁻.

¹SAINT, V8.30A, Bruker Analytical X-Ray Systems, Madison, WI, 2012.

²SADABS, 2.03, Bruker Analytical X-Ray Systems, Madison, WI, 2016.

³G. M. Sheldrick, *Acta Cryst. A*64, 112 - 122 (2008). Sheldrick, G.M. (2015). *Acta Cryst. A*71, 3-8.

⁴O. V. Dolomanov, L. J. Bourhis, R. J. Gildea, J. A. K. Howard and H. Puschmann, *J. Appl. Crystallogr.*, 2009, 42, 339–341.

S4.11: Crystallographic Data for 3CNCM

Data collection

Single crystals suitable for X-ray diffraction were grown by vapor diffusion of chloroform into isopropyl alcohol. A yellow crystal (needle, approximate dimensions $0.466 \times 0.04 \times 0.02 \text{ mm}^3$) was placed onto the tip of a MiTeGen pin and mounted on a Bruker Venture D8 diffractometer equipped with a PhotonIII detector at 100.00 K. The data collection was carried out using Cu $K\alpha$ radiation ($\lambda = 1.54178 \text{ \AA}$, I μ S micro-source) with a frame time of 6 seconds and a detector distance of 40 mm. A collection strategy was calculated and complete data to a resolution of 0.82 \AA were collected. The frames were integrated with the Bruker SAINT¹ software package using a narrow-frame algorithm to 0.84 \AA resolution. Data were corrected for absorption effects using the multi-scan method (SADABS).² Please refer to Table 1 for additional crystal and refinement information.

Structure solution and refinement

The space group $Pca2_1$ was determined based on intensity statistics and systematic absences. The structure was solved using the SHELX suite of programs³ and refined using full-matrix least-squares on F^2 within the OLEX2 suite.⁴ An intrinsic phasing solution was calculated, which provided most non-hydrogen atoms from the E-map. Full-matrix least squares / difference Fourier cycles were performed, which located the remaining non-hydrogen atoms. All non-hydrogen atoms were refined with anisotropic displacement parameters. The hydrogen atoms were placed in ideal positions and refined as riding atoms with relative isotropic displacement parameters. The final full matrix least squares refinement converged to $R1 = 0.1057$ and $wR2 = 0.2814$ (F^2 , all data). The goodness-of-fit was 1.071. On the basis of the final model, the calculated density was 1.261 g/cm^3 and $F(000)$, 848 e⁻.

¹SAINT, V8.30A, Bruker Analytical X-Ray Systems, Madison, WI, 2012.

²SADABS, 2.03, Bruker Analytical X-Ray Systems, Madison, WI, 2016.

³G. M. Sheldrick, *Acta Cryst. A* 64, 112 - 122 (2008). Sheldrick, G.M. (2015). *Acta Cryst. A* 71, 3-8.

⁴O. V. Dolomanov, L. J. Bourhis, R. J. Gildea, J. A. K. Howard and H. Puschmann, *J. Appl. Crystallogr.*, 2009, 42, 339–341.

S4.12: Crystallographic Data for 4CNCM

Data collection

Single crystals suitable for X-ray diffraction were grown by slow evaporation of methanol. A yellow crystal (plate, approximate dimensions $0.49 \times 0.13 \times 0.06 \text{ mm}^3$) was placed onto the tip of a MiTeGen pin and mounted on a Bruker Venture D8 diffractometer equipped with a PhotonIII detector at 147.00 K. The data collection was carried out using Mo $K\alpha$ radiation ($\lambda = 0.71073 \text{ \AA}$, I μ S micro-source) with a frame time of 8 seconds and a detector distance of 40 mm. A collection strategy was calculated and complete data to a resolution of 0.80 \AA with a redundancy of 4.7 were collected. The frames were integrated with the Bruker SAINT¹ software package using a narrow-frame algorithm to 0.84 \AA resolution. Data were corrected for absorption effects using the multi-scan method (SADABS).² Please refer to Table 1 for additional crystal and refinement information.

Structure solution and refinement

The space group $Pca2_1$ was determined based on intensity statistics and systematic absences. The structure was solved using the SHELX suite of programs³ and refined using full-matrix least-squares on F^2 within the OLEX2 suite.⁴ An intrinsic phasing solution was calculated, which provided most non-hydrogen atoms from the E-map. Full-matrix least squares / difference Fourier cycles were performed, which located the remaining non-hydrogen atoms. All non-hydrogen atoms were refined with anisotropic displacement parameters. The hydrogen atoms were placed in ideal positions and refined as riding atoms with relative isotropic displacement parameters. The final full matrix least squares refinement converged to $R1 = 0.0596$ and $wR2 = 0.1596$ (F^2 , all data). The goodness-of-fit was 1.050. On the basis of the final model, the calculated density was 1.307 g/cm^3 and $F(000)$, 424 e⁻.

¹SAINT, V8.30A, Bruker Analytical X-Ray Systems, Madison, WI, 2012.

²SADABS, 2.03, Bruker Analytical X-Ray Systems, Madison, WI, 2016.

³G. M. Sheldrick, *Acta Cryst. A* 64, 112 - 122 (2008). Sheldrick, G.M. (2015). *Acta Cryst. A* 71, 3-8.

⁴O. V. Dolomanov, L. J. Bourhis, R. J. Gildea, J. A. K. Howard and H. Puschmann, *J. Appl. Crystallogr.*, 2009, 42, 339–341.

S4.13: Crystallographic Data for 3FC3CM (nonreactive)

Data collection

Single crystals suitable for X-ray diffraction were grown from a xylene solution. A yellow crystal (plate, approximate dimensions $0.23 \times 0.05 \times 0.03 \text{ mm}^3$) was placed onto the tip of a MiTeGen pin and mounted on a Bruker Venture D8 diffractometer equipped with a PhotonIII detector at 147.00 K. The data collection was carried out using Cu $K\alpha$ radiation ($\lambda = 1.54178 \text{ \AA}$, I μ S micro-source) with a frame time of 4 seconds and a detector distance of 40 mm. A collection strategy was calculated and complete data to a resolution of 0.82 \AA with a redundancy of 7.7 were collected. The frames were integrated with the Bruker SAINT¹ software package using a narrow-frame algorithm to 0.83 \AA resolution. Data were corrected for absorption effects using the multi-scan method (SADABS).² Please refer to Table 1 for additional crystal and refinement information.

Structure solution and refinement

The space group $P2_12_12_1$ was determined based on intensity statistics and systematic absences. The structure was solved using the SHELX suite of programs³ and refined using full-matrix least-squares on F^2 within the OLEX2 suite.⁴ An intrinsic phasing solution was calculated, which provided most non-hydrogen atoms from the E-map. Full-matrix least squares / difference Fourier cycles were performed, which located the remaining non-hydrogen atoms. All non-hydrogen atoms were refined with anisotropic displacement parameters. The hydrogen atoms were placed in ideal positions and refined as riding atoms with relative isotropic displacement parameters. The final full matrix least squares refinement converged to $R1 = 0.1191$ and $wR2 = 0.2794$ (F^2 , all data). The goodness-of-fit was 1.115. On the basis of the final model, the calculated density was 1.385 g/cm^3 and $F(000)$, 1008 e⁻.

¹SAINT, V8.30A, Bruker Analytical X-Ray Systems, Madison, WI, 2012.

²SADABS, 2.03, Bruker Analytical X-Ray Systems, Madison, WI, 2016.

³G. M. Sheldrick, *Acta Cryst.* A64, 112 - 122 (2008). Sheldrick, G.M. (2015). *Acta Cryst.* A71, 3-8.

⁴O. V. Dolomanov, L. J. Bourhis, R. J. Gildea, J. A. K. Howard and H. Puschmann, *J. Appl. Crystallogr.*, 2009, 42, 339–341.

S4.14: Crystallographic Data for 3CF3CM (reactive)

Data collection

Single crystals suitable for X-ray diffraction were grown by slow evaporation of an ethanol/water solution. A yellow crystal (plate, approximate dimensions $0.4 \times 0.3 \times 0.04 \text{ mm}^3$) was placed onto the tip of a MiTeGen pin and mounted on a Bruker Venture D8 diffractometer equipped with a PhotonIII detector at 100.00 K. The data collection was carried out using Mo K α radiation ($\lambda = 0.71073 \text{ \AA}$, I μ S micro-source) with a frame time of 5 seconds and a detector distance of 40 mm. A collection strategy was calculated and complete data to a resolution of 0.77 \AA were collected. The frames were integrated with the Bruker SAINT¹ software package using a narrow-frame algorithm to 0.77 \AA resolution. Data were corrected for absorption effects using the multi-scan method (SADABS).² Please refer to Table 1 for additional crystal and refinement information.

Structure solution and refinement

The space group P $2_1/c$ was determined based on intensity statistics and systematic absences. The structure was solved using the SHELX suite of programs³ and refined using full-matrix least-squares on F^2 within the OLEX2 suite.⁴ An intrinsic phasing solution was calculated, which provided non-hydrogen atoms from the E-map. Full-matrix least squares / difference Fourier cycles were performed. All non-hydrogen atoms were refined with anisotropic displacement parameters. The hydrogen atoms were placed in ideal positions and refined as riding atoms with relative isotropic displacement parameters. The final full matrix least squares refinement converged to $R1 = 0.0568$ and $wR2 = 0.1507$ (F^2 , all data). The goodness-of-fit was 1.057. On the basis of the final model, the calculated density was 1.433 g/cm^3 and $F(000)$, 504 e $^-$.

¹SAINT, V8.30A, Bruker Analytical X-Ray Systems, Madison, WI, 2012.

²SADABS, 2.03, Bruker Analytical X-Ray Systems, Madison, WI, 2016.

³G. M. Sheldrick, Acta Cryst. A64, 112 - 122 (2008). Sheldrick, G.M. (2015). Acta Cryst. A71, 3-8.

⁴O. V. Dolomanov, L. J. Bourhis, R. J. Gildea, J. A. K. Howard and H. Puschmann, J. Appl. Crystallogr., 2009, 42, 339–341.